



Michigan Technological University
Create the Future Digital Commons @ Michigan Tech

Dissertations, Master's Theses and Master's
Reports - Open

Dissertations, Master's Theses and Master's
Reports

2013

THERMAL CHARACTERIZATION OF A GASOLINE TURBOCHARGED DIRECT INJECTION (GTDI) ENGINE UTILIZING LEAN OPERATION AND EXHAUST GAS RECIRCULATION (EGR)

Daniel P. Madison
Michigan Technological University

Follow this and additional works at: <https://digitalcommons.mtu.edu/etds>

 Part of the [Mechanical Engineering Commons](#)

Copyright 2013 Daniel P. Madison

Recommended Citation

Madison, Daniel P., "THERMAL CHARACTERIZATION OF A GASOLINE TURBOCHARGED DIRECT INJECTION (GTDI) ENGINE UTILIZING LEAN OPERATION AND EXHAUST GAS RECIRCULATION (EGR)", Dissertation, Michigan Technological University, 2013.
<https://doi.org/10.37099/mtu.dc.etds/852>

Follow this and additional works at: <https://digitalcommons.mtu.edu/etds>

 Part of the [Mechanical Engineering Commons](#)

THERMAL CHARACTERIZATION OF A GASOLINE TURBOCHARGED DIRECT
INJECTION (GTDI) ENGINE UTILIZING LEAN OPERATION AND EXHAUST GAS
RECIRCULATION (EGR)

By

Daniel P. Madison

A DISSERTATION

Submitted in partial fulfillment of the requirements for the degree of

DOCTOR OF PHILOSOPHY

in Mechanical Engineering-Engineering Mechanics

MICHIGAN TECHNOLOGICAL UNIVERSITY

2013

© 2013 Daniel P. Madison

This dissertation has been approved in partial fulfillment of the requirements for the Degree of DOCTOR OF PHILOSOPHY in Mechanical Engineering-Engineering Mechanics.

Department of Mechanical Engineering-Engineering Mechanics

Dissertation Advisor: *Dr. Scott A. Miers*

Committee Member: *Dr. Jeff D. Naber*

Committee Member: *Dr. Jason R. Blough*

Committee Member: *Dr. Paul G. Sanders*

Department Chair: *Dr. William Predebon*

Contents

List of Figures	xi
List of Tables	xvii
Acknowledgments	xix
Preface	xxi
Nomenclature	xxiii
Abstract	xxvii
1 Introduction	1
1.1 Motivation	1
1.2 Areas of Focus	2
1.2.1 Global and In-Cylinder Temperature and Heat Transfer Characterization	3
1.2.2 Fuel Spray Impingement on the Piston	5
2 Literature Review	7

2.1	Combustion Chamber Temperature and Heat Flux Measurement Techniques	7
2.1.1	Metallurgical Temperature Sensors	7
2.1.2	Coaxial and Triaxial Surface Thermocouples	8
2.1.3	Pair-Wire Thermocouples	10
2.1.4	Thin Film Temperature and Heat Flux Sensors	12
2.1.5	Mechanical Linkage Telemetry Systems	13
2.1.6	Wireless Telemetry Systems	14
2.1.6.1	Electromagnetic Induction	14
2.1.6.2	Bluetooth Network	16
2.1.6.3	Microwave Wireless Telemetry	17
2.2	Applications of Temperature and Heat Flux Measurements in IC Engines .	17
2.2.1	In-Cylinder Heat Transfer Modeling Studies	17
2.2.2	Parametric Effects on In-Cylinder Temperatures and Heat Transfer	19
2.2.3	Identification of Fuel Impingement on the Piston	22
2.3	Engine Energy Distribution	23
3	Method/Test Plan	27
3.1	Experimental Setup	27
3.1.1	Test Cell Setup	27
3.1.1.1	Engine and Dynamometer	27
3.1.1.2	Cooling System	28
3.1.1.3	Air Intake/Exhaust System	29

3.1.1.4	Fuel System	31
3.1.1.5	Engine Control	32
3.1.2	Engine Instrumentation	33
3.1.2.1	Combustion Chamber Temperature and Heat Flux Instrumentation	34
3.1.3	Data Acquisition	36
3.1.3.1	Wireless Telemetry System	38
3.2	Initial Testing without Telemetry	40
3.2.1	Baseline Performance	41
3.2.2	Lean and Dilute Combustion Testing on 2nd Engine	45
3.3	Initial Testing with Telemetry	46
3.4	Test Plan and Procedure	48
3.4.1	Global and In-Cylinder Temperature and Heat Transfer Characterization	48
3.4.2	Identification of Fuel Spray Impingement on the Piston	50
4	Data Processing and Analysis	51
4.1	Piston Thermocouple Telemetry Signal Processing	51
4.2	Heat Flux Calculation	53
4.3	Thermodynamic Analysis of the Engine System	54
4.3.1	1st Law Energy Analysis	54
4.3.2	2nd Law Exergy Analysis	57

4.4	Impingement Identification	58
5	Results and Discussion	61
5.1	Energy Balance Results	61
5.2	Exergy Analysis Results	68
5.3	Energy and Exergy Results Summary	73
5.4	Empirical Model of Engine Energy Balance	74
5.5	Combustion Chamber Temperature and Heat Flux Results	78
5.6	Fuel Impingement Identification	84
6	Conclusions and Recommendations	93
6.1	Conclusions	93
6.2	Recommendations for Future Work	94
	References	97
A	Additional Energy and Exergy Balance Analysis Plots	103
A.1	Interaction Plots for CV 2	103
A.2	Exhaust Energy and Exergy Plots	105
B	Control Point Repeatability	111
C	Additional Combustion Chamber Temperature and Heat Flux Plots	113
D	Additional Impingement Identification Plots	127

E Letters of Permission	147
--	------------

List of Figures

2.1	M3 Templug Drawing	8
2.2	Diagram of a Coaxial Thermocouple	9
2.3	Section View of a Triaxial Thermocouple	10
2.4	Section View of a Pair-Wire Thermocouple	11
2.5	Diagram of an Eroding Ribbon Thermocouple	12
2.6	Diagram of a Thin Film RTD	12
2.7	Diagram of a Vatel Heat Flux Microsensor (HFM)	13
2.8	Image of Typical Linkage	14
2.9	Diagram of an Electromagnetic Induction System	15
2.10	Diagram of a Bluetooth Piston Telemetry System	16
2.11	Plot of the Evolution of Measured Surface Temperature Profiles	
	with Deposit Formation	21
2.12	Plots of Piston Surface Temperatures and Heat Flux	23
2.13	Energy Distribution for a 1.4L SI Engine	24
3.1	Cooling System Schematic	29
3.2	External Low-Pressure Cooled EGR System Schematic	30

3.3	Air Intake System Schematic	31
3.4	Schematic of Piston Thermocouples	35
3.5	Photographs Showing Piston Thermocouple Installation	35
3.6	Image of Cylinder Head Showing Instrumentation Locations for Thermocouples and Heat Flux Sensor	36
3.7	Wireless Telemetry Component Schematic	38
3.8	Microwave Wireless Telemetry Signal Conversion Process	39
3.9	Installation of Wireless Telemetry Components on the Piston	40
3.10	Plot of Cylinder Pressure vs Engine Position	43
3.11	Zoomed In Plot Showing the Exhaust Valve Opening	43
3.12	Photograph of Bank 1 Exhaust Cam Timing Gear	44
3.13	Zoomed In Plot Showing the Exhaust Valve Opening After Camshaft Fix	44
3.14	1500 RPM and 2.6 Bar BMEP EGR Sweep	45
3.15	1500 RPM and 2.6 Bar BMEP Lambda Sweep	46
3.16	Comparison of Normalized Piston STC Response	47
3.17	Normalized STC Response Before and After Cleaning	48
4.1	Example of Filtering Used on Telemetry Signal	52
4.2	Piston Surface Thermocouple Data: Raw and Processed	53
4.3	Control Volume for Engine Energy Balance 1	55
4.4	Control Volume for Engine Energy Balance 2	56

4.5	Plot of Piston Surface Temperatures for an HCCI Engine	59
4.6	Plot of Piston Surface Heat Flux for an HCCI Engine	59
5.1	Engine Energy Balance for CV1 and CV2	62
5.2	Main Effects of Dilute Combustion from Lean Operation and EGR on the Energy Distribution for Control Volume 2	63
5.3	Simulation Results of the Effect of Burn Duration on Gross Efficiency	65
5.4	Simulation Results for the Effect of Dilution on Gross Efficiency . . .	67
5.5	Simulation Results for the Effect of Gamma on Gross Efficiency . . .	67
5.6	Comparison of Exhaust Energy and Exergy for CV 1 at 2250 RPM . .	70
5.7	Comparison of Exhaust Energy and Exergy for CV 2 at 2250 RPM . .	71
5.8	Comparison of Exhaust Gas Temperatures on an Absolute and Relative Basis	72
5.9	Comparison of the Exergy Distributions for a Downsized and Downspeeded Engine	74
5.10	Energy Balance Model Fits for CV2	75
5.11	Piston Temperature Plot for 1500 RPM and 2 bar BMEP	80
5.12	Piston Temperature Plot for 1500 RPM and 8 bar BMEP	81
5.13	Comparison of Normalized Surface Temperature Profiles	82
5.14	Comparison of Cylinder Head Surface Heat Flux Profiles	83
5.15	SOI Sweep STC Results at 1500 RPM and 5 bar BMEP	85
5.16	SOI Sweep $dT/d\theta$ Results at 1500 RPM and 5 bar BMEP	87

5.17	SOI Sweep Heat Flux Results at 1500 RPM and 5 bar BMEP	88
5.18	SOI Sweep Normalized Heat Flux Results at 1500 RPM and 5 bar BMEP	89
5.19	Comparison of Impingement ID Techniques	91
A.1	Interaction Plot for Brake Efficiency Under Lean Conditions	103
A.2	Interaction Plot for Coolant Heat Energy Under Lean Conditions . . .	104
A.3	Interaction Plot for Exhaust Heat Energy Under Lean Conditions . . .	104
A.4	Interaction Plot for Brake Efficiency with EGR	104
A.5	Interaction Plot for Coolant Heat Energy with EGR	105
A.6	Interaction Plot for Exhaust Heat Energy with EGR	105
A.7	Comparison of Exhaust Energy and Exergy for CV 1 at 1500 RPM . . .	106
A.8	Comparison of Exhaust Energy and Exergy for CV 2 at 1500 RPM . . .	107
A.9	Comparison of Exhaust Energy and Exergy for CV 1 at 3000 RPM . . .	108
A.10	Comparison of Exhaust Energy and Exergy for CV 2 at 3000 RPM . . .	109
B.1	Repeatability of the Brake Efficiency and Exhaust Energy Percentage for the 1500/2.6 Control Point	111
B.2	Repeatability of the Coolant Flow Rate for the 1500/2.6 Control Point	112
C.1	Piston Temperature Plot for 1500 RPM and 2 bar BMEP	114
C.2	Piston Temperature Plot for 1500 RPM and 5 bar BMEP	115
C.3	Piston Temperature Plot for 1500 RPM and 8 bar BMEP	116

C.4	Piston Temperature Plot for 1500 RPM and 11 bar BMEP	117
C.5	Piston Temperature Plot for 2250 RPM and 2 bar BMEP	118
C.6	Piston Temperature Plot for 2250 RPM and 5 bar BMEP	119
C.7	Piston Temperature Plot for 2250 RPM and 8 bar BMEP	120
C.8	Piston Temperature Plot for 2250 RPM and 11 bar BMEP	121
C.9	Piston Temperature Plot for 3000 RPM and 2 bar BMEP	122
C.10	Piston Temperature Plot for 3000 RPM and 5 bar BMEP	123
C.11	Piston Temperature Plot for 3000 RPM and 8 bar BMEP	124
C.12	Piston Temperature Plot for 3000 RPM and 11 bar BMEP	125
D.1	SOI Sweep STC Results at 1500 RPM and 2.6 bar BMEP	128
D.2	SOI Sweep dT/d θ Results at 1500 RPM and 2.6 bar BMEP	129
D.3	SOI Sweep Normalized Heat Flux Results at 1500 RPM and 2.6 bar BMEP	130
D.4	SOI Sweep STC Results at 1500 RPM and 5 bar BMEP	131
D.5	SOI Sweep dT/d θ Results at 1500 RPM and 5 bar BMEP	132
D.6	SOI Sweep Normalized Heat Flux Results at 1500 RPM and 5 bar BMEP	133
D.7	SOI Sweep STC Results at 1500 RPM and 8 bar BMEP	134
D.8	SOI Sweep dT/d θ Results at 1500 RPM and 8 bar BMEP	135
D.9	SOI Sweep Normalized Heat Flux Results at 1500 RPM and 8 bar BMEP	136

D.10 SOI Sweep STC Results at 3000 RPM and 2.6 bar BMEP	137
D.11 SOI Sweep $dT/d\theta$ Results at 3000 RPM and 2.6 bar BMEP	138
D.12 SOI Sweep Normalized Heat Flux Results at 3000 RPM and 2.6 bar BMEP	139
D.13 SOI Sweep STC Results at 3000 RPM and 5 bar BMEP	140
D.14 SOI Sweep $dT/d\theta$ Results at 3000 RPM and 5 bar BMEP	141
D.15 SOI Sweep Normalized Heat Flux Results at 3000 RPM and 5 bar BMEP	142
D.16 SOI Sweep STC Results at 3000 RPM and 8 bar BMEP	143
D.17 SOI Sweep $dT/d\theta$ Results at 3000 RPM and 8 bar BMEP	144
D.18 SOI Sweep Normalized Heat Flux Results at 3000 RPM and 8 bar BMEP	145

List of Tables

3.1	Engine Specifications	28
3.2	Test Fuel Specifications	32
3.3	Low-Speed Measurements	33
3.4	High-Speed Instrumentation	34
3.5	DSP Technologies ACAP System Components	37
3.6	Ectron Model 563HL Amplifier Specifications	38
3.7	Engine Break-In Procedure	41
3.8	Baseline Mini-Map Test Conditions and BSFC Results	42
3.9	Engine Map Test Matrix	49
3.10	Impingement Test Matrix	50
5.1	Analysis of Engine Performance Parameters with Dilution	64
5.2	Comparison of the Effects of Lean Operation and EGR on Laminar Flame Speed	66
5.3	Coefficients for Brake Thermal Efficiency Fit	76
5.4	Coefficients for the Coolant Energy Fraction Fit	77
5.5	Coefficients for the Exhaust Energy Fraction Fit	77

5.6	Coefficients for the Exhaust Gas Temperature Fit	78
5.7	Effects of Dilution on Combustion Chamber Temperatures and	
	Heat Flux	84

Acknowledgments

I would like to thank my advisor, Dr. Scott Miers, for providing me with an incredible research opportunity. I gained an immense amount of knowledge from this project and couldn't have done so without your guidance and support along the way. I would also like thank my committee members Dr. Jeff Naber, Dr. Jason Blough, and Dr. Paul Sanders. Your feedback and suggestions helped to make this research a success.

I am very grateful for the financial and technical support of this research by Ford Motor Company and the Department of Energy. I also want to thank Larry Jones and the team at Medtherm who manufactured and installed the custom thermocouples that helped make this study possible. Additionally, I would like to extend a special thanks to Glen, Dan, Ron and the rest of the employees at IR Telemetrics who supplied the wireless telemetry hardware and helped me throughout my graduate career.

I am also extremely grateful to have met so many great people during my time at Michigan Tech. I thank my colleagues, labmates, and officemates for their friendship and support. You helped make everyday a fun and exciting experience.

I must thank my family for their encouragement and belief in me over this long journey and of course my wonderful wife, who stood by me and helped keep me focused.

Finally, I must thank God for all the blessings that he has given me. Without Him, none of this would have been possible.

Preface

None of the work in this dissertation has been previously published; however, it is likely that in the near future, large excerpts from the abstract and all chapters will be used for journal articles and conference papers. These future works would be co-authored by my advisor, Dr. Scott Miers. I collected and analyzed the data and have written all the chapters. Dr. Miers has provided feedback and guidance on data collection and analysis, as well as on the formatting and phrasing of the written content.

Nomenclature

AD	analog-to-digital
AFR	air-fuel ratio
AKI	anti-knock index
ATDC	after top dead center
ATI	Accurate Technologies Inc.
BDC	bottom dead center
BMEP	brake mean effective pressure
BSFC	brake specific fuel consumption
BTE	brake thermal efficiency
CAC	charge air cooler
CAD	crank angle degrees
CAFE	corporate average fuel economy
CI	compression ignition
COV	coefficient of variation
CR	compression ratio
CV	control volume
DAQ	data acquisition
DI	direct injection
DOE	design of experiments
ECU	engine control unit
EES [®]	engineering equation solver
EGR	exhaust gas recirculation
EGT	exhaust gas temperature
ETC	embedded thermocouple
GTDI	gasoline turbocharged direct injection
HCCI	homogeneous charge compression ignition
HFM	heat flux microsensor
IC	internal combustion
IMEP	indicated mean effective pressure
IRT	IR Telemetry Inc.
LBDI	lean burn direct injection

LFE	laminar flow element
LHV	lower heating value
LPM	liters per minute
LTC	low temperature combustion
MBT	maximum brake torque
MPS	mean piston speed
NI	National Instruments
PC	personal computer
PWM	pulse width modulation
RPM	revolutions per minute
RTD	resistance temperature detector
SI	spark ignition
SOI	start of injection
STC	surface thermocouple
TDC	top dead center
TEG	thermoelectric generator
TEI	Testing Engineers Inc.
UEGO	universal exhaust gas oxygen
ULBDI	ultra lean burn direct injection
USB	universal serial bus
UTC	underside thermocouple
VCO	voltage controlled oscillator
VOIS	variable output ignition system
VVT	variable valve timing
WHR	waste heat recovery
WOT	wide open throttle
A_n	Fourier series cosine coefficients
B_n	Fourier series sine coefficients
Q	heat
Q_{LHV}	fuel lower heating value
T	temperature
T_0	dead state temperature

T_w	surface temperature
W	work
X_Q	exergy of a heat source
c	specific heat capacity
h	specific enthalpy
k	thermal conductivity
m	mass
p	pressure
q_w''	surface heat flux
t	time
x	distance from the surface
α	thermal diffusivity
γ	ratio of specific heats
λ	relative air-fuel ratio
ω	angular frequency
ρ	density
θ	engine position

Abstract¹

The push for improved fuel economy and reduced emissions has led to great achievements in engine performance and control. These achievements have increased the efficiency and power density of gasoline engines dramatically in the last two decades. With the added power density, thermal management of the engine has become increasingly important. Therefore it is critical to have accurate temperature and heat transfer models as well as data to validate them. With the recent adoption of the 2025 Corporate Average Fuel Economy (CAFE) standard, there has been a push to improve the thermal efficiency of internal combustion engines even further. Lean and dilute combustion regimes along with waste heat recovery systems are being explored as options for improving efficiency. In order to understand how these technologies will impact engine performance and each other, this research sought to analyze the engine from both a 1st law energy balance perspective, as well as from a 2nd law exergy analysis. This research also provided insights into the effects of various parameters on in-cylinder temperatures and heat transfer as well as provides data for validation of other models.

It was found that the engine load was the dominant factor for the energy distribution, with higher loads resulting in lower coolant heat transfer and higher brake work and exhaust energy. From an exergy perspective, the exhaust system provided the best waste heat recovery potential due to its significantly higher temperatures compared to the cooling circuit. EGR and lean combustion both resulted in lower combustion chamber and exhaust temperatures; however, in most cases the increased flow rates resulted in a net increase in the energy in the exhaust. The exhaust exergy, on the other hand, was either increased or decreased depending on the location in the exhaust system and the other operating conditions. The effects of dilution from lean operation and EGR were compared using a dilution ratio, and the results showed that lean operation resulted in a larger increase in efficiency than the same amount of dilution with EGR. Finally, a method for identifying fuel spray impingement from piston surface temperature measurements was found.

¹The material contained in this section is planned for submission as part of a journal article and/or conference paper in the future.

Chapter 1

Introduction¹

1.1 Motivation

The push for improved fuel economy and reduced emissions has led to great achievements in engine performance and control. These achievements have increased the power density of gasoline engines dramatically in the last two decades. Engine technologies such as variable valve timing (VVT), direct injection (DI), and turbocharging have significantly improved engine power-to-weight and power-to-displacement ratios. A popular trend for increasing vehicle fuel economy in recent years has been to downsize the engine and add VVT, DI, and turbocharging technologies so that a lighter more efficient engine can replace a larger heavier one [1–3]. With the added power density, thermal management of the engine becomes increasingly important [2]. Engine block, cylinder head, valve, and piston materials are being pushed to their temperature limits [4, 5]. Therefore it has become increasingly important to have accurate temperature and heat transfer models as well as data to validate them. This research provides insights into the effects of various parameters on in-cylinder temperatures and heat transfer as well as provides data for validation of other models.

Additionally, regulations in the United States are attempting to push fuel economy to much higher levels in the near future. The most recent Corporate Average Fuel Economy (CAFE) standard would increase passenger car fuel economy to an estimated 54.5 miles per gallon

¹The material contained in this chapter is planned for submission as part of a journal article and/or conference paper in the future.

(mpg) by 2025. This represents an increase of over 50% from the 2016 CAFE standard of 35.5 mpg [6]. Meeting the 2025 CAFE standard will require new technologies to both improve the thermal efficiency of IC engines as well as recover some of the waste heat energy they generate. One path for improving the thermal efficiency of IC engines is to use low temperature combustion (LTC) techniques that utilize dilution from lean air-fuel ratios (AFR) or exhaust gas recirculation (EGR). In the near term, these technologies can be applied to existing spark ignition (SI) engines and in the future, advanced LTC regimes such as Homogeneous Charge Compression Ignition (HCCI) [7] or ultra-lean burn jet-ignition [8] could be implemented as well. These technologies inherently change the energy distribution of the engine. Alternatively, waste heat recovery (WHR) mechanisms such as thermoelectric generators (TEG) [9, 10] or Rankine cycle devices [11–15] could be added to existing engines. In order to understand how these two different paths would interact, it is necessary to evaluate the effects of dilution on the energy distribution of the engine and the resulting impact on waste heat recovery potential. This research provides insight into these effects by evaluating the energy and exergy distributions of the engine under a large range of conditions.

1.2 Areas of Focus

The overall project can be broken up into two distinct areas of focus. The main portion of the work is the characterization of global and in-cylinder temperatures and heat transfer. This work covers a large scope of engine operating conditions. The other smaller area of focus hones in on the effect of a specific phenomenon on in-cylinder temperatures and heat transfer. During early start of injection (SOI), it is possible for the liquid fuel spray to impinge on the surface of the piston. This dramatically affects piston surface temperatures and heat transfer. Creating a method for impingement identification from surface thermocouple measurements was the second area of focus for this research. This research was conducted on a downsized and boosted 3.5 liter V6 gasoline turbocharged direct injection (GTDI) engine that was specifically instrumented for this work.

1.2.1 Global and In-Cylinder Temperature and Heat Transfer Characterization

Problem Statement

Downsized and boosted gasoline engines offer significant improvements in efficiency and fuel economy; however, with their high specific power outputs, thermal management of engine components and subsystems becomes increasingly important [1–3]. During the design phase, models are used to estimate the thermal loading of engine components [16, 17]. However, predicting the temperatures and heat transfer inside an engine is difficult and requires complex models which are hard to validate since there is a lack of actual engine data [18, 19].

This area of the research project characterized the thermal loading of combustion chamber components as a function of engine speed, load, relative air-fuel ratio (AFR) and exhaust gas recirculation (EGR) rate. Under these varied conditions, the energy distribution between the brake work, coolant, and exhaust was quantified and the impact on the waste heat recovery potential was also analyzed. The results of these analyses will be useful for improving numerical models that can aid in the future development of GTDI engines.

From previous research and study in this area, certain outcomes were expected. For instance, it was clear that increasing the load increased the gas temperature inside the combustion chamber. This increased the temperatures and heat fluxes of combustion chamber components. In addition, heat transfer to the coolant and the energy leaving through the exhaust were both increased. However, as a fraction of the fuel energy, it has been shown that the exhaust energy increases with load, while the coolant energy decreases [20]. It was also known that increasing the engine speed reduces the time per cycle for heat transfer to occur and thus it was expected that with all other conditions remaining the same, the temperatures and heat fluxes to combustion chamber surfaces would decrease with increasing speed. It follows then that less energy would be transferred to the coolant through heat transfer and more would exit the engine via higher temperature exhaust gases. However, the impacts of some of the other variables were less clear. It has been shown that with the addition of dilution, via either EGR or a lean AFR, the cylinder temperatures are reduced and thermal efficiency is increased [7, 21, 22]. The lower combustion temperatures result in decreased heat transfer to the coolant; however, it

was unclear if more or less energy was exiting via the exhaust. Certainly the exhaust gas temperature was decreased; however, the mass flow rate was increased and thus depending on which of the two factors was dominant, the exhaust energy could have either increased or decreased. It was hypothesized that the decreased energy to the coolant would be transferred not only to increase the brake work but also, to a lesser degree, to increase the energy in the exhaust stream (increase of less than 25% of the coolant energy). It was also hypothesized that since air has a 7% lower specific heat than typical exhaust gases, that dilution from EGR would result in an up to 7% higher increase in efficiency than the same amount of dilution from lean operation.

Understanding the engine energy distribution and how it changes with operating conditions would be helpful for determining the cooling system capacities and turbocharger designs required for engines utilizing these operating modes. It also would show which areas had the most potential for waste heat recovery devices and how that potential would change with lean and dilute combustion.

Previous studies have shown that deposits on combustion chamber surfaces can have a significant effect on the response of surface thermocouples [23, 24]. As the deposit layer increased in thickness, it added thermal mass and decreased the response time of the sensor. In order to understand the effect of the deposits, it was necessary to run a consistent test point at the beginning and end of each run of testing to allow the temperature profiles to be compared over time, and if necessary a cleaning procedure was applied to attempt to restore the fast response time.

Goals

- Utilize surface and embedded thermocouples, along with high-speed signal conditioning and wireless telemetry, to characterize the temperature distribution and heat flux in combustion chamber components for varying speed, load, relative AFR, and EGR conditions.
- Characterize the energy distribution and waste heat recovery potential of the engine as a function of engine speed, load, relative AFR, and EGR.

Objectives

- Develop and implement an instrumentation package and data acquisition system capable of measuring combustion chamber temperatures and pressure as well as flow rates, temperatures, and pressures of flows into and out of the engine.
- Measure and quantify the effects of speed, load, relative AFR, and EGR rate on the distribution of energy between the brake work, exhaust flow and cooling system.
- Quantify the waste heat recovery potential of the exhaust and coolant streams utilizing a 2nd law of thermodynamics approach.
- Quantify changes in temperature and heat flux profiles due to deposits on component surfaces.

1.2.2 Fuel Spray Impingement on the Piston

Problem Statement

Fuel spray impingement on the piston has become a much more important factor for gasoline engines in recent years. Two high efficiency combustion regimes: stratified charge spark ignition (SI) and homogeneous charge compression ignition (HCCI), often result in fuel spray impingement on the piston. In the case of stratified charge spark ignition, the impingement occurs as a result of late start of injection (SOI) timing [25]. Conversely, in HCCI operation, impingement occurs due to early SOI timing [23, 26]. In this research, the effects of fuel spray impingement on the piston from early injection were investigated, but the combustion regime remained homogeneous charge spark ignition. SOI timing was varied to change impingement characteristics. The focus of this work was on identifying the conditions when impingement occurred.

Previous research on an HCCI engine has shown that it should be possible to detect fuel spray impingement on the piston using surface and embedded thermocouples. The fuel impinging on the piston surface caused rapid cooling of the surface and a large spike in heat transfer from the piston surface to the liquid fuel film [23]. It was expected that this same phenomenon would occur during early injection on the engine used in this research. Processing the data to search for this signature should identify the SOI timings that result in impingement as well as the locations on the piston where it occurs.

Goal

- Utilize piston surface and embedded thermocouples along with wireless telemetry to identify the SOI timings that result in fuel spray impingement on the piston.

Objectives

- Develop a signal processing technique to identify fuel spray impingement from piston surface temperature and heat flux measurements.
- Quantify the differences in piston heat transfer between impinging and non-impinging SOI timings.

Chapter 2

Literature Review¹

2.1 Combustion Chamber Temperature and Heat Flux Measurement Techniques

Heat transfer inside internal combustion engines has been of interest since their invention; however, experimental methods to detect and record temperatures with high temporal resolution were not always available. Data were taken as early as the late 1930s [27]; however, it did not become common until the mid 1960s. Since then numerous studies into internal combustion engine heat transfer have been conducted and the work up to 1987 is well summarized by Borman and Nishiwaki [19]. In nearly all cases, the goal of collecting temperature data was to create and validate models for engine heat transfer. These models require surface and in-depth temperature data from the piston, cylinder head, and cylinder liner for validation. Measuring surface temperatures of combustion chamber components requires the design of special thermocouples as well as telemetry systems to get the signals to a data acquisition system.

2.1.1 Metallurgical Temperature Sensors

Metallurgical temperature sensors have been in use since the 1970s and are one of the simplest forms of temperature measurement. The sensors correlate a change in the structure of the material and the corresponding change in material properties to the

¹The material contained in this chapter is planned for submission as part of a journal article and/or conference paper in the future.

maximum temperature it was exposed to. They are used when more accurate methods, such as thermocouples or resistance temperature detectors (RTD), would be too costly or inconvenient. Templugs are a commercially available metallurgical temperature sensor supplied by Testing Engineers Inc. (TEI) [28]. They are small set screws machined from hardened alloy steels. A diagram of the larger of the two sizes they offer is shown in Fig. 2.1. Templugs utilize the process of thermal tempering and correlate the change in the material's hardness to the maximum sustained temperature at its location.

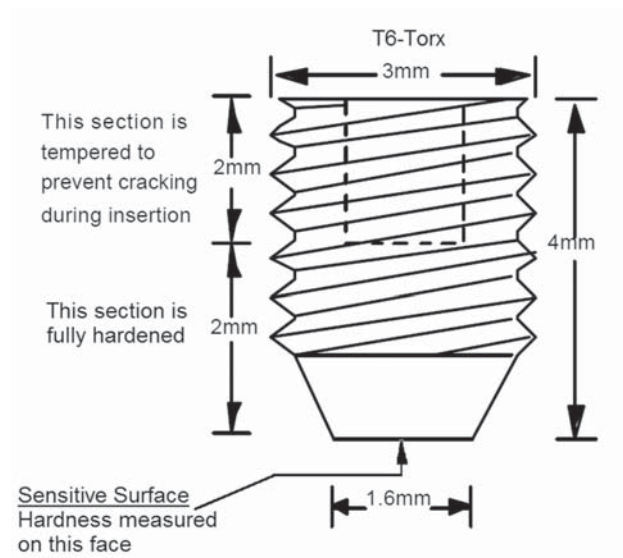


Figure 2.1: M3 Templug Drawing [28]

Madison et al. [29] investigated the performance of Templugs compared to thermocouples at multiple locations in the piston of a diesel engine. The results from Templugs matched the thermocouple data well in most cases; however, Templugs were found to potentially be susceptible to errors in locations with large axial thermal gradients through the Templug. In summary, metallurgical temperatures sensors are inexpensive and effective at indicating peak temperatures; however, they are unable to capture any dynamic phenomena.

2.1.2 Coaxial and Triaxial Surface Thermocouples

The most common probe used for temperature measurements in the internal combustion (IC) engine community is the coaxial surface thermocouple [30]. This type of probe was originally developed by Bendersky [31] for measuring gun barrel surface temperatures in 1953. Since then it has been refined for use in engine temperature measurements. It is constructed from standard metal thermoelements arranged in a coaxial configuration.

It consists of a wire of one thermoelement, coated with ceramic insulation, swaged tightly inside a tube of a second thermoelement. The junction is formed by a thin vacuum-deposited metallic layer on the surface. A diagram of a coaxial thermocouple is shown in Fig. 2.2.

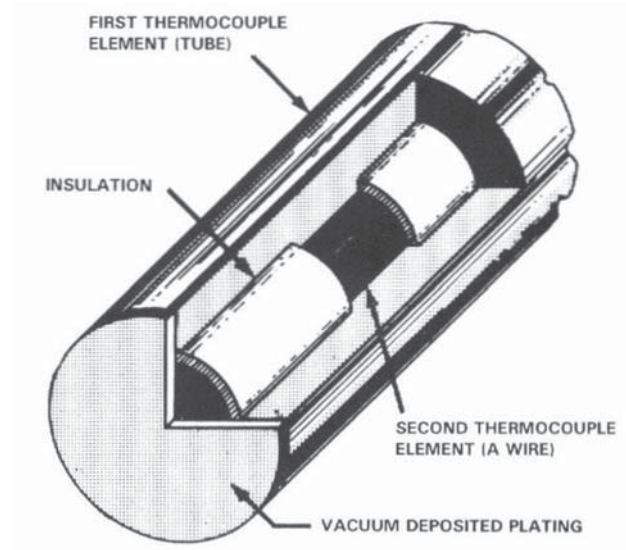


Figure 2.2: Diagram of a Coaxial Thermocouple [32]

Medtherm Corporation is the main manufacturer and supplier of this type of thermocouple. In addition to the standard coaxial configuration, they also offer a triaxial thermocouple with the option of a second junction a specified distance below the surface. In the triaxial configuration the outer thermoelement is also coated with a ceramic insulation and swaged inside a metal tube. This electrically insulates the thermocouple from the part it is installed in as well as limits radial heat transfer. A diagram showing a section view of a triaxial thermocouple is shown in Fig. 2.3.

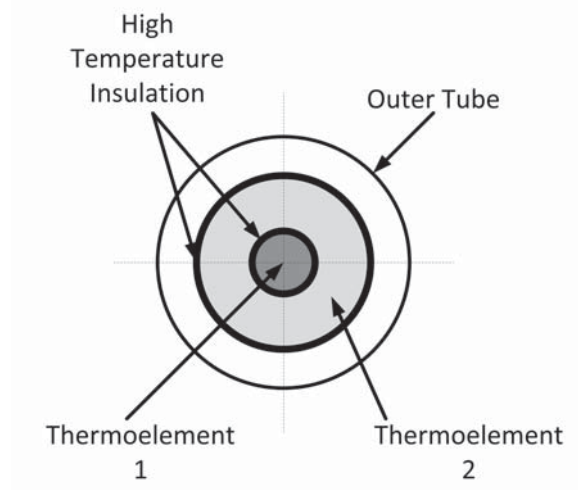


Figure 2.3: Section View of a Triaxial Thermocouple

The thermoelements commonly used for these types of sensors include iron, constantan, copper, nickel, and platinum. They are available in diameters under 1 mm and thus are well suited for use in small spaces. Their small size also allows multiple sensors to be installed in engine components, enabling the study of spatial variations of temperature and heat flux. With response times on the order of $1 \mu s$ [33], they can be used to achieve high temporal resolution measurements as well.

2.1.3 Pair-Wire Thermocouples

Pair-wire thermocouples are similar to triaxial thermocouples in that two thermoelements are separated by insulation and swaged together inside a tube; however, as the name implies, pair-wire thermocouples use two thermoelement wires installed next to each other instead of one wire inside a tube of the second thermoelement. A diagram showing a section view of a pair-wire thermocouple is shown in Fig. 2.4. The junction is made either by vacuum depositing a thin metallic layer on the surface or in some cases by abrading the surface to cold-weld slivers of each element together.

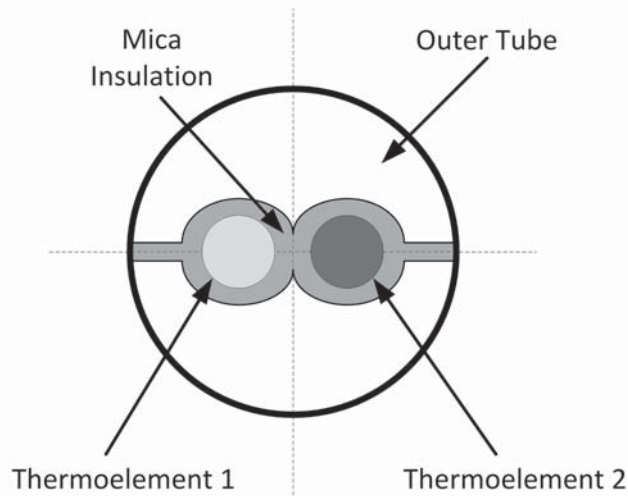


Figure 2.4: Section View of a Pair-Wire Thermocouple

There is also a special type of pair-wire thermocouple known as the eroding ribbon thermocouple [34]. These thermocouples have two flat ribbons of thermoelements instead of circular wires. The ribbons are separated and insulated by thin mica sheets and are pressed into a wide variety of substrates. A diagram of this type of thermocouple is shown in Fig. 2.5. The junction can be formed either by surface deposition or by abrading the surface. For coaxial and most pair-wire thermocouples the surface deposition method is preferred; however, the eroding ribbon thermocouple is really designed to use the abrasion technique. The "eroding" in its name refers to the ability to continually reform the hot junction as the surface erodes away.

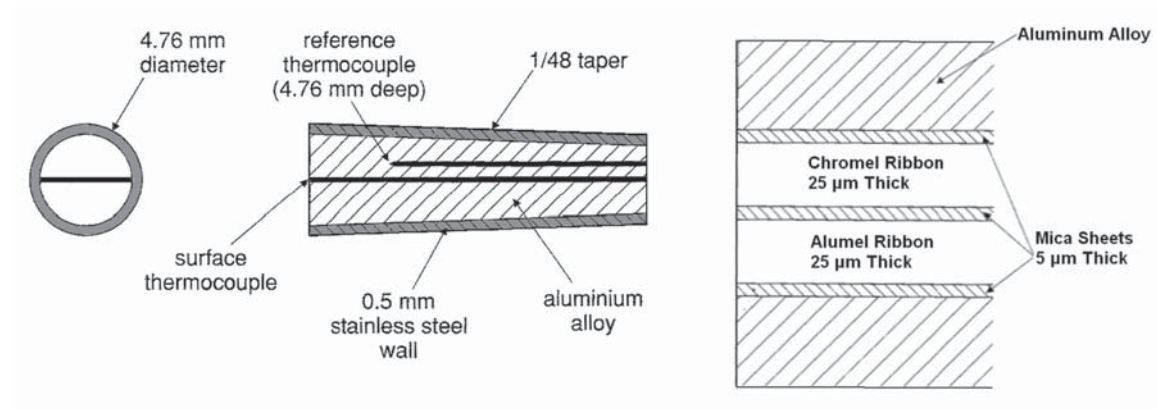


Figure 2.5: Diagram of an Eroding Ribbon Thermocouple [34]

Pair-wire thermocouples have many of the same benefits as coaxial thermocouples; however, they are typically larger in diameter. They also have slightly longer response times, typically on the order of $10 \mu s$ [34]. The eroding ribbon design is unique in that it is intended to remain functional even if the surface is worn away over time.

2.1.4 Thin Film Temperature and Heat Flux Sensors

Thin film platinum resistance temperature sensors were used by Wilson et al. [35] in 2002 to measure cylinder head and piston temperatures. The gauges were created by sputtering a $100 \mu m$ wide, $2 mm$ long, and $0.04 \mu m$ thick strip of platinum onto a $50 \mu m$ thick insulating layer of polyimide. A diagram of the sensor is shown in Fig. 2.6. A thermocouple embedded in the engine component was used to measure the metal surface temperature. The heat flux was calculated between the thin film gauge and the metal surface.

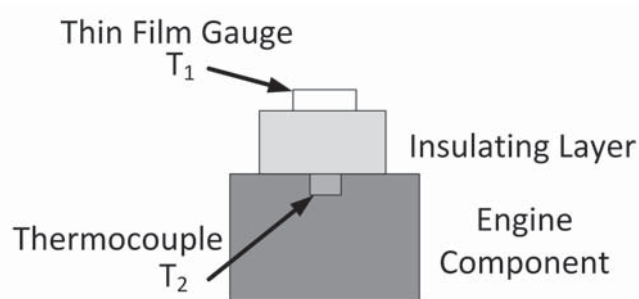


Figure 2.6: Diagram of a Thin Film RTD

A sensor using thin film thermocouples has been commercially developed by Vatel. It is designed to measure surface heat flux and operates as a differential thermopile. Two thermocouple materials are precisely deposited to form a structure of upper and lower thermocouples. This can be seen in Fig. 2.7. The thermopile formed by the upper and lower thermocouples provides a voltage output proportional to the heat flux. The actual surface temperature is measured using either a small thermistor or thermocouple. Several models of heat flux microsensors (HFM) are available with various materials and temperature ranges. The response time of these sensors varies from 17 to 300 μ s. These have been used successfully in engine applications [36].

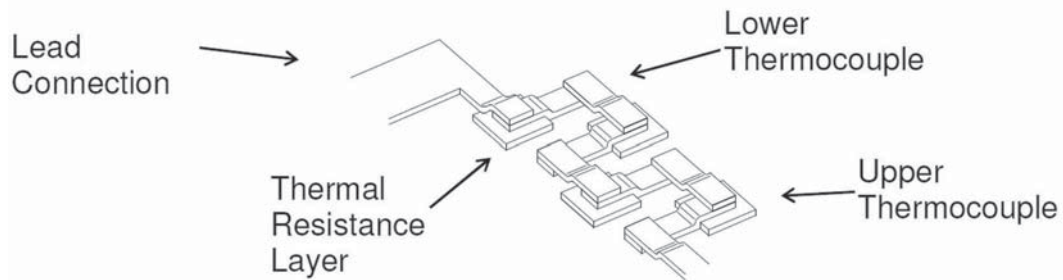


Figure 2.7: Diagram of a Vatel Heat Flux Microsensor (HFM) [37]

Thin film thermocouples and RTDs can improve the frequency response of surface temperature measurements and can be mounted without machining the part they are installed on; however, they tend to cover a fairly large surface area and caution must be taken to ensure this does not alter the flow field or boundary layer significantly. This is most often accomplished through film thicknesses on the order of a micrometer.

2.1.5 Mechanical Linkage Telemetry Systems

In order to make temperature and heat flux measurements on a piston in a running engine, some form of telemetry system is required to connect the sensor to a data acquisition system. This can be accomplished via a mechanical linkage to route the wires out of the engine or by some form of wireless data transmission.

Mechanical linkages known as "L-Links" or "Grasshopper Linkages" have been used by several researchers in the past [23, 38, 39]. An example of one is shown in Fig. 2.8. These linkages provide a solid connection, from the sensors to the data acquisition system, for

wires to be routed along. However, the linkage requires extensive modification to the engine and increases the imbalance significantly. Additionally, the wires are continually flexed during operation and are vulnerable to failure from fatigue. One of the key benefits is that all data channels are output continuously and not multiplexed like many wireless telemetry systems.



Figure 2.8: Image of Typical Linkage [23] *Reprinted with permission.*
Copyright ©2009 SAE International

2.1.6 Wireless Telemetry Systems

In the last twenty years, there have been numerous advancements in wireless telemetry techniques for internal combustion engines. Researchers have used electromagnetic induction [4, 40], Bluetooth network [5], and microwave [39, 41, 42] wireless telemetry systems to measure piston temperatures.

2.1.6.1 Electromagnetic Induction

Kato et al. [40] developed a piston temperature measurement technique using electromagnetic induction as the telemetry system. The system utilizes a resonator coil on the piston and transmitter and receiver coils on the engine block. Thermistors are

embedded in the piston and wired to the resonator coil. An alternating current is applied to the transmitter coil and when the piston reaches bottom dead center (BDC), current flows to the resonator coil via electromagnetic induction. The amount of current to the resonator coil is dependent on the resistance of the thermistor. As some of the current flows to the resonator coil, the amount of current through the receiver coil is decreased. The amount of this decrease can be correlated to the temperature of the thermistor. A diagram of this method is shown in Fig. 2.9. Up to six measurement locations per piston can be used with this system.

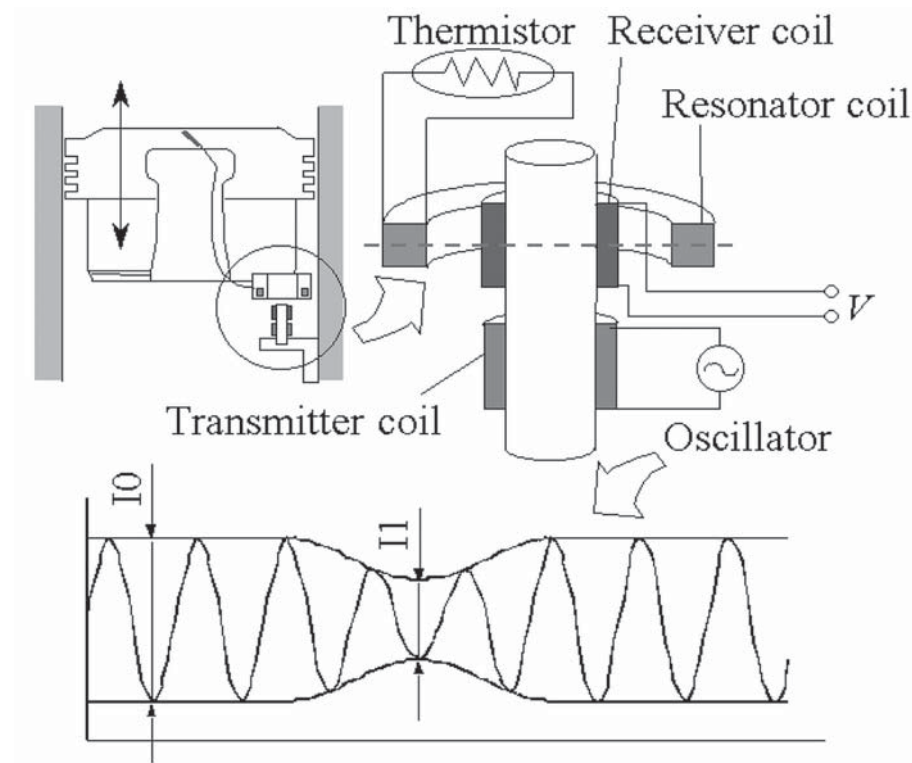


Figure 2.9: Diagram of an Electromagnetic Induction System [40]
Reprinted with permission. Copyright ©2001 SAE International

This method was successfully applied to measure piston temperatures in both spark ignited and diesel engines [40] as well as in a high speed 600 cm³ SI engine running at 15,000 RPM [4]. It has been proven to be accurate to within $\pm 2.5^\circ\text{C}$ and reliable even at high engine speeds. It is well suited to measuring in-depth piston temperatures that do not vary during a cycle. This limits its usefulness for surface temperature data collection since, even if a thin film thermistor was used, the temperature data would only be available within a

few crank angle degrees of BDC.

2.1.6.2 Bluetooth Network

Lee et al. [5] developed a multi-piston telemetry system using Bluetooth wireless networks. Thermocouples are mounted in the piston and the wires are run down to circuit boards mounted on the large end of the connecting rod. These circuit boards contain a 10 bit analog-to-digital (AD) converter, micro-controller, power board, and Bluetooth module. In order to supply power to the electronics a generator was constructed by attaching permanent magnets to the crankshaft counterweights and a coil on the connecting rod. As the magnets pass by the coil, a current is generated and used to power the electronics. A diagram of the system can be seen in Fig. 2.10.

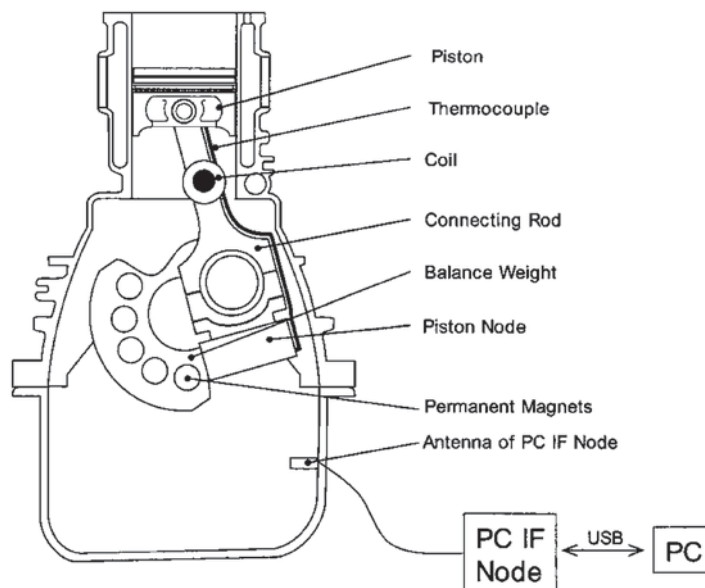


Figure 2.10: Diagram of a Bluetooth Piston Telemetry System [5]

The telemetry system is capable of collecting 16 multiplexed channels of thermocouple data on each of up to 56 pistons. The sampling rate is limited by the transfer rate of the Bluetooth module and was set to 100 Hz in their experiment. This system was tested on all four pistons of a 2.4 L four-cylinder light duty gasoline engine. It was able to successfully measure and record piston temperature data at five locations on the piston. The authors did note a limitation on the thermal loading of the Bluetooth module. The system cannot operate at temperatures above 120°C, therefore in some cases, some form of cooling system

may need to be applied to the electronic components mounted on the connecting rod.

2.1.6.3 Microwave Wireless Telemetry

Miers et al. [41] documented a wireless microwave telemetry data transmission technique in 2008. The telemetry system was developed by IR Telemetrics (IRT). It utilizes five main components: a multiplexer, a transmitter, a power supply, an antenna, and a receiver. The power supply can either be a battery pack or an inductive coil setup. The multiplexer acquires the signals, multiplexes them, and sends that signal to the transmitter. The transmitter converts the multiplexed emf output to a frequency modulated, 10-50 kHz square wave. This signal is then used to modulate a voltage-controlled oscillator (VCO) operating at a nominal frequency of 2.5 GHz. The output from the VCO ranges from 2.49 to 2.51 GHz and is broadcast from the transmitter. This signal is then captured by the receiver via an antenna mounted in the engine block. The receiver then demodulates the signal back to the 10-50 kHz square wave and then back to an analog voltage.

The system is capable of collecting up to 15 channels of multiplexed transducer data. The system is calibrated to an accuracy of $\pm 2\%$ for thermocouples and $\pm 1\%$ for thermistors. It has a bandwidth of up to 10,000 Hz but often a 2,000 Hz low-pass filter is employed to improve signal quality. It has been used successfully in single cylinder [39], light-duty [42] and heavy-duty [29] diesel engine applications.

2.2 Applications of Temperature and Heat Flux Measurements in IC Engines

2.2.1 In-Cylinder Heat Transfer Modeling Studies

As mentioned previously the goal of many of the early studies using surface temperature and heat flux measurement techniques was to characterize and develop models for in-cylinder heat transfer rates [27, 43–47].

Nusselt studied heat transfer in a combustion bomb in the 1920s but engine heat transfer was first studied experimentally by Eichelberg [27] in 1939. He used thermocouples to measure surface temperatures and then computed the surface heat flux according to Eq.

2.1.

$$q_w'' = -\lambda \left(\frac{\partial T_w}{\partial x} \right)_{x=0} \quad (2.1)$$

He then proposed a method for calculating the cylinder wall heat flux using a novel heat transfer coefficient and the temperature difference between the combustion gases and the cylinder wall. His method modified the term $\sqrt[3]{p^2 T}$, originally proposed by Nusselt [48], to \sqrt{pT} in order to consider the influence of radiation. He tested his method on several two-stroke and four-stroke diesel engines and while it predicted the general trends, it still lacked accuracy.

Woschni [45] provides a summary of the heat transfer coefficients resulting from the work of Nusselt, Briling, Eichelberg, Pflaum, and Annand. He believed that the $\sqrt[3]{p^2 T}$ and \sqrt{pT} terms used by all of the previous authors except Annand were only applicable to free convection, while in an engine, forced convection was the actual method of heat transfer. Thus he proposed to add a term representing the gas velocity to the equation for the heat transfer coefficient.

LeFeuvre et al. [46] reviewed the work done by Nusselt, Eichelberg, Pflaum, Annand, and Woschni and studied how their correlations worked on instantaneous data, since the previous correlations were mostly based on time-averaged data obtained from energy balances. Coaxial thermocouples with a plated surface junction were used by LeFeuvre et al. to measure surface temperatures in the cylinder head and cylinder wall. They calculated the heat flux by representing the surface temperature as a Fourier series and then solving the governing partial differential equation for heat conduction through the cylinder head and walls. They found that none of the correlations provided a good fit of the experimental data; however, they noted that the correlations aim to predict a single heat transfer rate for the entire cylinder head area; while, in reality, there are large spacial differences in heat transfer.

More recently, Wimmer et al. [36] studied the accuracy of previous heat transfer correlations to experimental measurements. They investigated a number of different surface temperature and heat flux sensors before settling on using thin film resistance temperature sensors for their experiment. They experimented on both diesel and gasoline engines and compared the heat transfer results from the Fourier method to those from the heat

transfer correlations of Woschni, Hohenberg, Kleinschmidt, and Bergende. They found the correlations to have large errors especially during and just after combustion when cylinder pressure and temperature are both very high.

There have been many attempts to develop a model for the heat transfer coefficient for combustion chamber surfaces in IC engines; however, the assumptions required by these models are very different from reality. The large spatial variations in surface temperatures and heat transfer limit the effectiveness of any model that assumes uniformity. Instead, more complex 2-D and 3-D models are required to provide a more accurate representation of heat transfer inside IC engines. These increasingly complex models require spatially and temporally resolved data for development and validation.

2.2.2 Parametric Effects on In-Cylinder Temperatures and Heat Transfer

While the studies mentioned in the previous section were interested in developing a model to predict in-cylinder heat transfer; others have conducted research to determine and quantify the effects of various operating parameters on in-cylinder temperatures and heat flux.

Alkidas [47] examined the effects of speed, load, and combustion phasing on cylinder head heat flux in a spark ignition engine. He utilized surface thermocouples with a second reference thermocouple embedded a known depth from the surface. The surface thermocouples were of the eroding ribbon type, whose junctions were formed by abrading the surface to produce contacts between the two ribbon elements. He showed that the initial high rate of increasing heat flux correlated well with the calculated time of flame arrival at each of the four measurement locations. In motored studies, the phasing of the increasing heat flux was similar at all four measurement positions. This shows that, as expected, there are large spatial variations in the surface heat flux which are due to combustion non-uniformities stemming from the turbulent nature of combustion. This further proves that attempts by earlier researchers to provide a global heat transfer coefficient have inherent weaknesses. He also found that with increasing engine speed, the magnitude of peak heat flux also increases. In a study on the effect of spark timing, Alkidas found that advancing the timing from maximum brake torque (MBT) resulted in increased peak heat flux while retarding the timing from MBT decreased it. However; he found that the heat

flux values near the end of the expansion stroke were similar regardless of spark timing.

Hayes et al. [49] conducted similar studies on a 2.2 L four cylinder engine. They utilized coaxial surface thermocouples with an embedded thermocouple 4 mm below the surface. They used an abraded junction technique on the coaxial thermocouples instead of the more typical plated junction. They studied the effect of engine speed while running at wide open throttle (WOT) conditions as well as the effect of load at constant engine speed on surface temperature and heat flux rates in both the piston and cylinder head. Like Alkidas, they found that increasing the engine speed results in increased peak heat flux rates; however, the rate of increasing heat flux decreases at higher engine speeds. They observed a similar trend for peak surface temperatures. When varying the load, they found that peak temperatures occurred at WOT while in some cases the peak heat flux rate occurred around a load of 75% of WOT. This was likely due to differences in air fuel ratio at the two conditions. They also found that the piston heat flux and surface temperature values were considerably higher than those on corresponding locations on the cylinder head. Finally, they briefly discussed the effect of deposits on surface temperature and heat flux measurements. As run time increased and deposits formed, they observed a steady decline in peak heat flux. After 50 hours the peak heat flux at a given condition decreased by 50%. This highlights the impact of deposits on heat flux measurements in IC engines.

The effects of deposits on instantaneous temperature and heat flux measurements in HCCI engines have been studied extensively by Güralp et al. [23, 24]. They utilized coaxial thermocouples with a vacuum deposited surface junction to measure piston surface temperatures. In as little as 10 hours, they saw a significant effect on the measured surface temperature profile from deposit formation. This can be seen in Fig. 2.11. From the plot it can be seen that the magnitude and phasing of the peak are effected. The peak temperature is decreased and the location of the peak occurs later.

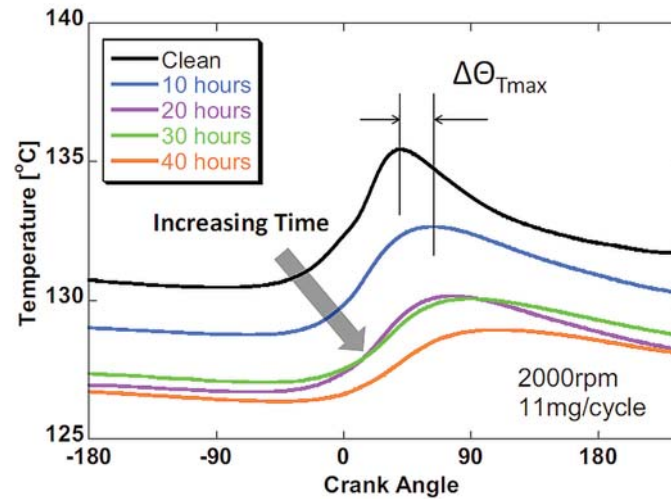


Figure 2.11: Plot of the Evolution of Measured Surface Temperature Profiles with Deposit Formation [23] *Reprinted with permission. Copyright ©2009 SAE International*

The authors were able to find a way to alter the engine conditions to compensate for the effect of deposits. By decreasing the intake air temperature and thus slowing combustion, they were able to match the rate of heat release curve to that of a clean piston. This solution is not practical for most testing, but it is interesting that there is a way to compensate for the effects of deposits, at least with respect to the heat release profile.

Enomoto et al. [50] investigated the effect of uncooled EGR on combustion chamber wall surface temperatures in a DI diesel engine. They utilized pair-wire thermocouples with a silver bead on the end that is machined flush with the measurement surface. They installed these thermocouples in the piston as well as the cylinder liner. They found that with increasing EGR ratio, the surface temperature increased slightly in all cases. While the magnitude of the increase in temperature was small, it is still counterintuitive since adding EGR should decrease combustion temperatures. The authors point to the increase in intake air temperature and decrease of the excess air ratio to explain the phenomenon. With cooled EGR, this trend may be reversed.

Boyce et al. [18] studied the effects of air fuel ratio on in-cylinder heat flux and temperatures in a small utility engine. They utilized a thermopile based heat flux sensor manufactured by Vatel to measure the surface heat flux on the cylinder head. In addition, standard type J thermocouples were installed 3 mm from the surface of the head. The air

fuel ratio was swept from 11.5 to 17.5 at several different engine conditions. It was found that the heat flux was highest for stoichiometric mixtures and decreased almost linearly on either side of stoichiometric. They found a similar trend on steady-state cylinder head and exhaust valve seat temperatures.

More recently, Suzuki et al. [4] investigated the effect of an oil cooling jet on piston temperatures. Using a thermistor embedded 2 mm from the backside of the piston and an induction telemetry system, the authors were able to collect piston temperature measurements at engine speeds up to 15,000 RPM. They found that the oil jet could reduce piston temperatures by up to 50°C; however, it was less effective at higher speeds. They also examined the effect of cooling by fuel enrichment and found that it was also more effective at lower engine speeds.

The effects of engine speed and load on in-cylinder heat transfer have been fairly well established; however, there is a lack of research and understanding of the heat transfer characteristics of modern GTDI engines that utilize lean air-fuel ratios and cooled EGR.

2.2.3 Identification of Fuel Impingement on the Piston

Miers et al. [42, 51] investigated fuel spray impingement on the piston of a DI diesel engine using triaxial surface thermocouples and a microwave wireless telemetry system. They found a unique signature in the surface temperature profile that they identified as impingement on the piston. However, the impingement was not of cool liquid fuel but instead was of the high temperature burning spray from the pilot injection. This high temperature burning spray caused a sharp rise in piston surface temperature at certain locations. When the fuel injector was rotated, the impingement signature did not occur, proving that the phenomenon was fuel spray related.

While studying the effect of deposits on surface temperature measurements in HCCI engines, Güralp et al. [23, 24] noticed a signature of liquid fuel spray impingement on the piston surface. On the thermocouples located close to the fuel injector tip, a sharp decrease in surface temperature was observed under certain engine conditions. The signature becomes even clearer when looking at the surface heat flux. When impingement occurs, a sharp spike in heat transfer out of the piston was seen. This was a result of the piston providing heat to vaporize the fuel that impinged on its surface. The plots of temperature and heat flux are shown in Fig. 2.12. At piston locations P1 and P7, the signatures of liquid

fuel spray impingement are evident.

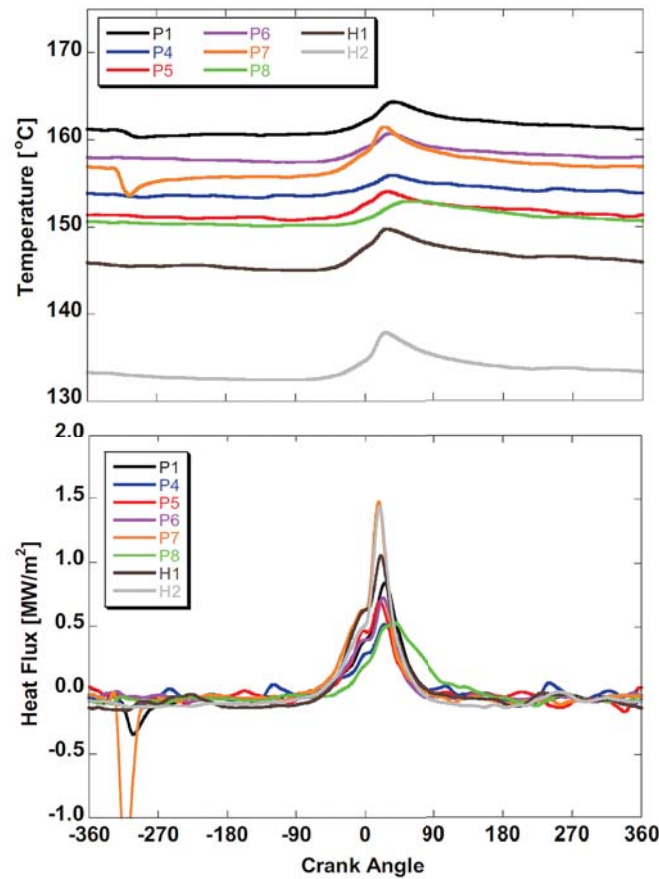


Figure 2.12: Plots of Piston Surface Temperatures and Heat Flux [23]

Reprinted with permission. Copyright ©2009 SAE International

2.3 Engine Energy Distribution

Energy flows into and out of internal combustion engines have been of interest since their inception. However, the recent push for improved high efficiency engines has led to more research into this area. This research varies from purely theoretical thermodynamic analysis of engine concepts to experimental testing. A commonly used assumption for the energy balance of IC engines is known as the "rule of thirds" and states that the fuel energy into the engine is output in even thirds to the crankshaft, coolant, and exhaust. This is a decent "rule of thumb" for simple calculations; however, the energy distribution varies significantly depending on the operating conditions of the engine. An example of this is illustrated in Fig. 2.13. Under constant speed but varying load, the energy distribution

changes dramatically.

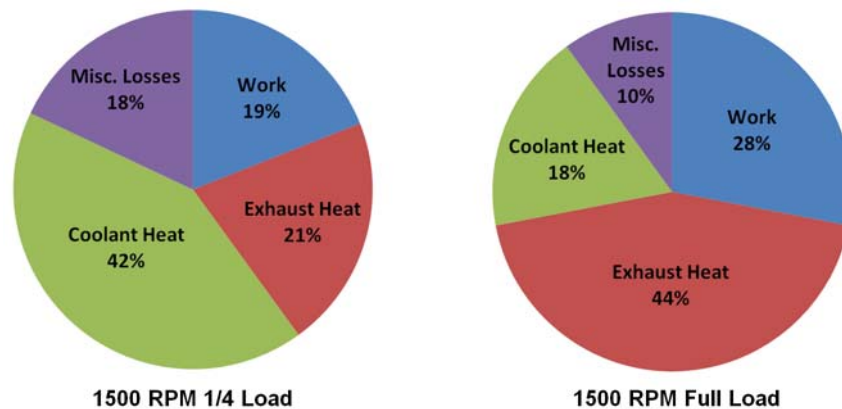


Figure 2.13: Energy Distribution for a 1.4L SI Engine [52]

Jerald Caton has published numerous papers on theoretical first and second law analyses of internal combustion engines [20,21,53–55]. He had developed a thermodynamic engine cycle simulation in previous research and in [53] used this model to analyze the effects of speed and load on the energy balance of an SI engine. He compared the fractions of fuel energy transferred to brake work, exhaust energy, friction, and heat transfer. He found that at constant speed, increasing the load increased the fraction of brake work and exhaust energy and decreased the fraction of friction and heat transfer. At constant load, he found that increasing the engine speed increased the fraction of exhaust energy and friction and decreased the fraction of heat transfer.

In a later paper [21], Caton used an updated engine cycle simulation to study the effects of EGR on SI engine performance and energy distribution. In this work, he utilized the second law of thermodynamics to perform an availability analysis. He found that the addition of cooled EGR decreased the heat transfer out of the engine and improved brake thermal efficiency. He also noted a decrease in the amount of availability exiting via the exhaust gases and an increase in the amount of availability destroyed by the combustion process.

In his most recent paper on the topic [56], Caton compared the effects of dilution from lean operation with that from EGR. He used engine simulation software that took into account the thermodynamic effects of dilution; however, the parameters for the Wiebe function based combustion model were not adjusted for dilution. He found that the use of EGR decreased the combustion temperatures more than dilution from lean operation. However, he showed that for the same peak temperature decrease, lean operation resulted in a higher

brake thermal efficiency (BTE). For a 10% peak temperature decrease, he found that the BTE for lean operation was 46.6% while for EGR it was only 45.4%. He showed that this difference was most likely caused by the differences in the ratio of specific heats (γ or "gamma") between the two methods of dilution. Both methods increase gamma during the compression stroke; however, during the exhaust stroke only lean operation has a higher gamma compared to normal operation.

Farrell et al. [7] utilized GT-Power engine simulation software to study the potential of high efficiency gasoline engine concepts. The three engines they considered were a 3.0 L port fuel injected (PFI) engine with a compression ratio (CR) of 10, a slightly downsized 2.9 L lean burn direct injection (LBDI) engine with a CR of 12, and a 2.7 L ultra lean burn direct injection (ULBDI) engine with a CR of 16. They found that at part load, the LBDI and ULBDI engines had much lower exhaust and cylinder heat losses which resulted in higher brake thermal efficiencies. They concluded that the decrease in combustion temperatures from lean operation caused the reduced heat transfer out of the cylinder and the exhaust. They also note that efficiency was also improved as a result of reduced pumping losses during lean operation.

Xin and Zheng [57] investigated methods to evaluate engine heat rejection. They proposed two control volumes that could be used to analyze the energy distribution in engines featuring turbocharging and exhaust gas recirculation. The first control volume has the boundary for gas flows set at the compressor inlet and turbine outlet and at the fuel tank for fuel flow. If low pressure loop EGR is used the boundary is set after EGR pick-up. The other control volume sets the boundary for gas flows at the intake manifold and turbine inlet and for fuel flow at the fuel tank. If high pressure loop EGR is used the boundary is set before EGR pick-up. The authors were able to use the resulting energy balance equations along with GT-Power engine simulations to evaluate and develop a model for miscellaneous heat losses. As a result, it was then possible to determine the coolant heat rejection from a gas side energy balance. This potentially allows for a more accurate determination of the coolant heat rejection since the uncertainty in thermocouple measurements is less of a factor for the high temperature exhaust gases compared to the lower temperature coolant.

Smith et al. [58] performed a first law energy balance on a modern diesel engine. They quantified the energy flows into the engine from the fuel enthalpy and out of the engine via the coolant, oil, exhaust gases, charge cooler, and crankshaft. The analysis was done

on both the absolute energy as well as values normalized as a fraction of fuel energy. They performed steady state engine tests across the entire operating map. They found that increasing the load resulted in an increase in brake thermal efficiency up to about 80% of the rated load; however, at 100% rated load the efficiency dropped slightly. The trends for the coolant heat rejection and the exhaust energy were different between data sets taken at 2000 and 4000 RPM. For the lower speed case, the fraction of energy in the coolant increased while the fraction of exhaust energy decreased consistently with load. At 4000 RPM, the fraction of coolant energy decreased as load increased up to 80% and then increased up to 100% load. The fraction of exhaust energy decreased as the load was increased to 60% but increased for higher loads. This inconsistency in the trends with load could potentially be explained by changes in air fuel ratio with load. At light load, diesel engines run very lean; however, as load is increased the air fuel ratio gets closer to stoichiometric and as a result, the combustion temperatures increase.

Fu et al. [59] performed an experiment to characterize both the 1st law energy distribution as well as the 2nd law exergy distribution of a modern four cylinder engine. Over a large map of engine conditions, both the absolute and relative values for the energy and exergy distribution were presented. One of the important conclusions was that the waste heat recovery potential of the coolant was low despite its large amount of energy. This was a result of the low temperatures associated with the cooling system. They also showed that if all the available waste heat energy was recovered, gasoline engine thermal efficiencies could reach nearly 60%.

Most of the work on this topic in the literature was of a theoretical nature and had been studied using simulation software. While this research is extremely valuable, the results need to be verified with physical engine testing. The experimental work that has been completed was mostly on compression ignition engines and so there was a need for more testing to be completed on modern spark ignition engines, especially under lean and dilute conditions. Additionally, the classical "rule of thirds" energy distribution has become outdated as a result of advancements in lean and dilute combustion. Updated information for engine energy distributions would be useful for initial estimates of coolant and exhaust system requirements.

Chapter 3

Method/Test Plan¹

3.1 Experimental Setup

This research required the design and setup of a test cell with the proper equipment and instrumentation. The test cell was created by modifying an existing engine test cell at Michigan Tech to fit the specific needs of this research. The research engine was provided by Ford Motor Company and was mounted on a movable engine cart. The engine cart and test cell were developed to facilitate fast engine swaps.

3.1.1 Test Cell Setup

An existing engine test facility at Michigan Tech was modified extensively to suit the specific needs of this research. The core pieces of the test cell were the engine, dynamometer, fuel system, cooling system, air intake/exhaust system and engine control system.

3.1.1.1 Engine and Dynamometer

The instrumented engine was a 3.5 liter, six cylinder, twin turbocharged, direct injection, spark ignition engine. Research engine specifications are listed in Table 3.1.

¹The material contained in this chapter is planned for submission as part of a journal article and/or conference paper in the future.

Table 3.1
Engine Specifications

No. of Cylinders/Configuration	6, 60° V
Bore x Stroke	92.5 mm x 86.7 mm
Displacement	3.5 L
Compression Ratio	10.0:1
Aspiration	Twin Garret GT15 Turbochargers
Maximum Boost Pressure	0.82 bar
Fuel Delivery System	High Pressure Direct Injection
Maximum Fuel Rail Pressure	150 bar
Rated Power	272 kW @ 5550 RPM
Peak Torque	475 N-m @ 1500-5250 RPM
Power Density	78 kW/L

The engine was equipped with variable intake cam timing that could advance the timing by up to 40 CAD from the base timing.

The dynamometer selected for this project was a 500 hp, 6000 RPM eddy current system from GE. An Omega LCCD-500 load cell, with a 500 lb (227 kg) capacity, was used to measure the force on the dyno's torque arm in order to calculate the engine torque. The dyno was controlled by a 0-10V analog signal supplied by a controller implemented in Labview. The dynamometer was water cooled and a Pohl Associates' Model A-600 cooling tower was used to regulate the temperature to approximately 30°C. The engine was mated to the dynamometer via a custom drive shaft fabricated by Raven Engineering.

3.1.1.2 Cooling System

The engine cooling system was designed to allow the engine to operate in a similar manner to its operation when installed in a vehicle. The original water pump circulated the coolant through the engine; however, instead of a conventional radiator, a two-pass shell and tube liquid-to-liquid heat exchanger was used. This allowed the engine to operate as a closed system with a 50/50 mix of ethylene glycol and water while the building side of the heat exchanger operated as an open system utilizing building water. In addition, a 15 psi (1.03 bar) radiator cap and overflow tank were installed in the engine coolant circuit to allow

for and regulate pressurization of the coolant. The temperature of the engine coolant was regulated by controlling the flow of building water through the heat exchanger. This was accomplished via a Belimo B213 valve operated by a 0-10V analog signal controlled by an Omega PID temperature controller. The coolant outlet temperature was set to 82°C (180°F). A turbine flow meter was installed in order to measure the coolant flow rate. A schematic of the cooling system can be seen in Fig. 3.1.

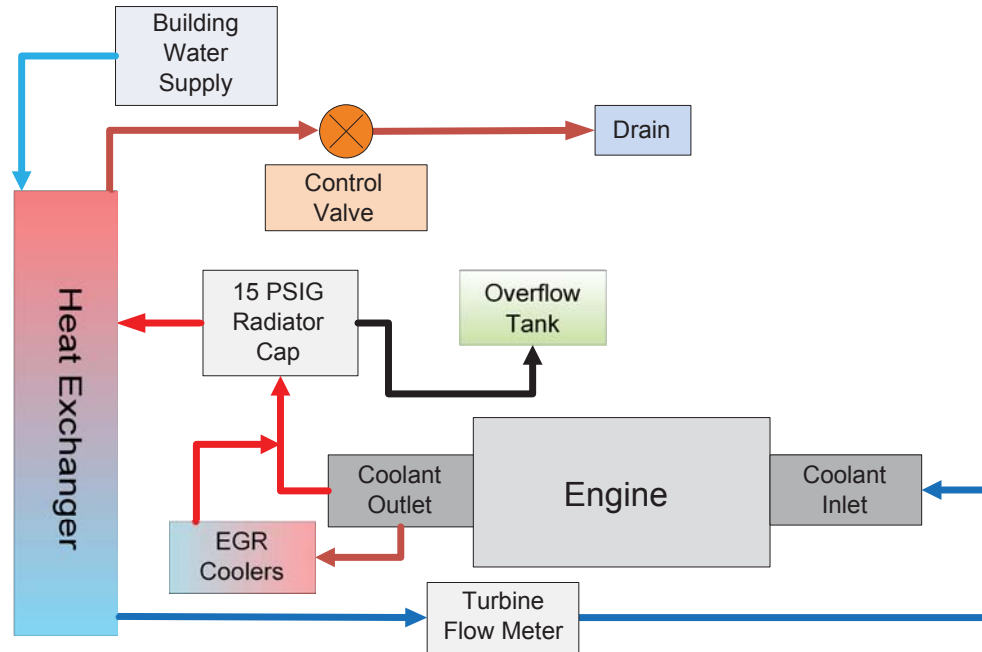


Figure 3.1: Cooling System Schematic

3.1.1.3 Air Intake/Exhaust System

The intake system for the engine was custom designed to allow for the installation of a low pressure loop cooled EGR system. A schematic showing the EGR system can be seen in Fig. 3.2. The EGR coolers were liquid-to-air heat exchangers that used engine coolant as the liquid. They were used to cool the hot exhaust gases from over 500°C to 85-90°C.

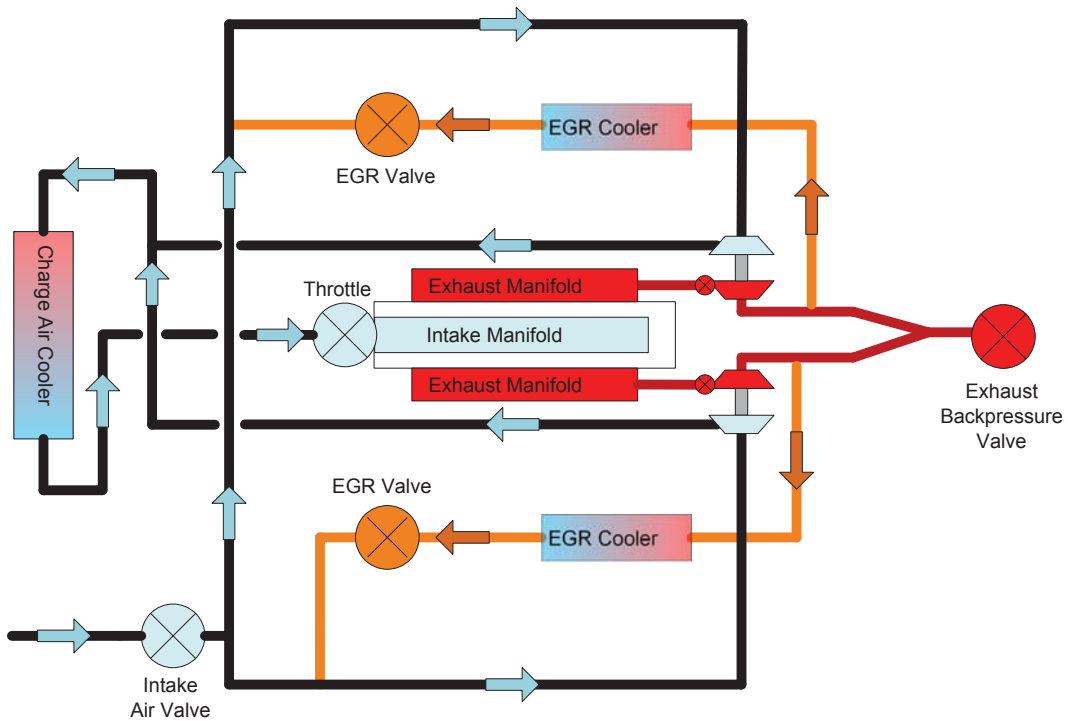


Figure 3.2: External Low-Pressure Cooled EGR System Schematic

The intake air to the engine was filtered and then fed through a Merian 50MC2-4 laminar flow element (LFE), with a flow range of 0-11,300 LPM. Additional pressure, temperature, and humidity sensors allow for the measurement of mass air flow. A schematic of this portion of the intake system is shown in Fig. 3.3.

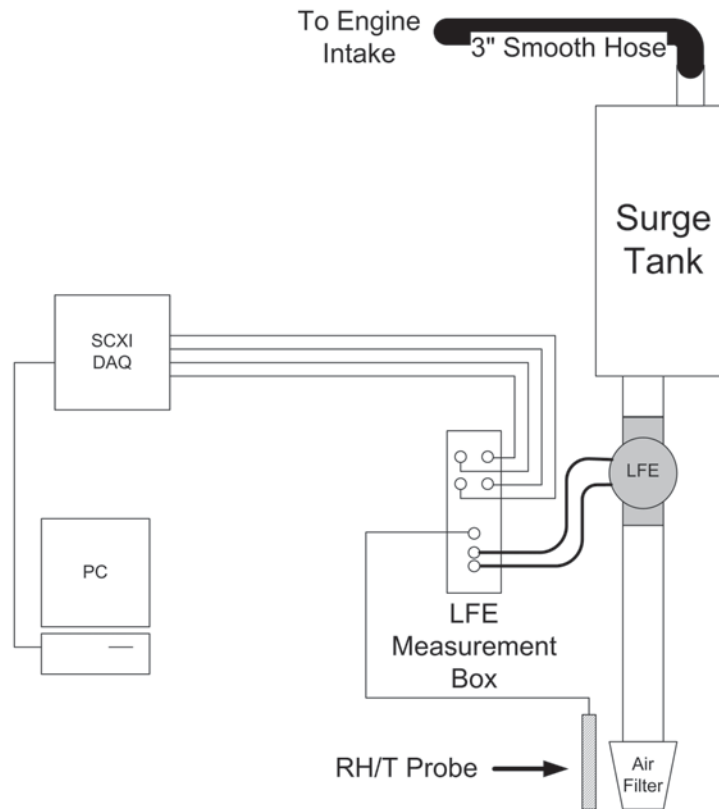


Figure 3.3: Air Intake System Schematic

The exhaust system removed the research engine's exhaust from the test cell without affecting the air flow out of the engine. It utilized exhaust fans and ducting in the building to create a vacuum that pulled the exhaust gases through ductwork and out the roof of the building. In order to simulate the back pressure normally created by a muffler and catalytic converter, a butterfly valve, controlled by a servo motor, was installed in the exhaust system. Three inch and four inch stainless steel exhaust tubing was used to route the exhaust gases from the turbo outlet to the test cell exhaust pipe.

3.1.1.4 Fuel System

The engine required a return-less fuel system that supplies fuel at a pressure of 55 psi (3.8 bar). To accomplish this, a portable fuel system with a Micro Motion Coriolis flow meter was used. The flow meter provided an accurate mass flow rate measurement. This system was used to feed the mechanically driven high pressure fuel pump that was on the

engine. This pump provided the 20 to 150 bar fuel rail pressures required for gasoline direct injection.

The test fuel used for this research was regular 87 AKI (Anti-Knock Index) E10 fuel purchased from a local gas station in one large batch. The fuel was sent out for analysis and the results are shown in Table 3.2.

Table 3.2
Test Fuel Specifications

Research Octane Number (RON)	92.3
Ethanol Concentration	9.59% v/v
Grabner Vapor Pressure	9.40 psi
Lower Heating Value	41.825 MJ/kg
Density	0.7404 g/mL
Carbon Mass Fraction	82.84%
Hydrogen Mass Fraction	13.59%
Oxygen Mass Fraction	3.57%

3.1.1.5 Engine Control

The engine was controlled by an ECU (Engine Control Unit) with an attached memory emulator to allow for real time changes to engine parameters. This hardware was utilized along with ATI (Accurate Technologies Inc.) Vision software. This combination enabled real-time control and recording of nearly all engine operating parameters. Some of the parameters that were controlled during testing were the throttle position, global and individual cylinder spark advance, global and individual cylinder air-fuel ratio, SOI (start of injection), and intake cam phasing angle. Many other ECU parameters were also monitored and recorded during testing.

In addition to the main engine ECU, a second Mototron ECU was used to control the custom external EGR system. MotoTune was used to create a calibration and display file that read data from UEGO (Universal Exhaust Gas Oxygen) sensors installed in the intake and exhaust systems and determined the EGR rate. This ECU and software controlled the EGR rate by modulating PWM signals that controlled the two EGR valves and an air intake valve. The parameters in MotoTune were also monitored and recorded during testing.

3.1.2 Engine Instrumentation

The engine was instrumented with type K thermocouples, RTDs, and standard pressure transducers for low-speed data collection. The low-speed measurements were sampled at 2 Hz. A summary of the low-speed measurements can be seen in Table 3.3.

Table 3.3
Low-Speed Measurements

<u>Pressure</u>	<u>Temperature</u>
Ambient	Ambient
Throttle Inlet	Intake Pre-Intercooler
Intake Manifold	Intake Post-Intercooler
Exhaust Pre-Turbine (2)	Throttle Inlet
Exhaust Post-Turbine (2)	Cylinder 2 Intake Runner
Oil	Individual Cylinder Exhaust (6)
	Exhaust Pre-Turbine (2)
	Exhaust Post-Turbine
<u>Other</u>	
Fuel Flowrate	Engine Coolant Inlet (RTD)
Air Flowrate	Engine Coolant Outlet (RTD)
Engine Coolant Flowrate	Heat Exchanger Water Outlet
Ambient Relative Humidity	EGR Cooler Inlet (2)
Engine Speed	EGR Cooler Outlet (2)
Engine Torque	Oil

To collect high-speed data for combustion analysis the engine was instrumented with in-cylinder pressure transducers, an optical encoder, and high-speed intake and exhaust pressure sensors. In addition, current probes were used to gather spark and fuel injector timing signals. Additionally, a custom system for measuring the relative air fuel ratio of each individual cylinder was constructed and used for testing. A summary of the high-speed instrumentation is shown in Table 3.4.

Table 3.4
High-Speed Instrumentation

<u>Parameter</u>	<u>Product Used</u>	<u>Specifications</u>
Cylinder Pressure	Kistler 6125A	Range: 0-250 <i>bar</i> absolute
Cyl. 2 Intake Runner Pressure	Kulite ETL-173B-190-2BarA	Range: 0-2 <i>bar</i> absolute
Cyl. 2 Exhaust Port Pressure	Kulite EWCTV-312M-3.5BarA	Range: 0-3.5 <i>bar</i> absolute
Manifold Air Pressure	Omega PX209-030A5V	Range: 0-30 <i>kPa</i> absolute
Engine Position	Encoder Products Model 260	Resolution: 0.5 CAD
Spark Timing Signal	Fluke 80I-110S	Sensitivity: 100 <i>mV/A</i>
Fuel Injection Signal	Fluke 80I-110S	Sensitivity: 100 <i>mV/A</i>
Individual Cylinder Lambda	Bosch LSU4.2 Sensors Innovate LC-1 Controllers	Accuracy: $\pm 0.007 \lambda$

3.1.2.1 Combustion Chamber Temperature and Heat Flux Instrumentation

Several components of cylinder 2 were instrumented with specialized equipment designed to characterize the temperature and heat transfer distribution of the combustion chamber. The piston was equipped with Medtherm fast response surface thermocouples as well as embedded and underside thermocouples. Triaxial type J thermocouples, with a sliver junction, were used to measure the surface temperatures. These thermocouples had a response time on the order of one microsecond. They also had a second junction a specified distance from the surface, which allowed for a second measurement of temperature and thus the ability to calculate heat flux. Four of this type of thermocouple were installed in the piston (STC 2_10, 3_11, 6_12, 7_13). Five thermocouples with only a surface temperature measurement were also installed (STC 1,4,5,8,9). In addition, there were two thermocouples mounted on the underside of the piston (UTC 14,15). In total, there were fifteen temperature measurement locations on the piston. The locations of these thermocouples can be seen in Fig. 3.4 and the actual implementation on the piston can be seen in Fig. 3.5.

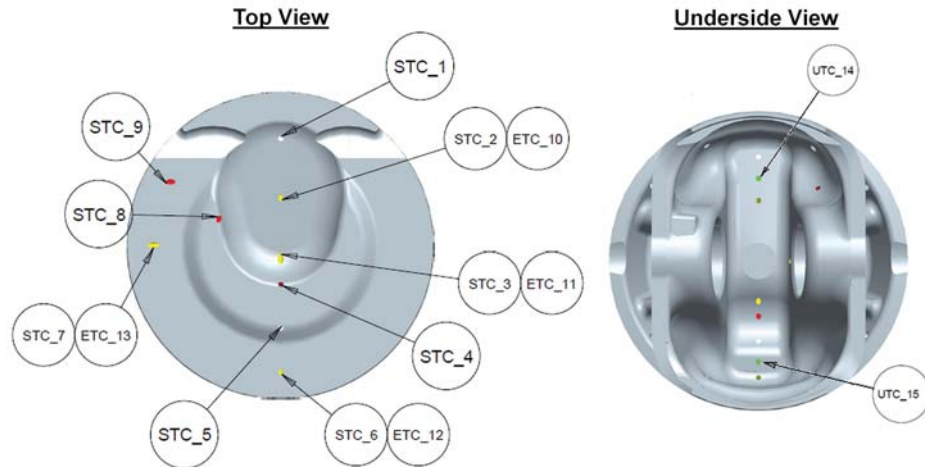


Figure 3.4: Schematic of Piston Thermocouples. Surface thermocouple (STC), embedded thermocouple (ETC), and underside thermocouple (UTC) locations are labeled.

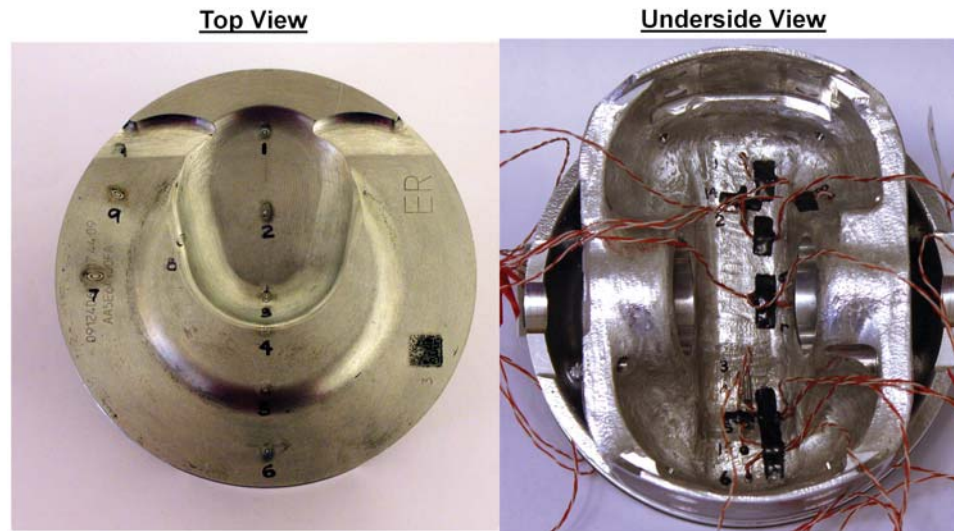


Figure 3.5: Photographs Showing Piston Thermocouple Installation

The cylinder liner was equipped with two fast response surface thermocouples located close to mid-stroke and the cylinder head had a heat flux transducer and two fast response surface thermocouples installed. In the cylinder head, the surface thermocouples were located in the exhaust valve bridge and near the injector tip. The heat flux transducer was a fast response triaxial type J thermocouple with a second junction 4 mm below the surface,

mounted in a metal plug in the shape of a Kistler 6125 pressure transducer. This allowed the heat flux probe to be mounted in a cylinder pressure transducer port. Two of these ports were machined into the head of cylinder 2 to allow for both the heat flux probe and a cylinder pressure transducer. An image of the head with the thermocouple and heat flux probe locations can be seen in Fig. 3.6. Unfortunately, the surface thermocouple in the exhaust valve bridge was damaged during engine reassembly and was not operable during any testing.

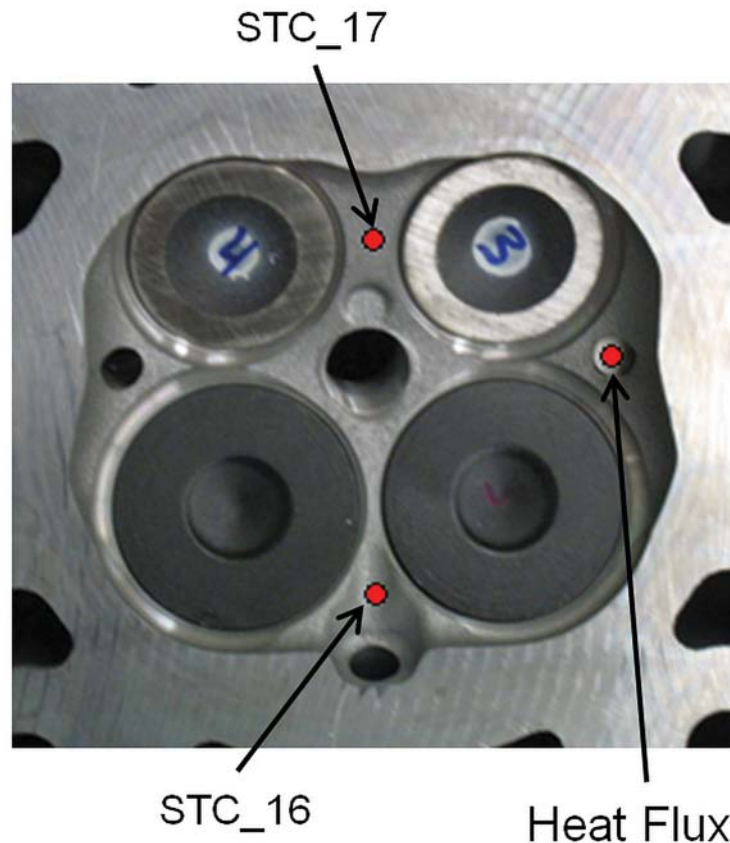


Figure 3.6: Image of Cylinder Head Showing Instrumentation Locations for Thermocouples and Heat Flux Sensor

3.1.3 Data Acquisition

There were several components to the overall data acquisition system for this project. For measurements of steady state variables, a low-speed NI SCXI data acquisition system was used along with Labview software. The NI SCXI system consisted of SCXI-1000

4-slot chassis, a SCXI-1600 16-bit 200kS/S USB DAQ module, a SCXI-1100 32-channel +/-10V differential input module, a SCXI-1102 32-channel thermocouple input module, and a SCXI-1126 8-channel frequency input module. This hardware was used along with a TC-2095 thermocouple terminal block and a BNC-2095 terminal block. This system was used to measure and record the low-speed temperature and pressure data as well as air flow, relative humidity, fuel flow, engine torque and engine speed. Additionally, the MotoTune and ATI Vision data was logged at a relatively slow speed by their respective software programs.

The high-speed pressure and temperature data required a different data acquisition system. A DSP Technologies ACAP system was used for this purpose. A breakdown of the components of the ACAP system are shown in Table 3.5.

Table 3.5
DSP Technologies ACAP System Components

Qty	Model	Description
1	Optima 860	25 Slot Chassis
2	4325	TRAQ Real Time Processor
2	5008	8192k Memory Module
4	2812 PMN100	8 Channel 12 Bit +/-10V 100 kHz Digitizer
1	2904A	Spincoder Timer/Counter
2	1642	Knock Module
1	6001	CAMAC Microprocessor
1	4012A	TRAQ System Controller

An optical encoder with 0.5 degree resolution was used as the engine position signal that triggered the ACAP system. A high-speed intake pressure transducer was used to determine the pressure used for pegging the in-cylinder pressure transducer in cylinder 2. The pressure transducer located in the intake manifold was used for pegging the other five cylinders. Pegging was done at 180°BTDC. A current clamp was used to acquire a spark timing signal that was used by ACAP for burn duration calculations. A second current clamp was used to measure the injection timing and injection duration for cylinder 2. The signals from high-speed thermocouples in the cylinder head and engine block were conditioned through an Ectron TC201 cold junction compensation circuit and then amplified by an Ectron model 563HL instrumentation amplifier. The amplifier specifications are shown in Table 3.6.

Table 3.6
Ectron Model 563HL Amplifier Specifications [60]

Parameter	Specification
Zero Stability	$\pm 4 \mu V$ RTI $\pm 0.25 mV$ RTO
Zero Temperature Coefficient	$\pm 1 \mu V/^{\circ}C$ RTI $\pm 0.35 mV/^{\circ}C$ RTO
Slew Rate	$> 6.3 V/\mu s$
Settling Time	15 μs to 0.1% of final value
Bandwidth (within 3dB)	DC to > 100 kHz
Noise	4 μV RTI + 0.5 mV RTO <i>rms</i>
Gain Accuracy	$\pm 0.1\%$
Linearity	$\pm 0.005\%$
Gain Steps	1, 2, 5, 10, 20, 50, 100, 200, 500, 1000

3.1.3.1 Wireless Telemetry System

In order to collect temperature data from the piston, a microwave wireless telemetry system was used. The system used in this experiment was developed by IR Telemetrics. The components mounted on the piston were the transmitter/multiplexer, an inductive coil, and the power electronics. A power coil was mounted in the crank case to supply power to the inductive coil in the piston. In addition, four antennas were mounted in the crankcase near the crankshaft to pick up the microwave signal from the transmitter and allow a receiver outside the engine to collect the data and transfer it to a computer. The typical setup can be seen in Fig. 3.7.

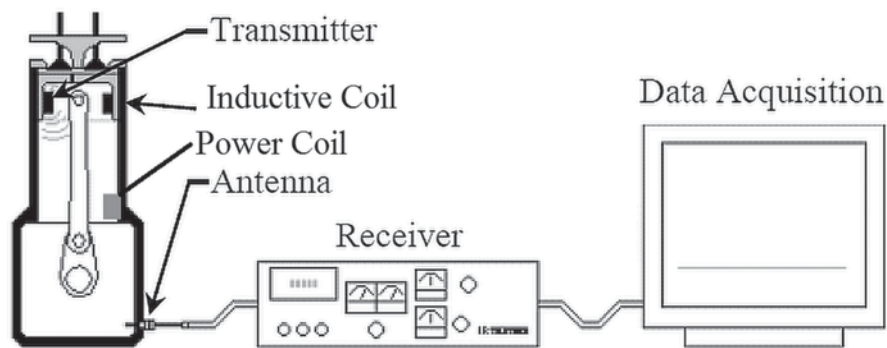


Figure 3.7: Wireless Telemetry Component Schematic [61]

The emf signals (mV) from thermocouples mounted in the piston are converted to a frequency (1st frequency modulation), multiplexed, used to modulate a microwave carrier (2nd frequency modulation), and finally transmitted via an antenna to a receiver. The double frequency modulation is very precise and was a key component of the accuracy of this system. The receiver captures the microwave signal, demodulates it to a square wave and sends the frequency of each pulse to a computer. The receiver also performs a frequency-to-voltage conversion and outputs an analog voltage. This conversion process also uses amplifiers and filters to reduce noise and improve signal quality [41]. The conversion process is shown in Fig. 3.8 and the installation in the piston for this test is shown in Fig. 3.9. Note that reading the frequency data prior to the voltage conversion is slightly more accurate. This is a result of the filters used during the frequency to voltage conversion. An error on one frequency pulse can affect the voltage signal for a longer period of time. In this research, both the frequency output and analog output were recorded. The frequency data was recorded by IRT's hardware and the voltage output was recorded by ACAP.

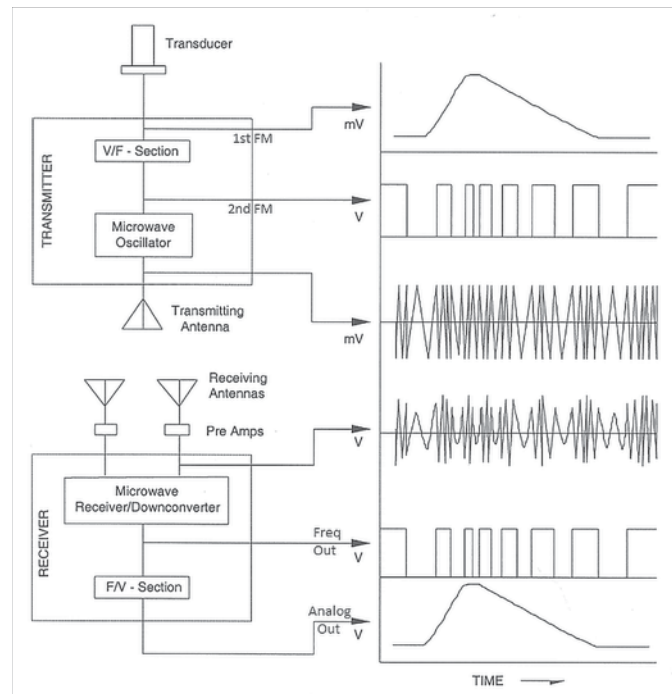


Figure 3.8: Microwave Wireless Telemetry Signal Conversion Process [61]



Figure 3.9: Installation of Wireless Telemetry Components on the Piston

The combination of these data acquisition systems enabled an in-depth study of internal combustion engine thermodynamics and heat transfer.

3.2 Initial Testing without Telemetry

Prior to being disassembled and sent out for high-speed thermocouple and wireless telemetry installation, the engine was broken in and preliminary data was recorded. Most of the low-speed temperature and pressure measurements were already installed at this stage; however, the coolant flow meter and individual cylinder UEGO sensors were not. The in-cylinder pressure transducers were installed and cylinder pressure data was recorded using a one degree encoder with the ACAP system.

The break-in procedure specified a gradual ramp up in speed and load until the main break-in point was reached. This point was then maintained for three hours and fifteen minutes. The break-in schedule can be seen in Table 3.7.

Once the engine was broken in, a series of baseline tests were conducted to verify the

Table 3.7
Engine Break-In Procedure

Speed	BMEP	Time
<i>RPM</i>	<i>bar</i>	<i>hr:min</i>
1500	2.5	0:30
2000	4.5	0:30
2500	7.0	0:30
2750	8.5	0:30
2750	10.0	3:15
2000	4.5	0:30

engine was operating within its performance specifications.

3.2.1 Baseline Performance

Baseline tests were performed and the results were compared to performance specifications received from Ford Motor Company. The tests were part of a "mini-map" that is indicative of the types of speeds and loads seen in many vehicle drive cycles. The test points and a comparison of the manufacturer optimized and actual BSFC (brake specific fuel consumption) results are shown in Table 3.8. Note that for the 600 RPM and 0.7 bar BMEP case the units of BSFC were g/L-hr instead of g/kW-hr. The BSFC results were within acceptable limits for this engine. The results were all about 3-5% higher than the manufacturer's specification; however, the test fuel for this research had a lower heating value of 41.8 MJ/kg compared to the 43.3 MJ/kg certification fuel used by the manufacturer. Additionally, the research engine likely had a higher work requirement for the water pump due to the EGR coolers and shell and tube heat exchanger, which also would have increased the BSFC.

While the BSFC results were reasonable, it was found that there was an up to 10% difference in fuel flow between the two engine banks. After analyzing the cylinder pressure data it was found that there was a small discrepancy in the exhaust valve opening and closing timing between the two banks. This resulted in different levels of internal EGR and thus different amounts of fresh air. This can be seen clearly in a plot of the log of cylinder pressure versus engine position. One example is shown in Fig. 3.10. The region of interest was the exhaust valve opening and blowdown process which is seen in Fig. 3.11. This plot

Table 3.8
Baseline Mini-Map Test Conditions and BSFC Results
(*BSFC units are g/L-hr)

Speed	BMEP	BSFC Opt.	BSFC Actual	BSFC Difference
<i>RPM</i>	<i>bar</i>	<i>g/kW-hr</i>	<i>g/kW-hr</i>	<i>%</i>
600	0.7	237*	254*	0.7
1000	1.5	416	440	5.8
1500	2.6	317	333	5.0
1500	5.0	259	273	5.4
2000	2.0	366	377	3.0
2000	5.0	263	270	2.7
3000	7.5	249	257	3.2

clearly shows the exhaust valves for cylinders 1, 2 and 3 (Bank 1) opening 8 to 10 degrees before cylinders 4, 5 and 6 (Bank 2). The clearance between the pocket in the cam timing gear and the mating tab on the camshaft was large enough to cause this difference (note that an error of 1 degree on the camshaft results in an error of 2 crankshaft degrees). This issue was solved by adjusting the camshaft timing gear shown in Fig. 3.12. The result of this adjustment can be seen in Fig. 3.13. After the adjustment, the fuel flow difference decreased to less than 4%.

Once this problem was fixed and the engine was found to perform satisfactorily in all other areas, it was removed from the test cell and disassembled before parts were shipped out for instrumentation.

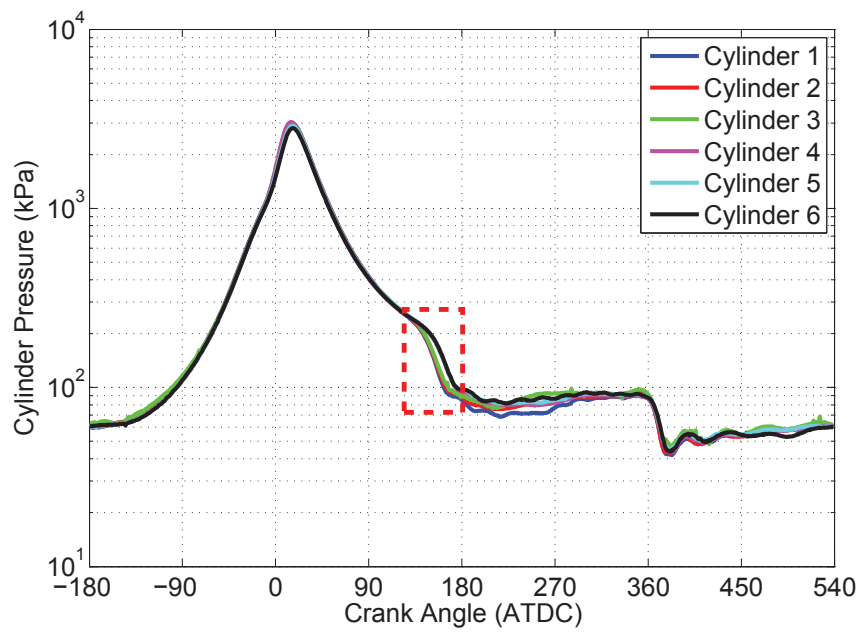


Figure 3.10: Plot of Cylinder Pressure vs Engine Position

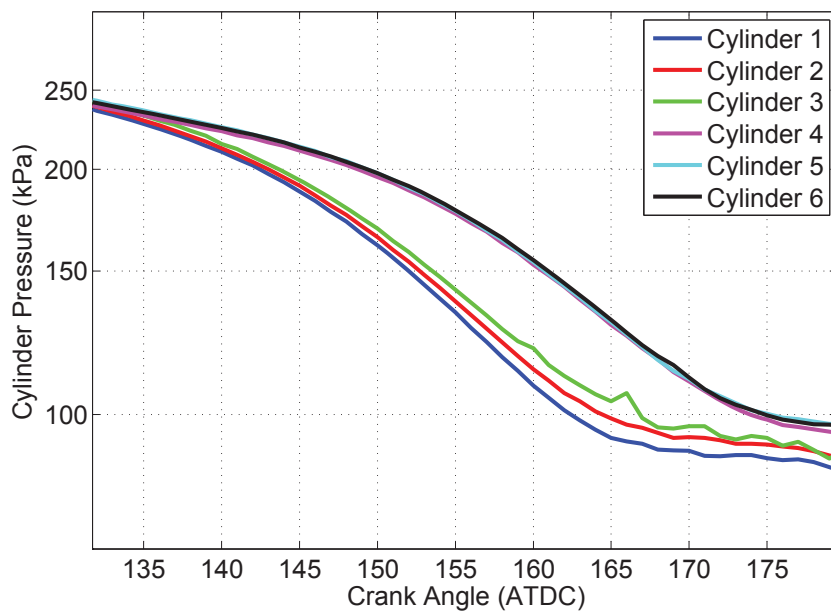


Figure 3.11: Zoomed In Plot Showing the Exhaust Valve Opening

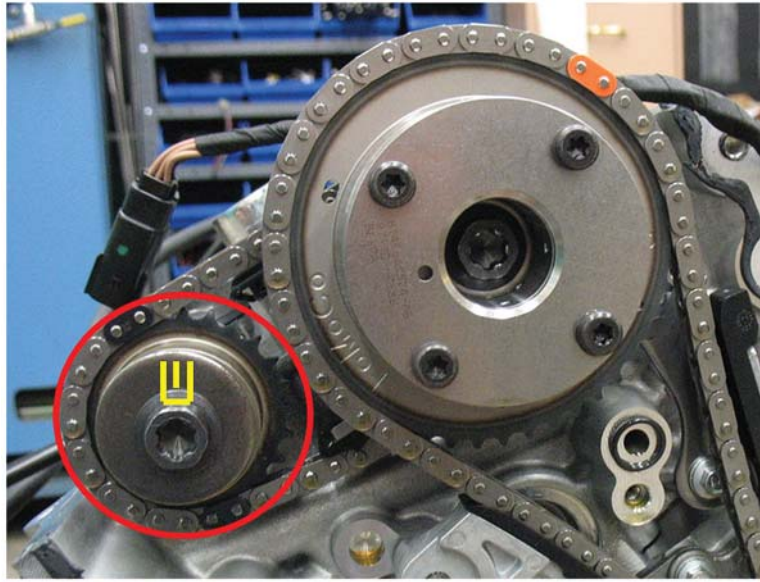


Figure 3.12: Photograph of Bank 1 Exhaust Cam Timing Gear

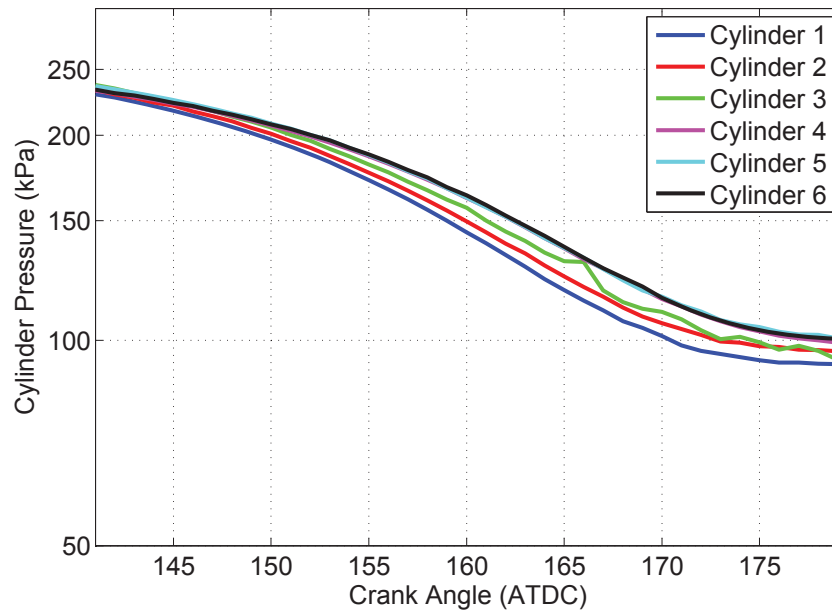


Figure 3.13: Zoomed In Plot Showing the Exhaust Valve Opening After Camshaft Fix

3.2.2 Lean and Dilute Combustion Testing on 2nd Engine

A nearly identical engine to the one that was used for this research was used for several other research projects in the test cell. The only difference between the two was the use of a VOIS (Variable Output Ignition System). This dual coil system allowed for control of the dwell and timing of each coil. Some data on lean and dilute combustion was completed on this engine and is presented here. This data was used to help define the test points for the specially instrumented engine.

EGR sweeps at several test points were conducted to determine the combustion stability and misfire limits. The combustion stability criteria used for determining the EGR limit was based on the COV (coefficient of variation) of gross IMEP. For loads above 2 bar BMEP, the COV limit was 2% and for loads below 2 bar, the COV limit was 5%. For these tests 300 cycles of combustion data was collected at each condition. Additionally, the test was repeated several times and the results are shown in Fig. 3.14. The EGR limit for the 1500 RPM and 2.6 bar BMEP condition was found to be 16%.

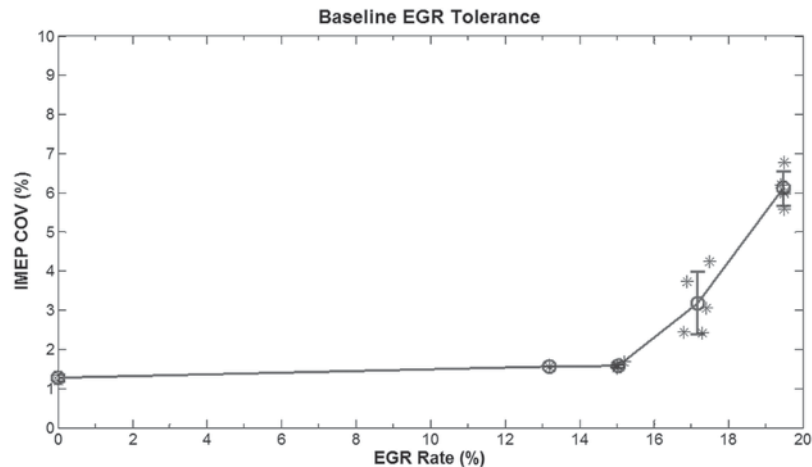


Figure 3.14: 1500 RPM and 2.6 Bar BMEP EGR Sweep. Error bars are ± 1 standard deviation.

In addition, some work was also done previously on lean combustion. The results from a lambda sweep at 1500 RPM and 2.6 bar BMEP are shown in Fig. 3.15. At this condition, the lean limit was found to be 1.38.

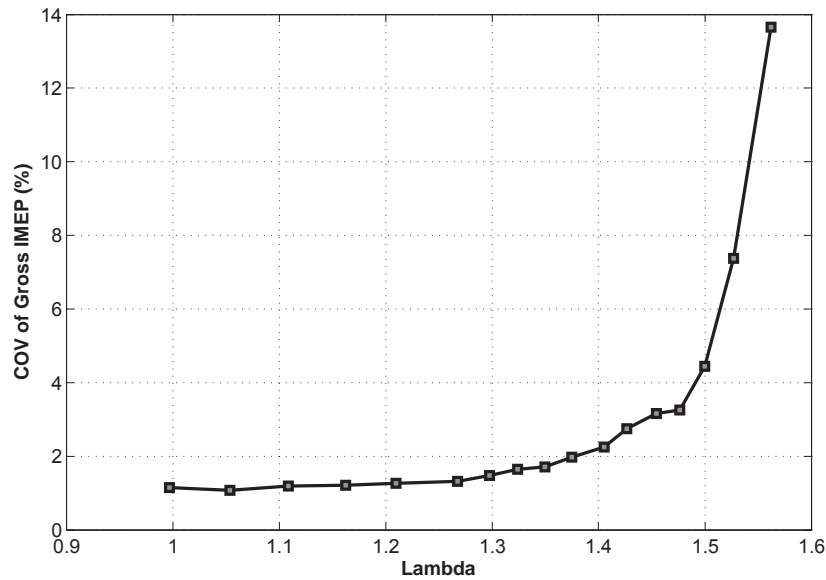


Figure 3.15: 1500 RPM and 2.6 Bar BMEP Lambda Sweep

The conditions of these two sweeps were under light load and low speed and thus should have some of the lowest EGR and lean limits on the engine map. These limits were used as a reference when deciding the EGR rates and lambda values used in this research.

3.3 Initial Testing with Telemetry

After the fully instrumented engine components were received, the engine was re-assembled and installed in the test cell. Another mini-map was conducted to verify the engine was performing within specifications. Once this was completed, initial testing was conducted and soon an issue with the telemetry system was encountered. The engine had to be removed from the cell and the piston had to be pulled from the engine. It was sent to IRT for diagnosis and it was found that some of the capacitors had shorted out, requiring new telemetry components to be installed on the piston. After this was completed, the engine was again re-assembled and installed in the test cell. A third mini-map was conducted and again verified that the engine was performing within specifications.

With the engine and telemetry system up and running properly, testing was resumed. After about 2 weeks of data collection, the initial data was processed and an issue with the surface thermocouple response was discovered. It appeared that the dynamic response of the surface thermocouples was degrading significantly. A comparison of the response

of one of the surface thermocouples over time is shown in Fig. 3.16. From studying the literature, it was known that surface deposits could cause this type of effect. To verify that the effect was a result of carbon deposits on the piston, a cleaning procedure was tested on the piston. The spark plug was removed and with piston at about mid-stroke, an acetone based brake cleaner was sprayed onto the piston. After the procedure, the spark plug was installed and the engine was run again at the control point. The results from before and after the cleaning are shown in Fig. 3.17. The results clearly indicated that it was a carbon deposit problem and that the cleaning procedure was effective in restoring the thermocouple response. This cleaning process was performed often during testing in an attempt to maintain the fast response time of the thermocouples; however, the effectiveness of the cleaning procedure varied from time to time and also did not affect all thermocouple locations equally.

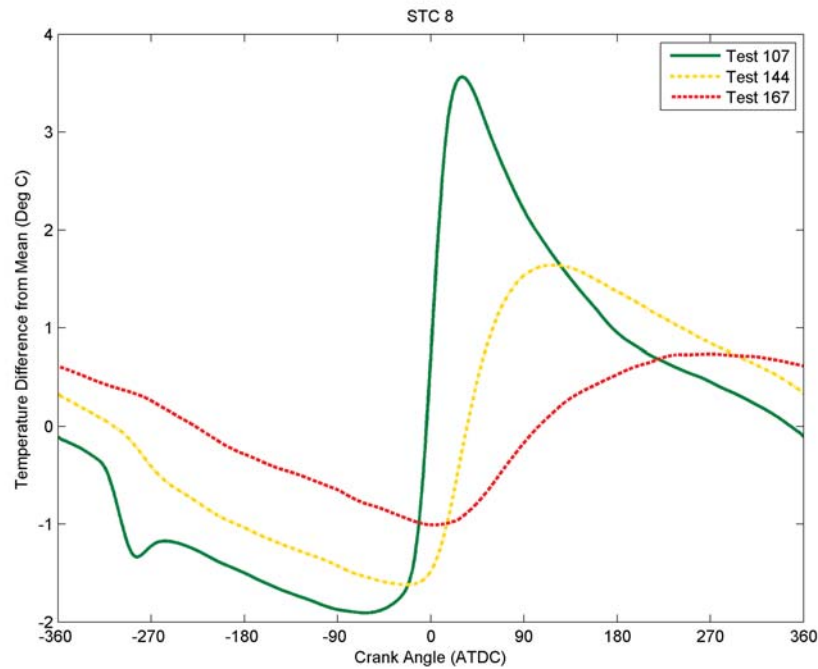


Figure 3.16: Comparison of Normalized Piston STC Response

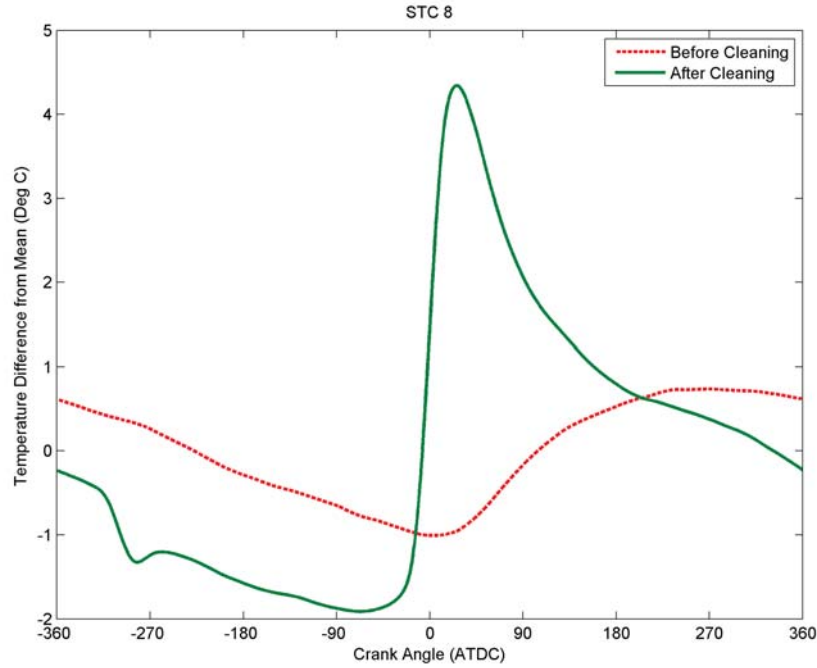


Figure 3.17: Normalized STC Response Before and After Cleaning

3.4 Test Plan and Procedure

This project's overall goal was to characterize the temperature and heat transfer distribution in the combustion chamber of a modern GTDI engine. Specialized instrumentation allowed for high-speed measurements of piston, cylinder liner, and cylinder head temperatures and heat fluxes. In addition, a large number of low speed temperature, pressure, and flow measurements allowed for the characterization of the overall energy distribution of the engine. For this research several specific tests were chosen to quantify the effects of different parameters on heat transfer and temperature distribution.

3.4.1 Global and In-Cylinder Temperature and Heat Transfer Characterization

The bulk of this research focused on characterizing the effects of lean and dilute combustion on both the combustion chamber temperatures and heat transfer as well as the overall energy balance of the engine. A test matrix was determined based on design of experiments (DOE) principles for a partial factorial test. Engine speed, engine load, relative AFR,

and EGR were the four factors. Engine speed, relative AFR, and EGR had three levels each, while engine load had four levels. The test matrix is shown in Table 3.9. 14 bar BMEP tests were also conducted, but only for stoichiometric operation with no EGR. The focus on low-speed operation was both to minimize the acceleration forces on the wireless telemetry system, as well as, to align with the future trend of downspeeding to improve fuel efficiency [62]. Notice that due to engine performance characteristics, some of the lean and dilute operating points could not be achieved. The experiment was broken up into two, essentially full factorial, tests where EGR and relative AFR were tested separately.

Table 3.9
Engine Map Test Matrix

Speed (RPM)	BMEP (bar)	Lambda [EGR %]
1500	2.0	1.00[0], 1.00[10], 1.00[20], 1.15[0], 1.30[0]
1500	5.0	1.00[0], 1.00[10], 1.00[20], 1.15[0], 1.30[0]
1500	8.0	1.00[0], 1.00[10], 1.00[20], 1.15[0], 1.30[0]
1500	11.0	1.00[0], 1.00[10], 1.00[20], 1.15[0], 1.30[0]
2250	2.0	1.00[0], 1.00[10], 1.00[20], 1.15[0], 1.30[0]
2250	5.0	1.00[0], 1.00[10], 1.00[20], 1.15[0], 1.30[0]
2250	8.0	1.00[0], 1.00[10], 1.00[20], 1.15[0], 1.30[0]
2250	11.0	1.00[0], 1.00[10], 1.00[20], 1.15[0], 1.30[0]
3000	2.0	1.00[0], 1.00[10], 1.00[20], 1.15[0], 1.30[0]
3000	5.0	1.00[0], 1.00[10], 1.00[20], 1.15[0], 1.30[0]
3000	8.0	1.00[0], 1.00[10], 1.00[20], 1.15[0], 1.30[0]
3000	11.0	1.00[0], 1.00[10], 1.00[20], 1.15[0], 1.30[0]

At each test condition, the spark timing was adjusted to achieve a nominal CA50 of 7°ATDC. In some high load cases; however, this was not possible since the spark timing was limited by combustion knock. In these cases, the spark timing was advanced up to the knock limited value. Additionally, the intake cam phasers were set for minimum valve overlap to minimize the amount of internal EGR. Once all the engine parameters were set, the engine was allowed to stabilize for 5-10 minutes and then data was collected. After each speed/load point, the engine was returned to the 1500 rpm and 2.6 bar BMEP control point. Data was collected at this condition and then the engine was shut down and the piston cleaning procedure described in section 3.3 was performed. After the cleaning, the

engine was returned to the control point and data was again collected in order to verify the effectiveness of the cleaning.

3.4.2 Identification of Fuel Spray Impingement on the Piston

The goal of this portion of work was to identify fuel impingement on the piston via surface temperature and heat flux measurements. In order to investigate impingement, a series of start of injection (SOI) sweeps were performed at different engine conditions. The test matrix is shown in Table 3.10. At 3000 RPM the -340° ATDC SOI timing was commanded in the ECU but it was found to be calibration limited to -320° ATDC and thus that timing was not run for the 3000 RPM cases. At each test condition the intake cam phasing and spark timing were automatically controlled by the factory PCM. The engine was operated under stoichiometric conditions with no EGR. Again, the cleaning procedure and control points were completed after each SOI sweep.

Table 3.10
Impingement Test Matrix

Speed	BMEP	SOI
<i>RPM</i>	<i>bar</i>	$^{\circ}$ ATDC
1500	2.6	-340, -320, -300, -280, -260
1500	5.0	-340, -320, -300, -280, -260
1500	8.0	-340, -320, -300, -280, -260
3000	2.6	-340, -320, -300, -280, -260
3000	5.0	-340, -320, -300, -280, -260
3000	8.0	-340, -320, -300, -280, -260

Chapter 4

Data Processing and Analysis¹

This section describes the data processing and analysis techniques used to extract meaningful information from the raw data collected by a variety of data acquisition devices.

4.1 Piston Thermocouple Telemetry Signal Processing

The piston thermocouple telemetry signal required a substantial amount of processing to resolve the raw data into complete cycle temperature traces for each thermocouple location. The raw data was multiplexed and thus the first step in the process was to demultiplex the signal. The multiplexed signal consisted of 15 thermocouple channels and 1 marker channel. The marker channel had a value near the maximum output of the transmitter, which correlated to a temperature of approximately 1000°C. This was significantly different than the 100-250°C range of the piston thermocouples and made the marker channel easy to identify. However, due to dropouts in the telemetry signal, the raw data required some filtering to allow the marker channel edges to be located. First, a threshold of 900°C was used to transform the original data into a digital signal with only a high or low value. After this, a median filter with a length of 175 points was used to eliminate dropout spikes. An example of the result of digitizing and filtering the data is shown in Fig. 4.1. Once the signal was filtered, the marker channel edges were used to determine the indices for each of the 16 channels. The data before the first and after the last marker channel was not used. Additionally, since the multiplexer timing was not perfect,

¹The material contained in this chapter is planned for submission as part of a journal article and/or conference paper in the future.

30-60 data points on either side of the transition between channels were skipped.

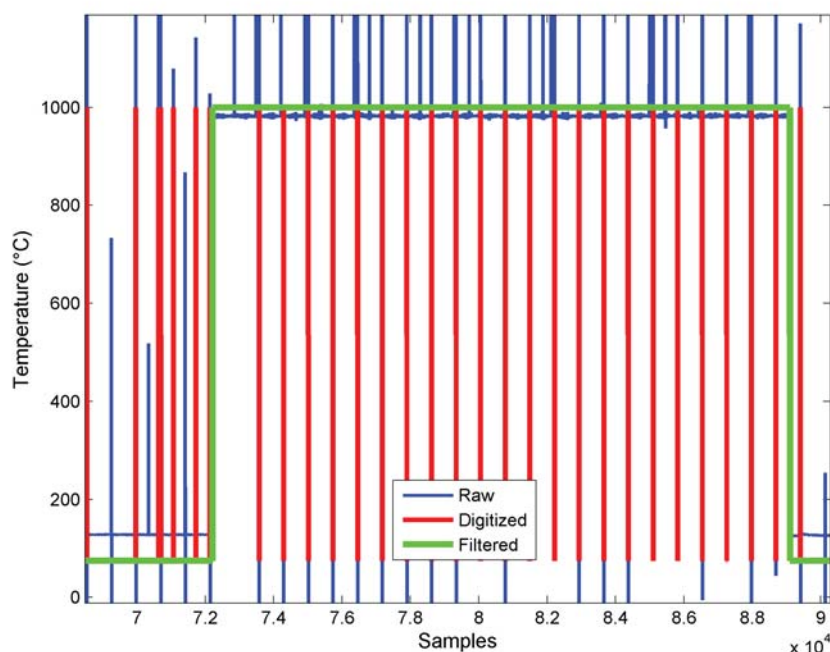


Figure 4.1: Example of Filtering Used on Telemetry Signal

Once the piston telemetry data was successfully demultiplexed, the raw temperature data for each channel had to be processed to get an accurate temperature profile for a full engine cycle. As a result of the dropouts and broadband noise, a somewhat lengthy filtering, averaging, and smoothing process was used. The first step was to eliminate obvious dropouts by eliminating any points outside of a 100-250°C temperature window. After that, a short 13 point median filter was used to eliminate some of the dropout spikes not removed by the first step. Next, the ensemble average of all the cycles for a given test point was computed. A final 15 point median filter was applied to the averaged data to further reduce the effects of dropouts. After that, a smoothing filter was applied using the "lowess" method with a span of 6%. The term "lowess" was derived from "locally weighted scatter plot smooth" and uses locally weighted linear regression to smooth the data [63]. The smoothing was done to fill in the gaps in the cycle that resulted from a consistent dropout region. This region was the result of none of the four antennas receiving a good signal during those engine positions. The region was consistent at the engine position range of -325° to -315° and 35° to 45°. This was believed to be caused by the positioning of the counterweights during those crankshaft positions. Finally, the smoothed data was fit to a

100 term Fourier series. An example of the raw data and the final result of this processing technique is shown in Fig. 4.2.

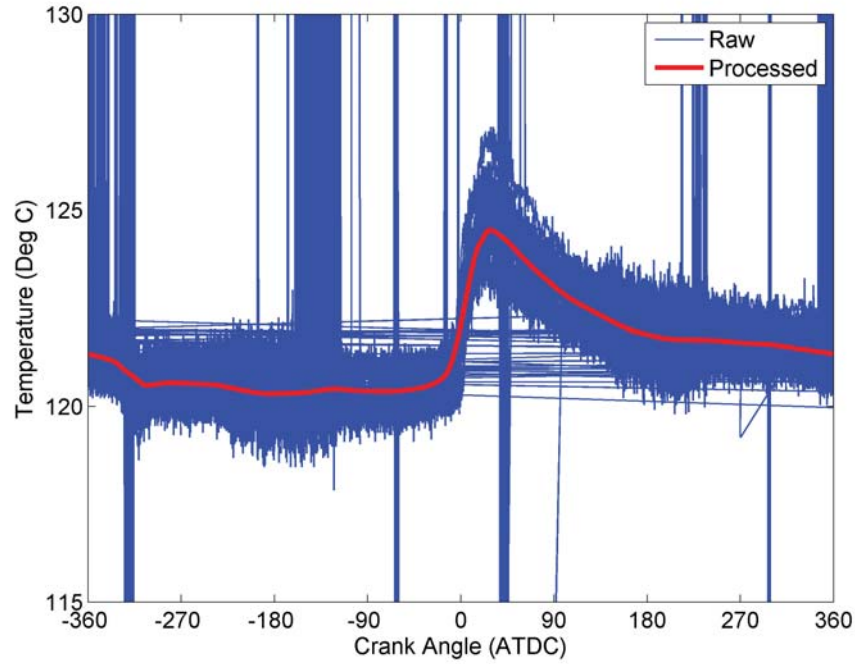


Figure 4.2: Piston Surface Thermocouple Data: Raw and Processed

4.2 Heat Flux Calculation

The in-cylinder temperatures were directly recorded by the data acquisition system; however, the heat flux for the combustion surface thermocouples had to be calculated in post processing. The most common technique from the literature for calculating the heat flux was to solve the one dimensional unsteady heat conduction equation along the probe [30,38,64].

This method represented the surface temperature as a truncated Fourier series of the form:

$$T_w(t) = \overline{T_w}(0) + \sum_{n=1}^N [A_n \cos n\omega t + B_n \sin n\omega t] \quad (4.1)$$

where $T_w(0)$ was the time-averaged surface temperature, A_n and B_n for $n = 1$ to N were the Fourier coefficients, t was time, and ω was one half the angular velocity of the engine.

The measured surface temperature time history, $T(0,t) = T_w(t)$, was used along with the boundary condition of the in-depth thermocouple at a distance δ below the surface, $T(\delta,t) = T(\delta)$. The in-depth temperature was assumed to be constant. Then using the semi-infinite idealization, it was possible to solve the one-dimensional unsteady heat conduction equation

$$\frac{\partial^2 T}{\partial x^2} = \frac{1}{\alpha} \frac{\partial T}{\partial t} \quad (4.2)$$

where $\alpha = \frac{k}{\rho c}$ was the thermal diffusivity. From this the instantaneous heat flux as a function of time, $q_w''(t)$, was found as

$$q_w''(t) = \frac{k}{\delta} (\bar{T}_w - T_\delta) + k \sum_{n=1}^N \sqrt{\frac{n\omega}{2\alpha}} [A_n (\cos n\omega t - \sin n\omega t) + B_n (\sin n\omega t + \cos n\omega t)] \quad (4.3)$$

where the first term was the steady-state heat flux and the second term was the transient heat flux. For surface thermocouples without an additional embedded junction, only the transient heat flux could be calculated. This analytical technique was implemented in Matlab and used to determine instantaneous surface heat flux.

The thermo-physical material properties used in the calculation of heat flux greatly effect the results. The piston and cylinder head were made from an aluminum alloy; however, the base metal of the type J thermocouples was iron. Assanis and Badillo [65] showed that it was best to use the properties of the probe instead of the properties of the piston in heat flux calculations. They showed that the error between the calculated and true heat flux values was only 7% when probe properties were used but could be as high as 62% when using the properties of the aluminum piston, instead of the probe. Therefore the thermo-physical properties used for the analysis were those of iron, which has a thermal conductivity of 40 W/m² and a thermal diffusivity of 2.3x10⁻⁵ m²/s.

4.3 Thermodynamic Analysis of the Engine System

4.3.1 1st Law Energy Analysis

A first law of thermodynamics based energy balance was used to analyze the energy flows into and out of the engine. The energy into the engine resulted from the flow of air and fuel;

while the energy out of the engine was divided among crankshaft work, heat transfer to the coolant, and exhaust gas flow. Additionally there were some unmeasured losses that were represented by a miscellaneous energy loss term. These losses included the work required for the oil, water, and high-pressure fuel pumps as well as the radiative and convective heat losses from the engine surfaces. A first law energy balance is shown in Eq.4.4.

$$\dot{m}_{air}h_{air} + \dot{m}_{fuel}Q_{LHV} = \dot{m}_{exh}h_{exh} + \dot{Q}_{cool} + \dot{W}_{shaft} + \dot{E}_{misc} \quad (4.4)$$

There were multiple control volumes that could have been used to analyze this system. The two control volumes studied in this work were adapted from those presented by Xin in 2009 [57]. The first control volume is shown in Fig. 4.3. In this case, the control volume boundary was set upstream of EGR introduction for the intake and downstream of EGR pick-up for the exhaust and thus the EGR loop and turbocharger were kept inside the control volume. The energy balance based on this control volume can be seen in Eq. 4.5.

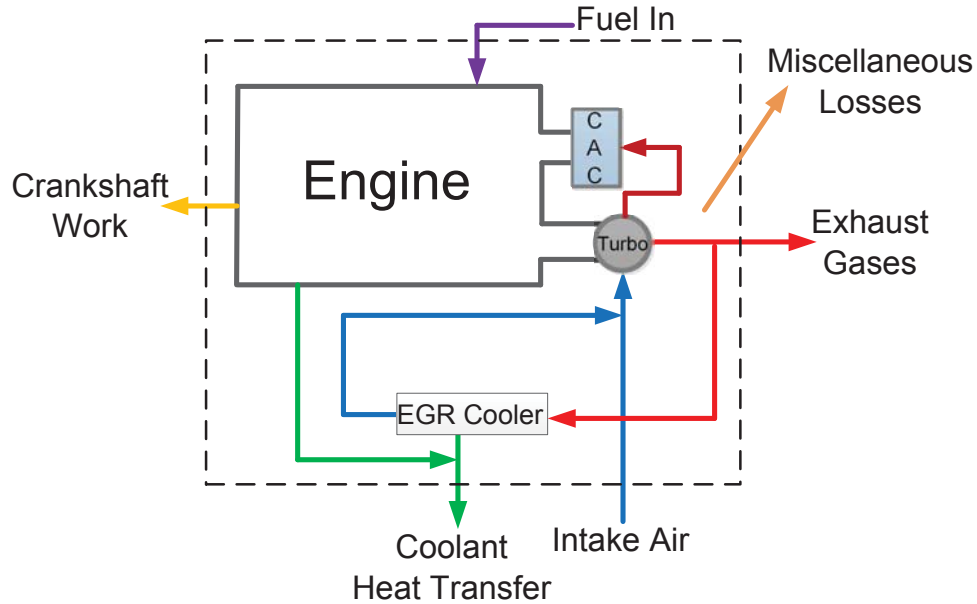


Figure 4.3: Control Volume for Engine Energy Balance 1

$$\dot{m}_{air}h_{pre_egr} + \dot{m}_{fuel}Q_{LHV} = \dot{m}_{exh}h_{post_egr} + \dot{Q}_{cool} + \dot{W}_{shaft} + \dot{E}_{misc} \quad (4.5)$$

In the other case, the control volume boundaries were set at the intake manifold (IM) and at the turbine inlet for the exhaust, as shown in Fig. 4.4. In this approach, EGR flows crossed the boundary and had to be accounted for. This resulted in a slightly more complicated analysis; however, it had the advantage of minimizing the amount of unmeasured heat losses from the exhaust system between the turbine and EGR pick-up. The energy balance equation for the second control volume is shown in Eq. 4.6.

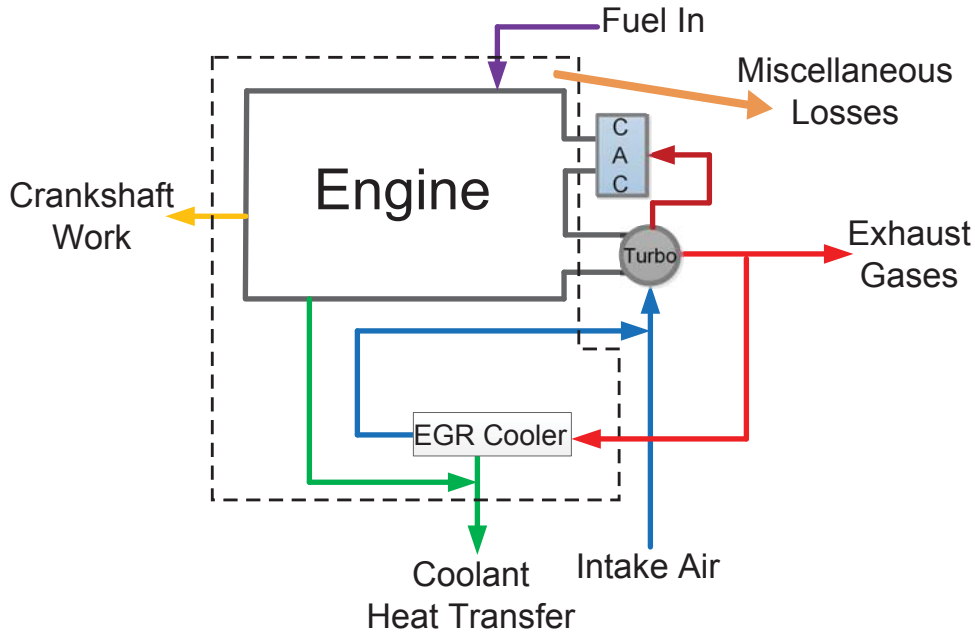
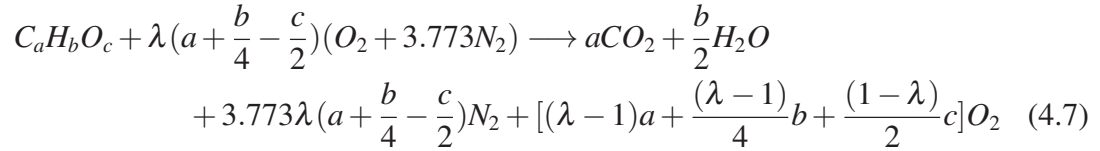


Figure 4.4: Control Volume for Engine Energy Balance 2

$$\dot{m}_{air}h_{IM_air} + \dot{m}_{egr}h_{IM_egr} + \dot{m}_{egr}h_{hot} + \dot{m}_{fuel}Q_{LHV} = \dot{m}_{exh+egr}h_{turb_in} + \dot{m}_{egr}h_{cooled} + \dot{Q}_{cool} + \dot{W}_{shaft} + \dot{E}_{misc} \quad (4.6)$$

Steady state temperature and pressure measurements were used to determine the properties of the intake air, exhaust gases, and coolant. The coriolis fuel flow meter were used to quantify the fuel flow rate into the engine. Due to a calibration error on the LFE, the air flow rate was calculated using the fuel flow and AFR measurements instead. The exhaust gas was modeled as a four component mixture of nitrogen (N_2), oxygen (O_2), carbon dioxide (CO_2), and water vapor (H_2O). The exhaust gas concentrations were computed based on the assumption of complete combustion. The chemical equation used to determine the exhaust

gas concentrations is shown in Eq. 4.7. The concentrations were then used to compute the mixture properties.



The assumptions of complete combustion and a simple four component exhaust gas mixture introduced a small amount of error into the energy balance analysis. However, not accounting for small concentrations of nitrogen oxides, carbon monoxide, and unburned hydrocarbons in the exhaust did not change the enthalpy very much. The specific enthalpies of nitrogen (N_2), nitrogen monoxide (NO), nitrogen dioxide (NO_2), carbon monoxide (CO), and carbon dioxide (CO_2) at 1000 K differ by less than 8%. Additionally, since NO_x and CO typically account for less than 1% of the exhaust mixture [64], the error caused by the assumption of a four component exhaust mixture was negligible.

The fuel energy delivered was calculated using the mass flow rate and the lower heating value of the fuel. The coolant energy was calculated from the mass flow rate, the specific heat, and the temperature difference across the engine. The intake and exhaust gas energies were computed using their mass flow rates and enthalpies. However, all enthalpies are actually differences in enthalpy between the current state and a reference state. Therefore a reference state for this analysis had to be chosen. The convention of using the standard reference state of 25°C and 1 bar was used for this research and thus the enthalpies of the intake air and the exhaust gases were computed as the difference in enthalpy between the experimental state and the reference state. Engineering Equation Solver (EES®) was used to determine the fluid properties and compute the results of the energy balance equations.

4.3.2 2nd Law Exergy Analysis

While the first law energy balance showed the quantity of energy in the various streams, it did not describe how much effective work could actually be extracted from the waste heat sources. A second law analysis; however, provides insight into the actual waste heat recovery potential. Since converting waste heat into effective work requires a

thermodynamic cycle, the amount of work recovered is limited by the Carnot cycle efficiency. This leads to the expression in Eq. 4.8 for the exergy, or waste heat recovery potential \dot{X}_Q , for a waste heat source \dot{Q} at temperature T with a dead state temperature of T_0 . The dead state temperature used for the analysis in this study was 25°C. It should be noted here that the waste heat recovery potential of the exhaust does not consider the potential for work from the exhaust pressure. This additional exergy would be important from the perspective of the turbocharger but not for a Rankine cycle or TEG waste heat recovery device.

$$\dot{X}_Q = \left(1 - \frac{T_0}{T}\right)\dot{Q} \quad (4.8)$$

With the dead state temperature fixed, the temperature of the waste heat source determines the maximum efficiency of the waste heat recovery process. This fact becomes important when comparing the coolant waste heat recovery potential with that of the exhaust system. Coolant temperatures are nominally 90-100°C, while exhaust gas temperatures for SI engines range between 350-950°C, depending on the operating conditions and location in the exhaust system. Therefore, the waste heat recovery potential of exhaust waste heat is typically much higher than that of coolant waste heat. However, with dilution from lean AFRs or EGR, the exhaust gas temperatures can be reduced dramatically. This decrease in temperature decreases the enthalpy and Carnot efficiency, but this decrease is potentially offset by the increase in mass flow rate. This trade-off was analyzed from both an energy and exergy perspective.

4.4 Impingement Identification

In order to identify impingement, a signature in the surface temperature data had to be identified. It had been shown in HCCI engines that impingement from early injection resulted in a sharp decrease in surface temperature as well as a spike in heat transfer out of the piston surface [23]. This is evident in Fig. 4.5 and Fig. 4.6 for locations P1 and P7.

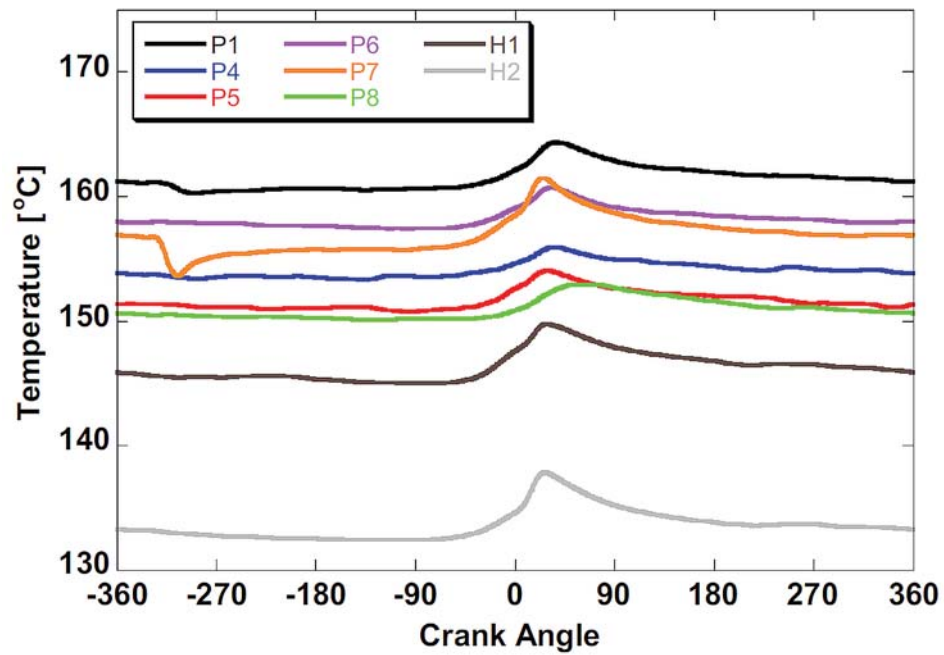


Figure 4.5: Plot of Piston Surface Temperatures for an HCCI Engine [23] *Reprinted with permission. Copyright ©2009 SAE International*

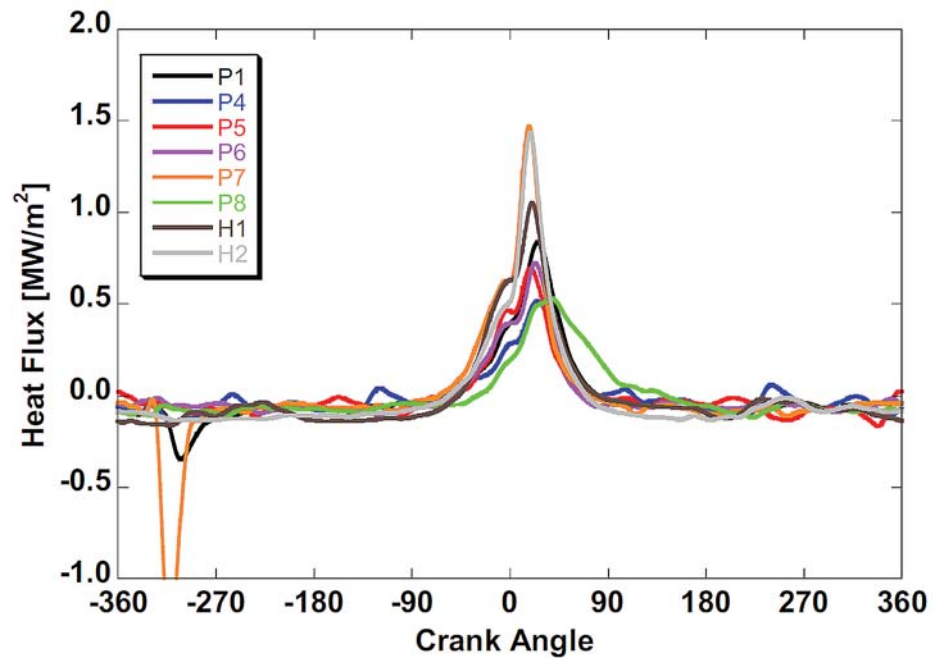


Figure 4.6: Plot of Piston Surface Heat Flux for an HCCI Engine [23] *Reprinted with permission. Copyright ©2009 SAE International*

From the heat flux data, the impingement event is obvious; however, only STC_2 and STC_3 (shown in Fig. 3.4) had an in-depth thermocouple that could be used for total heat flux calculations. The surface thermocouples at the other locations likely to see impingement, STC_1, STC_4, and STC_8, did not have an in-depth thermocouple; however, the transient portion of the heat flux was still calculated. The absolute magnitude of the heat flux was off by some DC offset, but the dynamics were correct. Therefore a method for identifying an impingement event from surface temperature measurements alone had to be developed. In order to identify the sharp change in temperature as a result of impingement, it was useful to look at the derivative of temperature with respect to crank angle $dT/d\theta$. Miers et al. [42] used this parameter to identify flame impingement on the surface of a diesel engine piston. In that case, a positive spike in $dT/d\theta$ prior to the main spike was identified as a flame impingement signature. For fuel spray impingement in this research, it was expected that a negative spike in $dT/d\theta$ or the transient surface heat flux would identify impingement.

Chapter 5

Results and Discussion¹

5.1 Energy Balance Results

Using the analytical techniques described in the preceding sections, the results of the engine energy balance were computed. The effects of speed and load on the energy distribution for control volume 1 and control volume 2 are shown in Fig. 5.1. These results confirmed those of other researchers who showed that the majority of the energy at light loads went to the coolant; while at higher loads more went out via the exhaust and as brake work [21, 57–59, 66, 67]. There was also a smaller trade-off between coolant and exhaust energy as a function of speed, with higher speeds resulting in less time for heat transfer to the coolant and thus higher exhaust energy percentages.

By comparing the two control volumes, it was possible to identify the effect of the location used for the exhaust temperature measurement. From control volume 2 to 1, the energy exiting via the exhaust was decreased by 13-27%, leaving instead as radiative and convective heat transfer from the exhaust pipes. This highlighted that the exhaust energy was highly dependent on the location in the exhaust system. From a waste heat recovery perspective, this meant that the best place for a WHR device was at the exhaust manifold (CV 2); however, if turbochargers and/or catalytic converters were being used, the device may need to be located further down the exhaust system (CV 1), to prevent negatively affecting the operation of the engine.

¹The material contained in this chapter is planned for submission as part of a journal article and/or conference paper in the future.

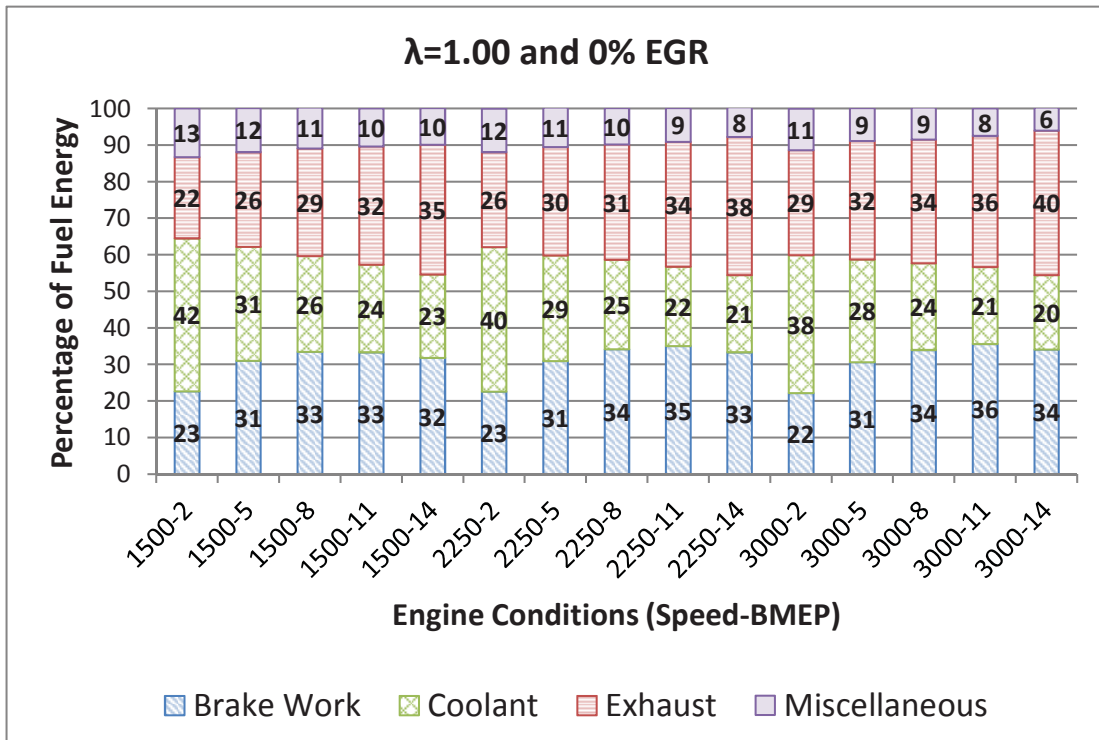
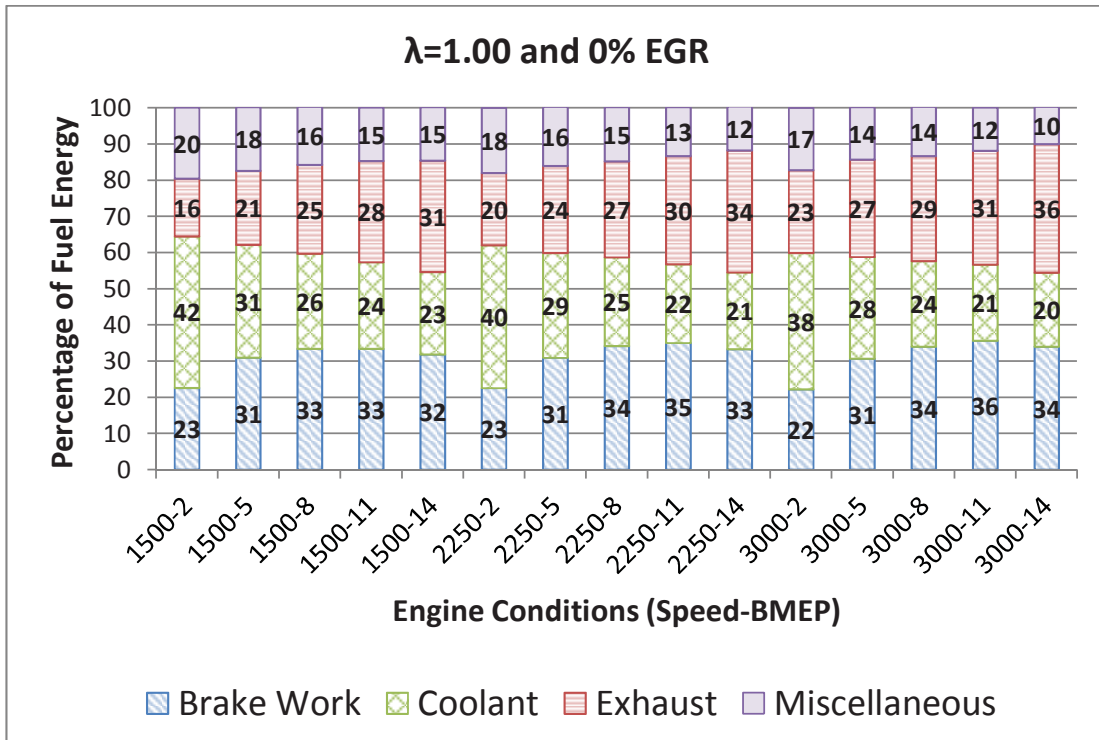


Figure 5.1: Engine Energy Balance for CV1 and CV2

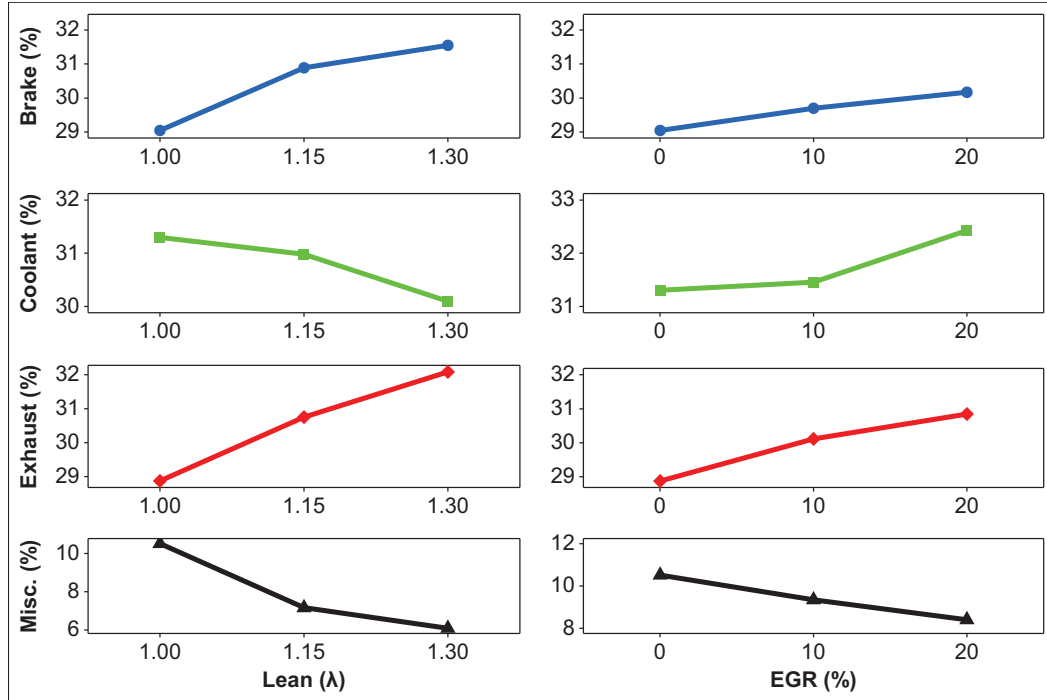


Figure 5.2: Main Effects of Dilute Combustion from Lean Operation and EGR on the Energy Distribution for Control Volume 2

The focus of this work, however, was not on the effects of speed and load, but rather on the effects of lean and dilute combustion on the energy distribution. Using a DOE factorial analysis of the collected data, the main effects of these two parameters were quantified and are illustrated in Fig. 5.2. Each data point on the chart is the average of all speed and load points at that particular value of λ or EGR (9 runs per data point). Only the 2, 5, and 8 bar BMEP data was included in the main effects since, at 11 bar, the higher levels of EGR and lean operation were not achievable at 1500 RPM and at 14 bar, no EGR or lean tests were performed. The interaction plots that show more detailed effects of speed, load, λ , and EGR are shown in Appendix A.1. These allowed the effects of dilute combustion from lean operation and EGR to be compared as functions of speed and load. However, it was found that the effects were not significantly different regardless of speed or load. Therefore only the main effects are discussed in this section.

The main effects showed that on average, increasing λ from 1.0-1.3 increased the brake efficiency by around 2.5 percentage points while increasing the EGR rate from 0-20% only increased it by about 1.5 percentage points. Comparing the cases of 1.15 λ to 20% EGR, it was still found that the lean case resulted in a larger increase in brake efficiency (1.8 vs.

1.5 percentage points). In order to investigate the differences between dilution from lean operation and EGR, a dilution ratio was defined. This ratio is defined in Eq. 5.1, where DR is the dilution ratio, $m_{diluent}$ is the mass of the diluent (EGR or excess air) and $m_{air_stoichiometric}$ is the mass of air needed for a stoichiometric AFR. This is essentially how the EGR rate is defined and thus the EGR rate is the same as the dilution ratio. For lean combustion, the dilution ratio for a λ of 1.15 is 13.0% and the dilution ratio for a λ of 1.30 is 23.1%.

$$DR = \frac{m_{diluent}}{m_{diluent} + m_{air_stoichiometric}} \times 100\% \quad (5.1)$$

With this equation, some key engine performance parameters affected by dilution were normalized by the dilution ratio. This allowed both dilution mechanisms to be more easily compared. The results are shown in Table 5.1. It was found that on average, dilution from lean operation resulted in a 0.40% increase in BTE per 1% of diluent, while for operation with EGR, the BTE only increased 0.22%.

Table 5.1
Analysis of Engine Performance Parameters with Dilution

Parameter		BTE	BTE	EGT	EGT	BD 10-90	BD 10-90
<i>Unit</i>		%Pts/DR	%/DR	°C/DR	%/DR	CA/DR	%/DR
Lean	1.15	0.133	0.44%	-3.16	-0.42%	0.196	0.72%
	1.30	0.100	0.34%	-3.43	-0.46%	0.270	0.98%
	Avg	0.116	0.39%	-3.29	-0.44%	0.233	0.85%
EGR	10%	0.071	0.23%	-3.39	-0.45%	0.349	1.26%
	20%	0.057	0.19%	-3.23	-0.43%	0.518	1.87%
	Avg	0.064	0.21%	-3.31	-0.44%	0.434	1.56%

To understand why dilution from lean AFRs resulted in better efficiency improvements, it was necessary to look into the effects of dilution on combustion temperatures and burn durations. It was found that dilution from EGR and lean operation resulted in very similar temperature decreases. It was expected that EGR would result in a slightly larger temperature decrease due to its higher specific heat capacity; however, the difference in the specific heat capacity of the air/EGR mixture was only about 1.5% for 20% EGR and about

0.7% for 10% EGR. This meant the difference in the temperature decrease per amount of diluent would have been very small and would be hard to differentiate when considering the accuracy limits of standard type K thermocouples and the EGR rate measurement system.

After analyzing the 10-90% burn durations for the experimental results of this work, a significant difference between EGR and lean operation was found. As highlighted in Table 5.1, the increase in burn duration for dilution via EGR was nearly twice that of lean operation. The longer the burn duration, the further the cycle was from the ideal scenario of constant volume combustion and the lower the efficiency. Lavoie et al. [68] studied the effect of burn duration on gross efficiency in simulation. Fig. 5.3 shows their results for this effect. They showed that increasing the burn duration from 30 to 40 degrees resulted in a the gross efficiency dropping by 1.1 percentage points. This effect explains part of the reason that lean operation resulted in a larger in increase in brake efficiency compared to dilution from EGR.

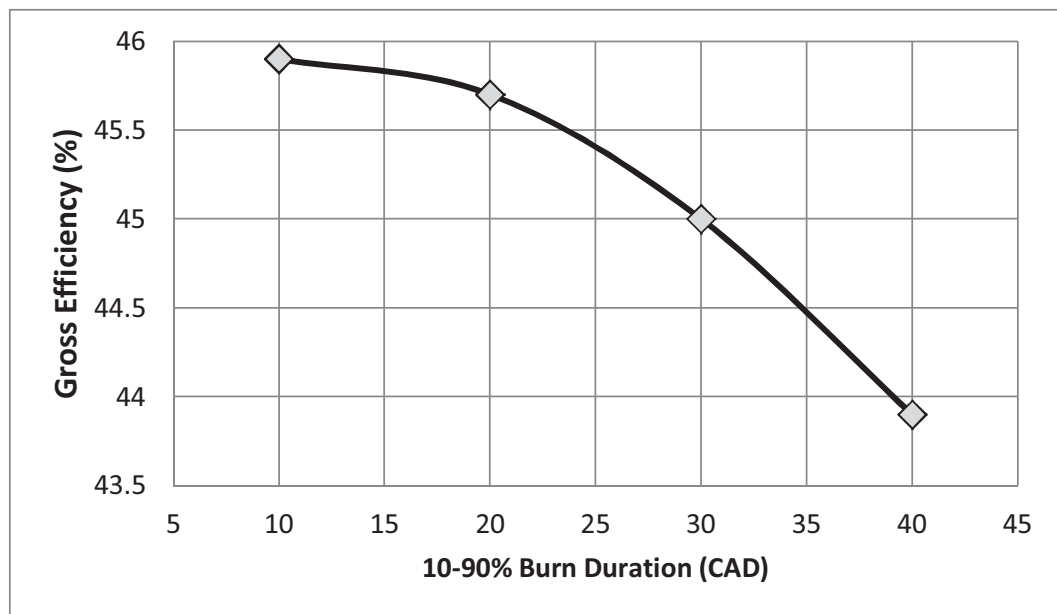


Figure 5.3: Simulation Results of the Effect of Burn Duration on Gross Efficiency. *This plot was created using data from [68].*

To understand why the burn durations were shorter for dilution from lean operation compared to EGR, the effect of dilution on laminar flame speed was investigated, since this parameter can be correlated to the burn duration [64]. A recent study by Syed et al. [69] in 2010 examined these effects. Their results are summarized in Table. 5.2. They showed the

laminar flame speed decreased almost twice as much for dilution with EGR compared to lean operation. This explains the differences in burn durations.

Table 5.2
Comparison of the Effects of Lean Operation and EGR on Laminar
Flame Speed. *Table created with data from [69].*

Dilution Ratio (%)	Δ Laminar Flame Speed (%)	
	<i>EGR</i>	<i>Lean</i>
10	-29%	-12%
20	-52%	-27%

However, Lavoie et al. [68] also showed that for the same burn duration, lean operation still resulted in a better thermal efficiency compared to the same amount of dilution from EGR. This result is shown in Fig. 5.4, where for the same dilution and same burn duration, lean operation still resulted in a 1-2% larger increase in gross efficiency. Caton [56] had similar results for his simulation and went on to show that there was an effect from differences in the specific heat ratios between lean and EGR based operation that led to a thermodynamic advantage for lean operation over EGR during the heat release portion of the cycle. The increased specific heat ratio caused the temperature and pressure during heat release to increase, resulting in a greater potential for expansion work. He found that when the thermal efficiency increase was plotted against the increase in gamma, that the results for both lean operation and EGR were similar. This is shown in Fig. 5.5. The combination of the differences in gamma and burn duration explain the larger increase in efficiency for lean operation over EGR.

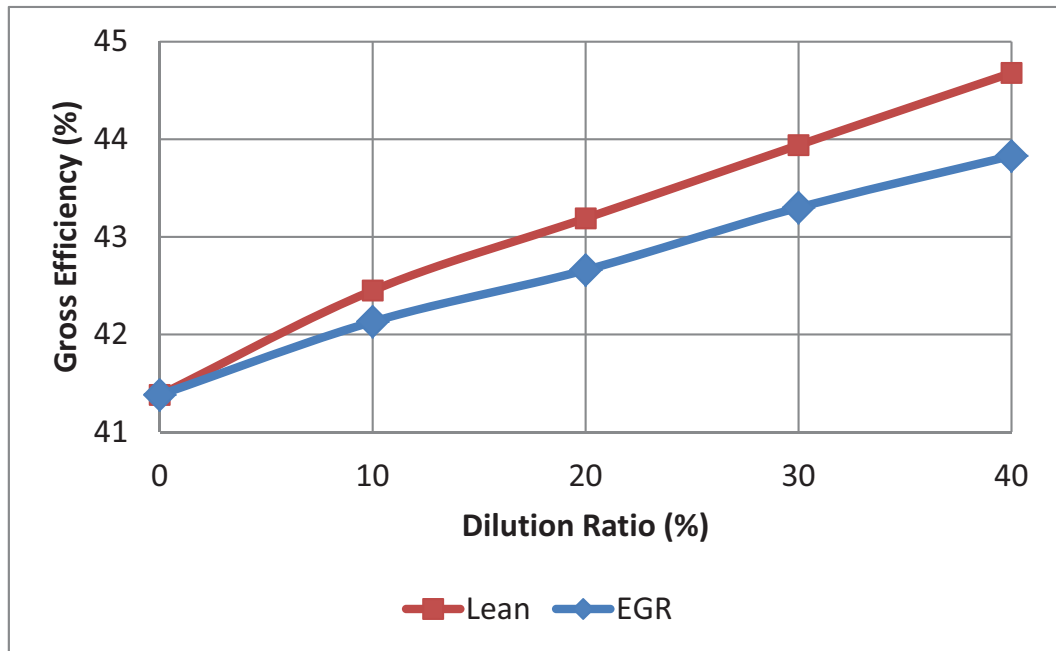


Figure 5.4: Simulation Results for the Effect of Dilution on Gross Efficiency. *This plot was created using data from [68].*

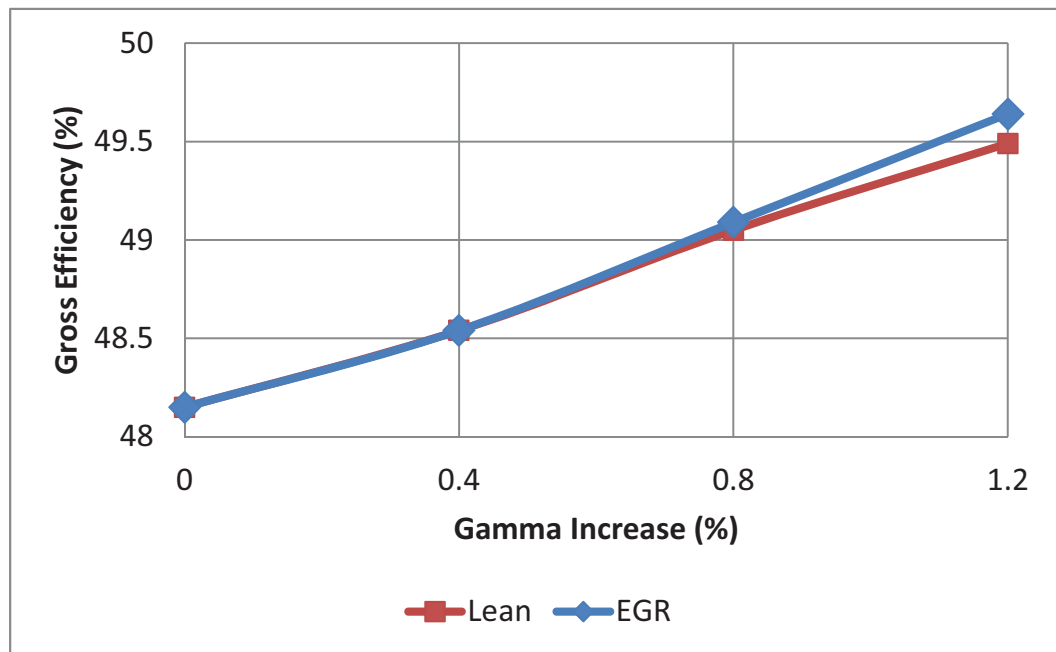


Figure 5.5: Simulation Results for the Effect of Gamma on Gross Efficiency. *This plot was created using data from [56].*

With an understanding of the effects of dilution on the brake efficiency, its effect on the energy in the coolant and exhaust streams were studied. The two methods differed significantly with respect to their effects on the coolant energy. The reduced in-cylinder temperatures of lean combustion resulted in a lower amount of coolant energy. However, despite the decreased temperatures and heat transfer to the coolant from the cylinder walls, the addition of heat transfer from the EGR coolers resulted in a net increase in the overall coolant energy when EGR was used.

The effects of the two parameters on the exhaust energy were of great interest since it was unclear whether the increased mass flow or decreased temperatures would be the dominant factor. Under the conditions studied in this work, the mass flow was found to be dominant and as a result, increasing λ or the EGR rate resulted in an increase in the exhaust energy percentage. It is important to note here that these results are for control volume 2, where the EGR was still present in the exhaust stream; however, when using control volume 1, the EGR loop remains inside the control volume and thus there was no increase in exhaust mass flow at that location. Using control volume 1, the lean cases still showed an increase in exhaust energy percentage, while the EGR cases showed a decrease. Excluding the EGR cases for CV 1, the energy balance analysis showed a general increase in the energy available in the exhaust; however, an exergy analysis had to be performed to determine if there was an actual increase in the waste heat recovery potential.

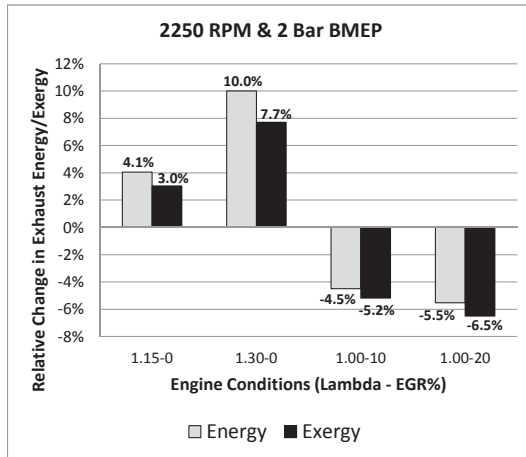
5.2 Exergy Analysis Results

In order to determine if the waste heat recovery potential in the exhaust stream was also increased, the exergy was compared to the baseline case ($\lambda = 1$ and $EGR = 0\%$). This analysis was performed for each operating point and the results for the 2250 RPM cases are shown in Figs. 5.6 and 5.7. These plots show both the relative change in energy as well as exergy. In general, it was seen that at light load, the mass flow increase was dominant and thus the energy and exergy both increased relative to the baseline for lean and EGR conditions. However, as the load was increased, the temperature effect became more dominant, especially for the exergy. This occurred since in the computation of exergy (Eq. 4.8), the temperature is counted twice. Enthalpy and thus the heat energy \dot{Q} is nearly linearly related with temperature and the Carnot efficiency is also directly related to temperature. As a result, when the temperature decreased, both the heat energy and the Carnot efficiency decreased, combining for a larger decrease in the exergy than

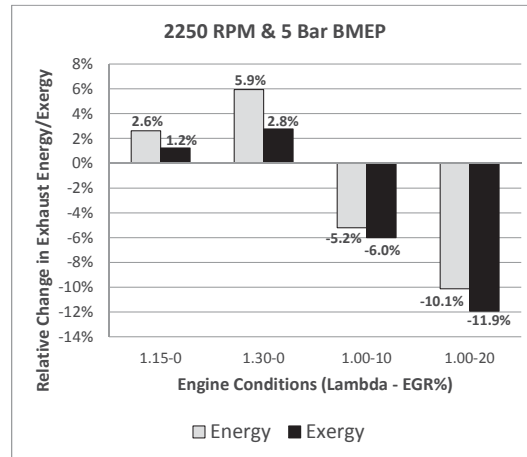
in the energy. This manifested itself in decreased waste heat recovery potential for the lean and EGR cases at higher loads, despite the increased waste heat energy. This trend was consistent for both the 1500 RPM and 3000 RPM cases for CV 2, which can be seen in Appendix A.2. This means that the exhaust waste heat recovery potential at the exhaust manifold would be decreased at medium to high loads if lean and dilute combustion strategies were employed. This has potential turbocharger sizing and design implications since it is actually a WHR device itself. In order to provide the intake pressures required by lean and dilute combustion strategies, the turbocharger must be optimized for these lower temperature, higher flow rate exhaust conditions. In extreme cases, a supercharger may even be required to meet the boosting requirements.

The more probable location for Rankine cycle WHR devices is likely to be after the turbocharger and catalytic converter and is better represented by control volume 1, thus it was important to also consider the results at this location in the exhaust. An interesting discovery was made when comparing these results to those of CV 2, the waste heat recovery potential in the exhaust for CV 1 was increased even at high loads for lean operation. While the increase was only about 1% at 8 bar, it was better than the 1% decrease seen at the exhaust manifold in CV 2. At 5 bar the difference between the two locations was even greater, with CV 1 resulting in a 3% increase at $\lambda = 1.3$ compared to a 2% decrease with CV 2. This trend held true for nearly all of the other operating conditions as well. The results for these conditions are shown in Appendix A.2. This meant that despite the decreased combustion temperatures that resulted from lean combustion, there was still a larger WHR potential in the exhaust for most operating conditions. Since the EGR had already been extracted from the exhaust for CV 1, there was always a decrease in the WHR potential for the EGR cases. However, it would be possible to use a WHR device in place of the standard liquid-air EGR cooler to recover some more of the exhaust waste heat energy.

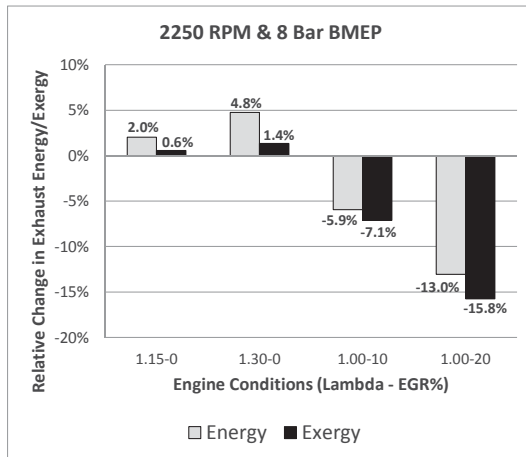
In order to understand why the trends for exhaust WHR potential differed depending on the location in the exhaust, it was necessary to look into the exhaust gas temperatures at these two locations. A comparison of the exhaust gas temperatures for the 2250 RPM 2-8 bar cases is shown in Fig. 5.8. At 5 bar, Fig. 5.8(c), it is shown that for CV 1 the temperature dropped by 23°C and 50°C as λ was increased to 1.15 and 1.30. However, for CV 2 the decrease was much larger, 43°C and 81°C respectively. Even on a relative basis, CV 1 exhaust gas temperatures decreased less than those for CV 2, as shown in Fig. 5.8(d). This was explained by examining the heat losses from the exhaust system



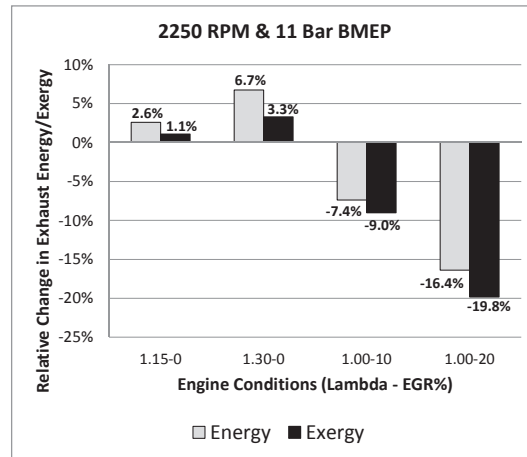
(a) 2250 RPM and 2 bar



(b) 2250 RPM and 5 bar



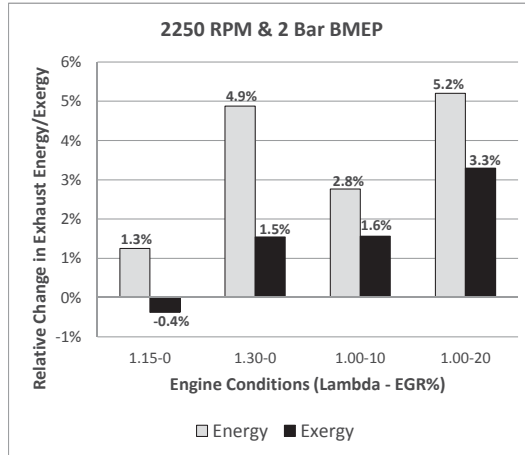
(c) 2250 RPM and 8 bar



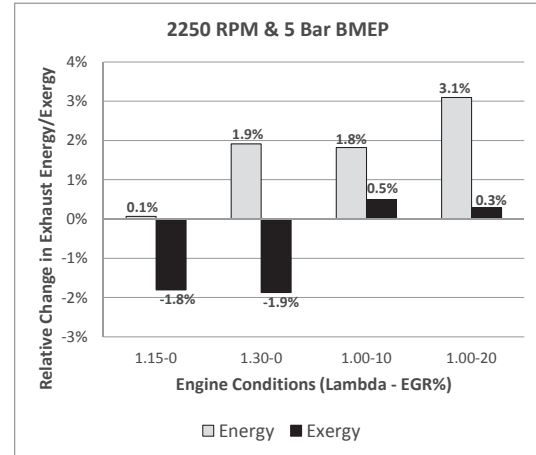
(d) 2250 RPM and 11 bar

Figure 5.6: Comparison of Exhaust Energy and Exergy for CV 1 at 2250 RPM

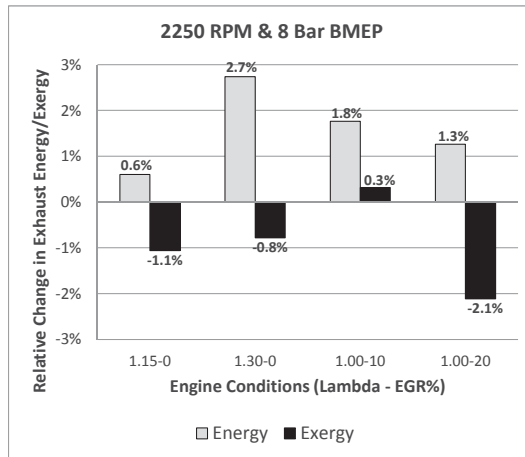
components. The exhaust gases leave the cylinder and go into the manifold at a certain temperature. From there the exhaust gases travel through the turbine and along a section of pipe before reaching the measurement location for CV 1. While the gases travel through the turbocharger and the pipes, they transfer heat to the walls and the walls transfer that heat to the environment via radiation and convection. Both of these heat transfer mechanisms scale with the temperature difference between the exhaust and the environment. Therefore, when the exhaust gas temperature was lowered, the radiative and convective heat transfer from the exhaust system was also decreased. This meant that the lower the temperature at the exhaust manifold, the less heat was removed from the exhaust gases as they traveled through the exhaust system, and the closer the starting and ending point temperatures were.



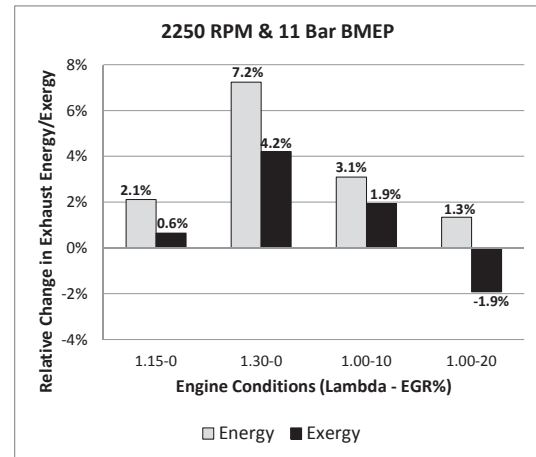
(a) 2250 RPM and 2 bar



(b) 2250 RPM and 5 bar



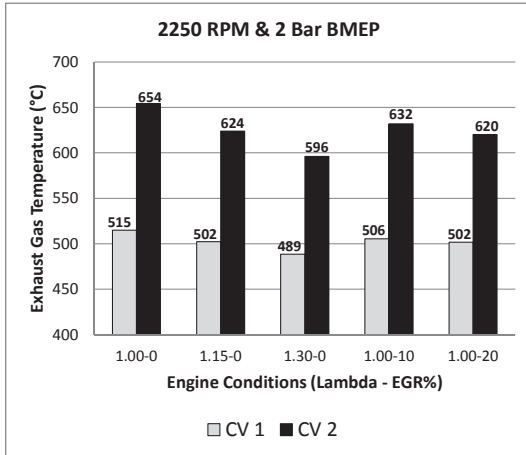
(c) 2250 RPM and 8 bar



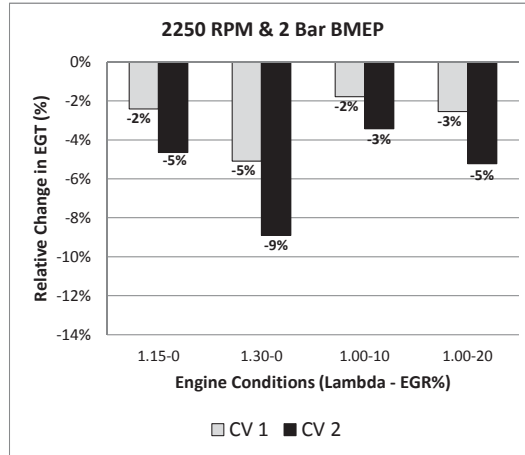
(d) 2250 RPM and 11 bar

Figure 5.7: Comparison of Exhaust Energy and Exergy for CV 2 at 2250 RPM

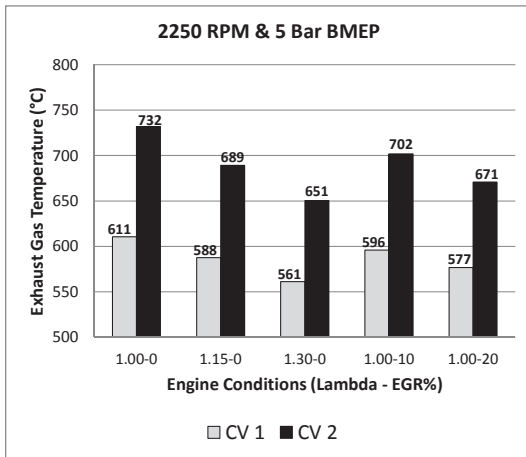
This was confirmed by the results in Fig. 5.8(c), which showed the difference between the EGTs at CV 1 and CV 2 decreased from 121°C to 101°C to 90°C as λ was increased. Since less heat was transferred to the environment, more was available in the exhaust.



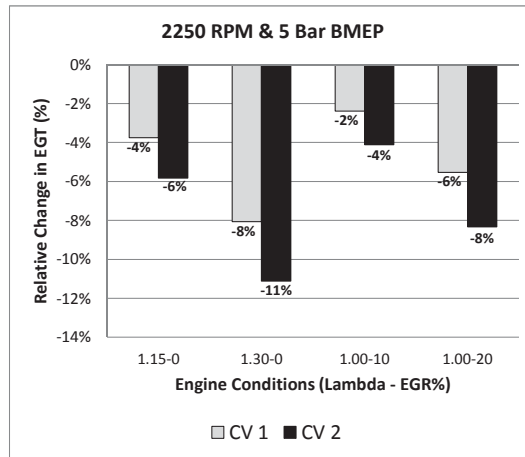
(a)



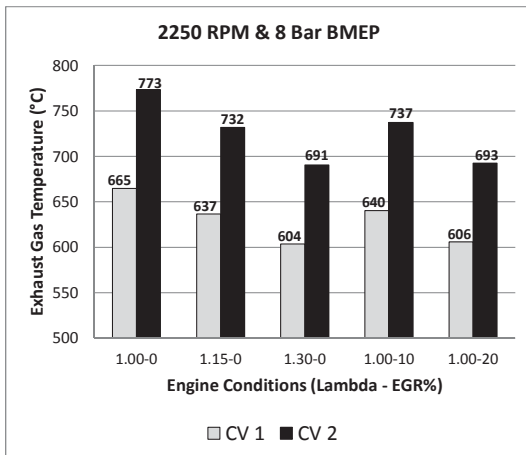
(b)



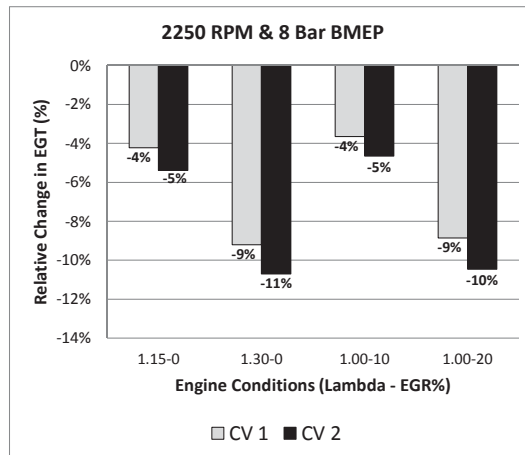
(c)



(d)



(e)

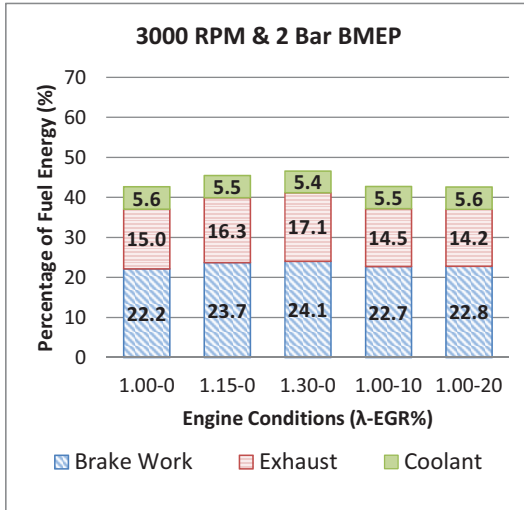


(f)

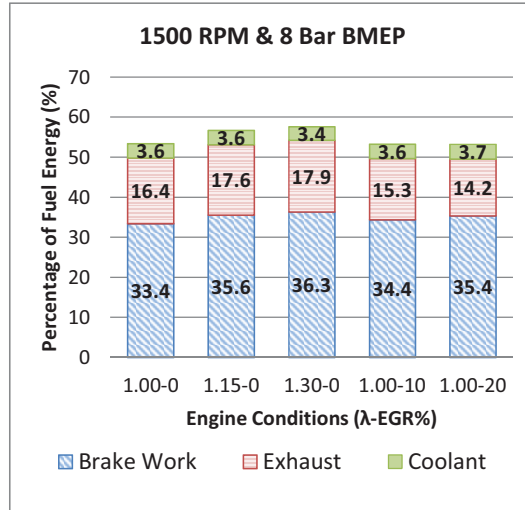
Figure 5.8: Comparison of Exhaust Gas Temperatures on an Absolute [(a),(c),(e)] and Relative [(b),(d),(f)] basis

5.3 Energy and Exergy Results Summary

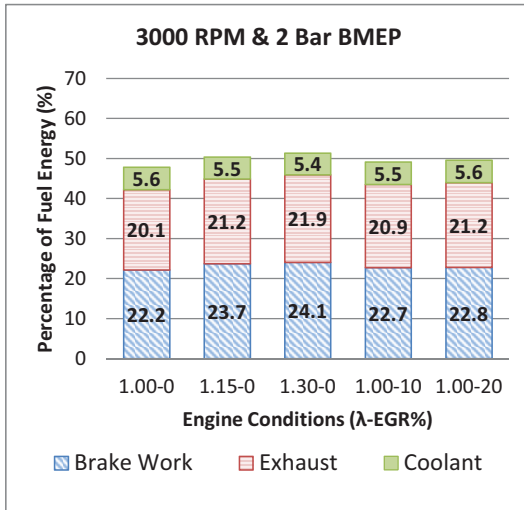
With an understanding of the effect of lean and dilute combustion on the energy and exergy balances of a GTDI engine, it was possible to analyze the potential for fuel economy improvements in future vehicles. The goal of downsizing and downspeeding engines is to allow the engine to operate at higher efficiency points during normal operation. For example, by downsizing to a smaller turbocharged engine and using an 8 or 9 speed gearbox, a vehicle's highway cruise point could be shifted from 3000 RPM and 2 bar BMEP to 1500 RPM and 8 bar BMEP. The results of such a shift on the exergy distribution is shown for both CV 1 and CV 2 in Fig. 5.9. Without waste heat recovery or lean/dilute combustion, the brake efficiency of the engine is improved from 22% to 33%, a 50% increase. Operating lean, the engine could be improved again and reach 36.3% brake thermal efficiency. These are great first steps; however, to meet the 2025 CAFE standard, additional improvements would be needed. Waste heat recovery from the exhaust has the possibility of improving the thermal efficiency an additional 18-22%, up to a maximum total thermal efficiency of 54-58%. Engineers will need to work on designing and optimizing engines, aftertreatment systems, and waste heat recovery devices to work together to get close to this maximum efficiency.



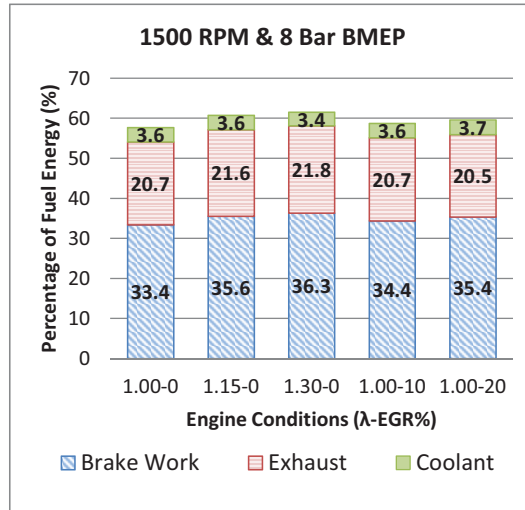
(a) CV 1 Initial Operating Point



(b) CV 1 Downsized/Downspeeded Point



(c) CV 2 Initial Operating Point



(d) CV 2 Downsized/Downspeeded Point

Figure 5.9: Comparison of the Exergy Distributions for a Downsized and Downspeeded Engine

5.4 Empirical Model of Engine Energy Balance

One of the objectives of this work was to create an empirical model that could be used to estimate the energy balance of the engine based on speed and load inputs. This was accomplished with a polynomial fit of the results of the energy balance to the speed and load inputs. A method of least squares regression was used for the fitting. The engine speed was normalized to mean piston speed (MPS) and the engine load was normalized to BMEP.

The 3 speeds and 4 loads (5 for BTE since it is known to be 0% at 0 bar BMEP) served to create a coarse map of the engine's operating conditions. This allowed surface plots to be created for each of the energy balance parameters. These can be seen in the plots in Fig. 5.10. The dots are the actual data points and the surface is the result of the polynomial fit. It must be noted here that this fit is for the data collected during the dilution study and as a result was taken with intake cams phased for minimum internal EGR. This results in slightly lower brake efficiencies than for the OEM calibration strategy, which would have used the internal EGR to improve the pumping losses at light load.

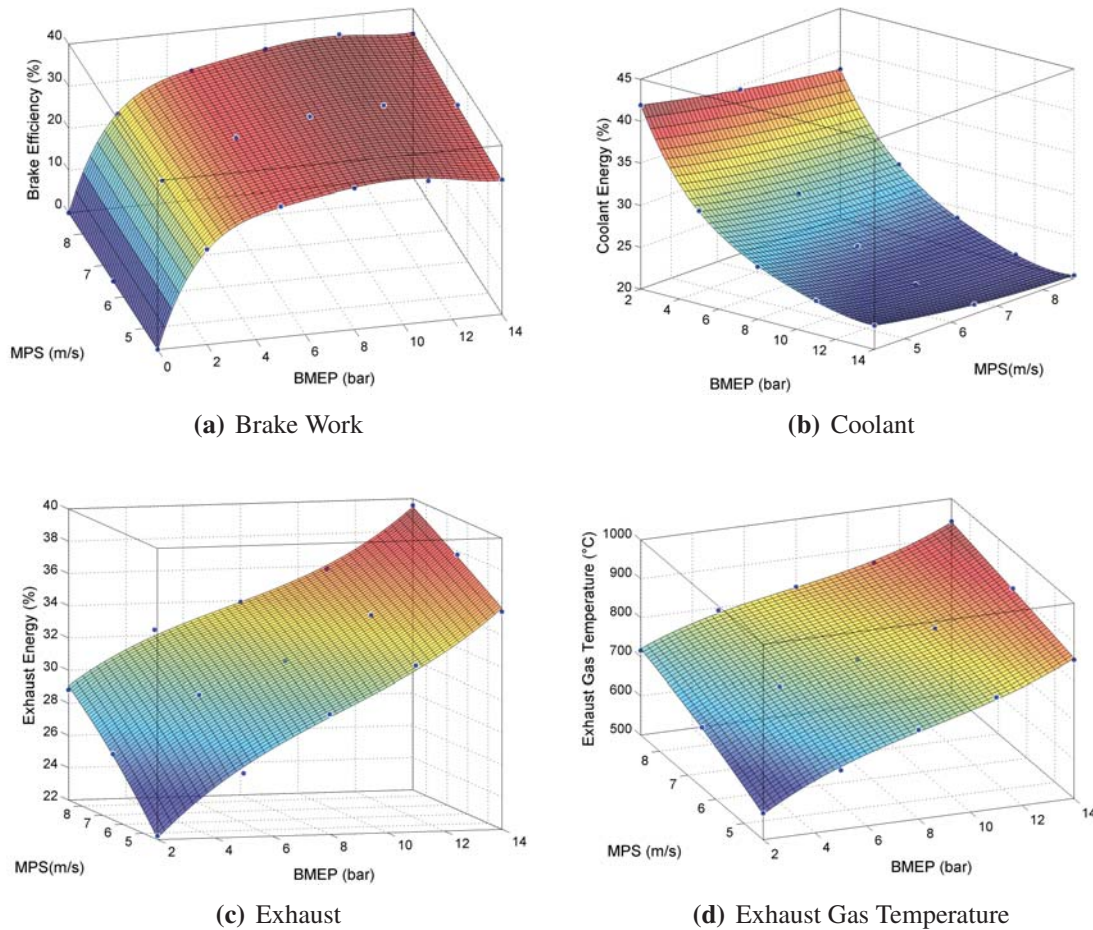


Figure 5.10: Energy Balance Model Fits for CV2

The fit for the brake efficiency used a 5th order polynomial for the engine load and a 1st order polynomial for the mean piston speed. After analyzing the fit coefficients, it was clear that some of the parameters in the original equation could be eliminated. Over the

relatively narrow range, there was little effect of the speed on BTE, thus most of the mean piston speed paramaters could be eliminated. The refined equation is shown in Eq. 5.2, where BTE is the brake thermal efficiency in %, x is the BMEP in bar, y is the mean piston speed in m/s and the coefficients (c_n) are defined in Table 5.3. The refined fit resulted in a root mean square error (RSME) of 0.33%.

$$BTE = c_0x + c_1x^2 + c_2x^3 + c_3x^4 + c_4x^3y + c_5x^5 \quad (5.2)$$

Table 5.3
Coefficients for Brake Thermal Efficiency Fit

Coefficient	Value	Coefficient	Value	Coefficient	Value
c_0	18.170	c_2	0.5773	c_4	0.0002273
c_1	-4.496	c_3	-0.0362	c_5	-0.0008601

The fit for the percentage of fuel energy in the coolant used a 4th order polynomial for the engine load and a 2nd order polynomial for the mean piston speed. This fit resulted in a RMSE of 0.17%. The equation is defined in Eq. 5.3, where $Q_{coolant}$ is the fraction of fuel energy in the coolant in %, x is the BMEP in bar, y is the mean piston speed in m/s and the coefficients (c_n) are defined in Table 5.4.

$$Q_{coolant} = c_0 + c_1x + c_2y + c_3x^2 + c_4xy + c_5y^2 + c_6x^3 + c_7x^2y + c_8xy^2 + c_9x^4 + c_{10}x^3y + c_{11}x^2y^2 \quad (5.3)$$

A simpler fit for the percentage of fuel energy in the exhaust was able to be used. It used a 3rd order polynomial for the engine load and a 2nd order polynomial for the mean piston speed. This fit resulted in a RMSE of 0.36%. The equation is defined in Eq. 5.4, where $Q_{exhaust}$ is the fraction of fuel energy in the exhaust in %, x is the BMEP in bar, y is the

Table 5.4
Coefficients for the Coolant Energy Fraction Fit

Coefficient	Value	Coefficient	Value	Coefficient	Value
c_0	62.840	c_4	-0.10790	c_8	0.029380
c_1	-9.210	c_5	0.01611	c_9	0.001175
c_2	-1.606	c_6	-0.07566	c_{10}	0.001153
c_3	1.204	c_7	-0.01031	c_{11}	-0.001630

mean piston speed in m/s and the coefficients (c_n) are defined in Table 5.5.

$$Q_{exhaust} = c_0 + c_1x + c_2y + c_3x^2 + c_4xy + c_5y^2 + c_6x^3 + c_7x^2y + c_8xy^2 \quad (5.4)$$

Table 5.5
Coefficients for the Exhaust Energy Fraction Fit

Coefficient	Value	Coefficient	Value	Coefficient	Value
c_0	6.092	c_3	-0.2032	c_6	0.007171
c_1	3.250	c_4	-0.2203	c_7	0.004760
c_2	3.167	c_5	-0.1006	c_8	0.006457

Similarly, the fit for the exhaust manifold temperature used a 3rd order polynomial for the engine load and a 2nd order polynomial for the mean piston speed. This fit resulted in a RMSE of 7.6°C. The equation is defined in Eq. 5.5, where EGT is the exhaust gas temperature at the manifold in °C, x is the BMEP in bar, y is the mean piston speed in m/s and the coefficients (c_n) are defined in Table 5.6.

$$EGT = c_0 + c_1x + c_2y + c_3x^2 + c_4xy + c_5y^2 + c_6x^3 + c_7x^2y + c_8xy^2 \quad (5.5)$$

While this model is very simple and has limitations compared to engine simulation packages like GT-Power, AVL Boost, or Ricardo WAVE, it provides a useful tool for the many applications that don't require all the capabilities of a 1-D engine simulation.

Table 5.6
Coefficients for the Exhaust Gas Temperature Fit

Coefficient	Value	Coefficient	Value	Coefficient	Value
c_0	198.20	c_3	-4.863	c_6	0.1692
c_1	75.64	c_4	-5.152	c_7	0.1089
c_2	72.72	c_5	-2.384	c_8	0.1522

One potential use is to estimate the potential improvements in fuel economy from downsizing/downspeeding, hybridization, and/or waste heat recovery. By understanding the power required for a vehicle to complete a given drive cycle, the mean piston speed and engine load can be determined for various levels of downsizing, as well as different transmission and hybridization strategies. Then the brake efficiency, and thus fuel flow rate, could be found for each point along the cycle. Integrating the fuel flow rate and distance traveled over the drive cycle would result in an estimate of the vehicle's fuel economy. Additionally, using the exhaust energy fraction and the exhaust gas temperature, the waste heat recovery potential in the exhaust could be analyzed as well. This would allow those without access to expensive simulation software to get an initial estimate of what the fuel economy improvements would be for applying new technologies and strategies to a modern GTDI engine.

A second use is for estimating the cooling system requirements for different engines or set of operating conditions. This model would allow the amount of heat energy entering the cooling system to be computed. With that quantity known, various water pumps, radiators, and coolant mixtures could be analyzed for performance. While the typical "rule of thirds" is a reasonable estimate for the energy distribution, this simple model provides a much better estimate that is applicable over a wide range of engine conditions without much additional work.

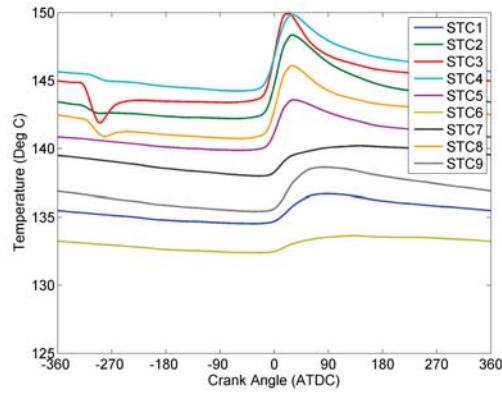
5.5 Combustion Chamber Temperature and Heat Flux Results

One of the objectives of this research was to understand the effects of speed, load, and dilution on the temperatures and heat fluxes of combustion chamber components including the piston and cylinder head. The specialized thermocouples allowed crank angle

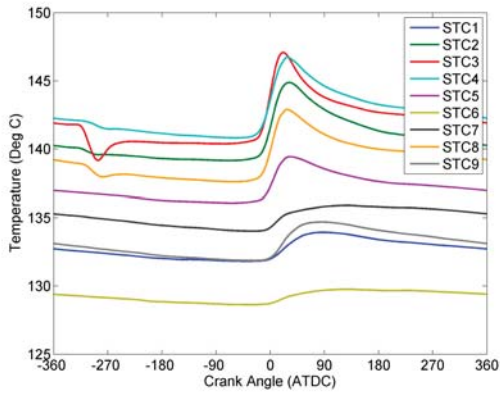
resolved surface temperature and heat flux profiles to be captured. Additional embedded thermocouples allowed temperatures within the components to be measured and analyzed as well.

After following the processing steps outlined in section 4.1, plots of the surface temperature profiles for the piston were created. The plots for dilution sweeps at each speed/load point were grouped together and the results for the 1500 RPM 2 and 8 bar BMEP cases are shown in Figs. 5.11 and 5.12. All of the cases are shown in Appendix C.

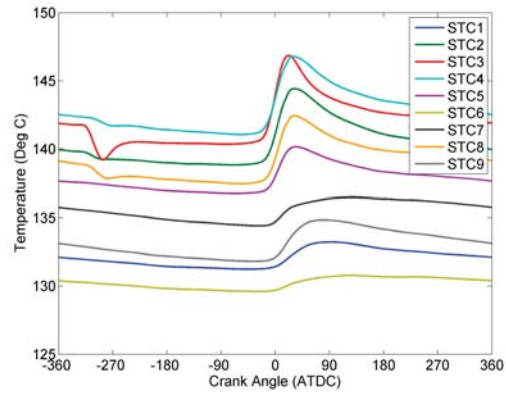
After analyzing the plots it became clear that the average surface temperatures were decreased when dilution was added. However, the shape of the temperature profile was not significantly affected. In order to compare the temperature profiles, the surface temperatures were normalized by subtracting the mean temperature from each point on the trace. These traces were then compared for STC_3 on the piston and HF_STC on the cylinder head. These two surface thermocouples were chosen since they had the best and most consistent response characteristics. The results of this analysis are shown in Fig. 5.13. In these figures, a small difference in the minimum and maximum heat flux between the stoichiometric case and the dilute cases was observed and the difference was more pronounced for the 2 bar case. Dilute cases resulted in about a 1°C lower temperature difference between the maximum and minimum values.



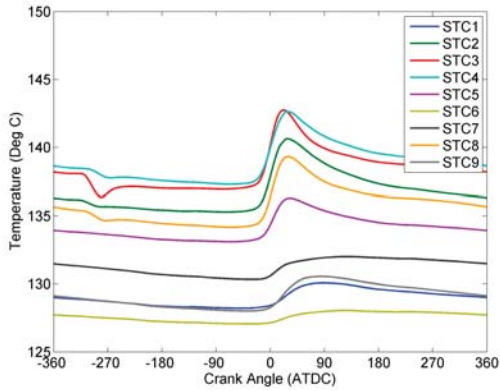
(a) $\lambda = 1.00$ and $EGR = 0\%$



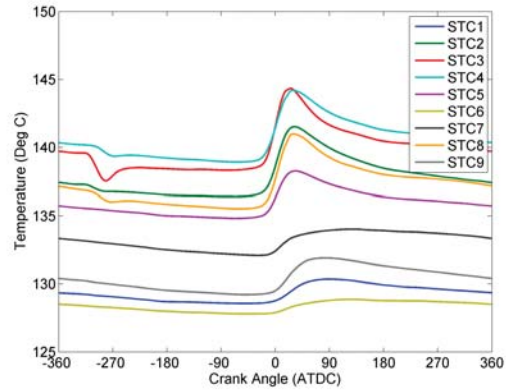
(b) $\lambda = 1.15$ and $EGR = 0\%$



(c) $\lambda = 1.00$ and $EGR = 10\%$

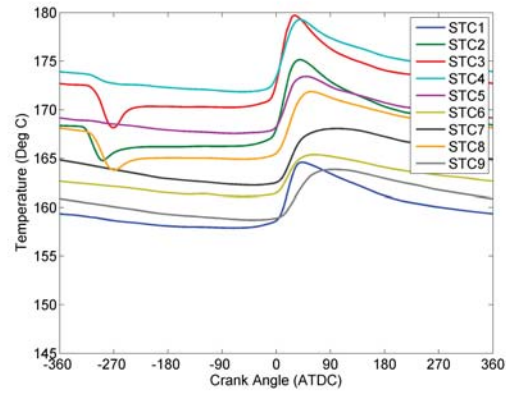


(d) $\lambda = 1.30$ and $EGR = 0\%$

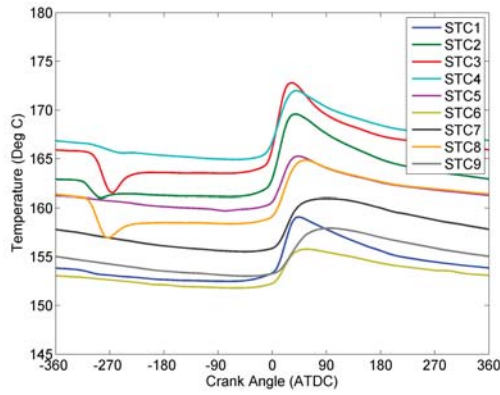


(e) $\lambda = 1.00$ and $EGR = 20\%$

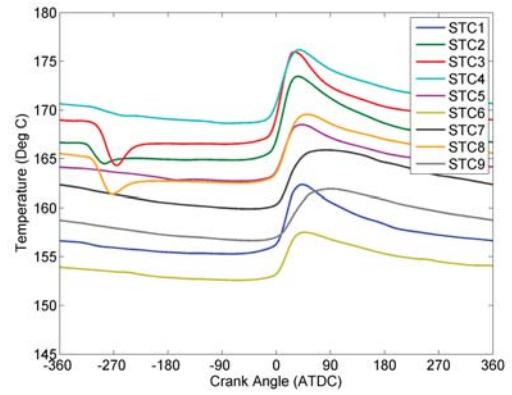
Figure 5.11: Piston Temperature Plot for 1500 RPM and 2 bar BMEP



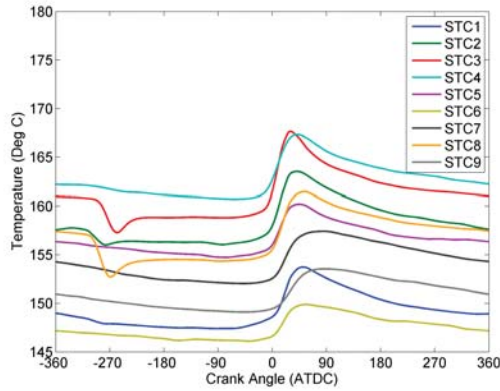
(a) $\lambda = 1.00$ and $EGR = 0\%$



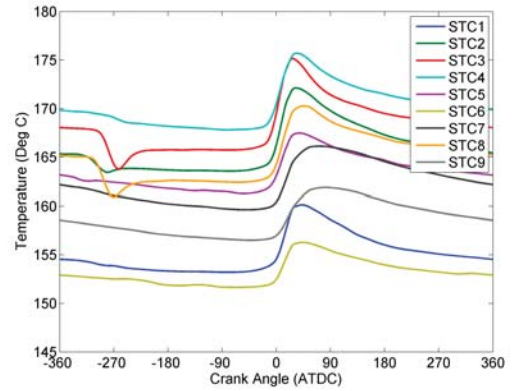
(b) $\lambda = 1.15$ and $EGR = 0\%$



(c) $\lambda = 1.00$ and $EGR = 10\%$

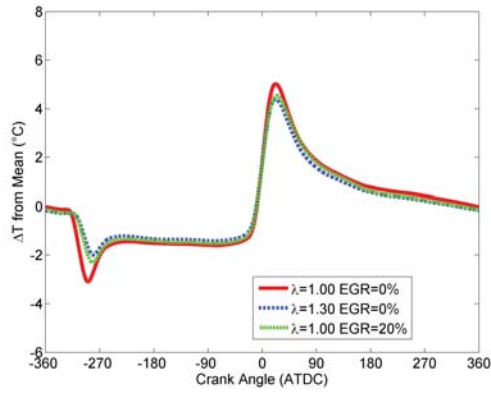


(d) $\lambda = 1.30$ and $EGR = 0\%$

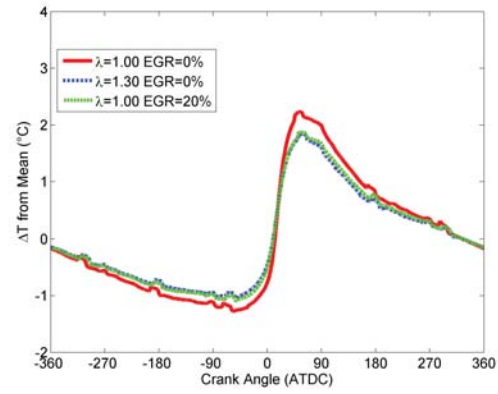


(e) $\lambda = 1.00$ and $EGR = 20\%$

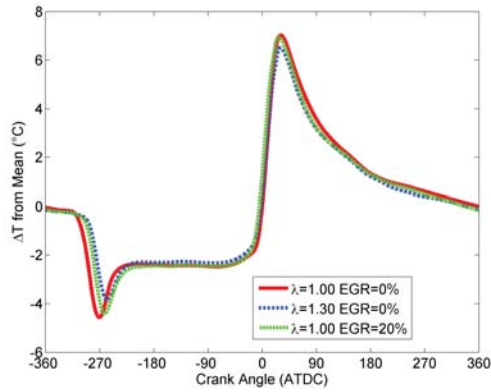
Figure 5.12: Piston Temperature Plot for 1500 RPM and 8 bar BMEP



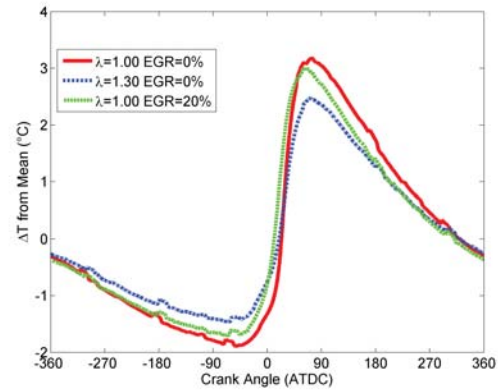
(a) 1500 RPM and 2 bar BMEP STC_3



(b) 1500 RPM and 2 bar BMEP HF_STC



(c) 1500 RPM and 8 bar BMEP STC_3



(d) 1500 RPM and 8 bar BMEP HF_STC

Figure 5.13: Comparison of Normalized Surface Temperature Profiles

It was also possible to analyze the surface heat flux for the piston and cylinder head thermocouples; however, only the thermocouples which had an additional embedded junction could be used to compute the total heat flux. The heat flux sensor in the cylinder head proved to be more stable than the piston thermocouples, with respect to carbon deposits affecting its response, so it was used for analyzing the effects of dilute combustion. The heat flux profiles for the 1500 RPM 2 and 8 bar BMEP cases are shown in Fig. 5.14. In these figures there was about a 20% reduction in the peak heat flux. The total heat transfer, which was computed by integrating the heat flux profile over the cycle, was also reduced for dilute operation. There were differences in the phasing of the heat flux profile at the 1500 RPM 8 bar BMEP case, but not at the 2 bar BMEP case. This was caused by differences in combustion phasing since at light load, the spark timing was controlled to achieve a CA50 of 7°ATDC; however, at 8 bar, the spark timing was limited by combustion knock and the

lean and EGR cases had different knock limited spark timings.

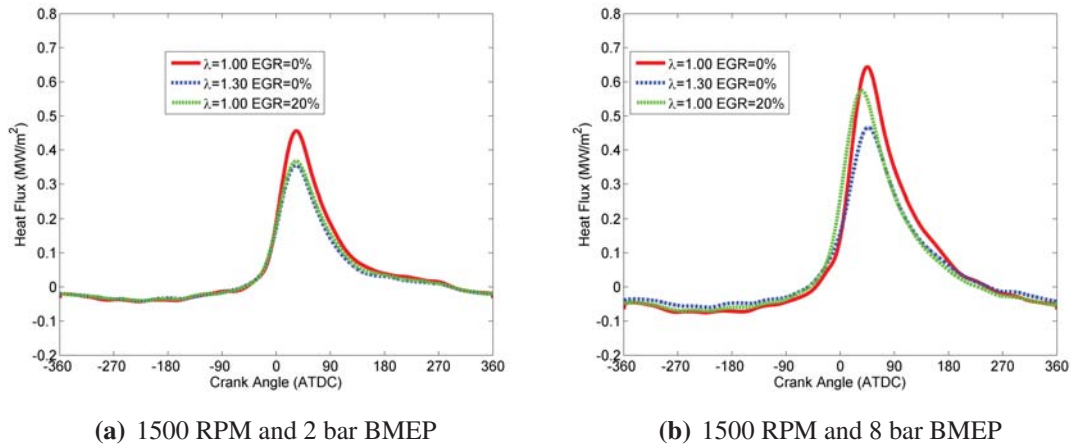


Figure 5.14: Comparison of Cylinder Head Surface Heat Flux Profiles

In order to quantify the effects of dilution on combustion chamber temperatures and heat transfer, the data was sorted by dilution type and amount, and then averaged together. The parameters studied were the change in the average surface temperature of the piston and head and the change in the heat transfer through the cylinder head heat flux probe. The heat transfer through the cylinder head probe was computed by integrating the total surface heat flux over the cycle with respect to time. The resulting value had units of kJ/m^2 and was representative of the heat transfer through the cylinder head. This value was used to quantify the reduction in heat transfer to the coolant from dilute operation. These results were then normalized as functions of the dilution ratio defined in Eq. 5.1. A summary of the results is shown in Table 5.7.

The results showed that dilution from lean operation and EGR was effective at reducing combustion chamber temperatures and heat transfer. For each 1% increase in the dilution ratio, average piston surface temperatures dropped by approximately 0.2% and heat transfer through the cylinder head decreased by about 0.7%. The results showed that lean operation resulted in lower average surface temperatures but higher cylinder head heat transfer compared to EGR for the same amount of dilution.

It was expected that dilution from EGR would have reduced both surface temperatures and heat transfer more than lean operation due to the slightly higher specific heat capacity and longer burn duration. The cylinder head heat flux measurement showed the expected trends

Table 5.7
Effects of Dilution on Combustion Chamber Temperatures and Heat Flux

Parameter		Avg Head STC		Int Heat Flux		Avg Piston STC	
<i>Unit</i>		°C/DR	%/DR	(kJ/m ²)/DR	%/DR	°C/DR	%/DR
Lean	1.15	-0.286	-0.241%	-0.025	-0.616%	-0.434	-0.254%
	1.30	-0.280	-0.237%	-0.030	-0.732%	-0.442	-0.258%
	Avg	-0.283	-0.239%	-0.027	-0.674%	-0.438	-0.256%
EGR	10%	-0.252	-0.213%	-0.029	-0.711%	-0.311	-0.182%
	20%	-0.228	-0.193%	-0.031	-0.778%	-0.324	-0.190%
	Avg	-0.240	-0.203%	-0.030	-0.744%	-0.318	-0.186%

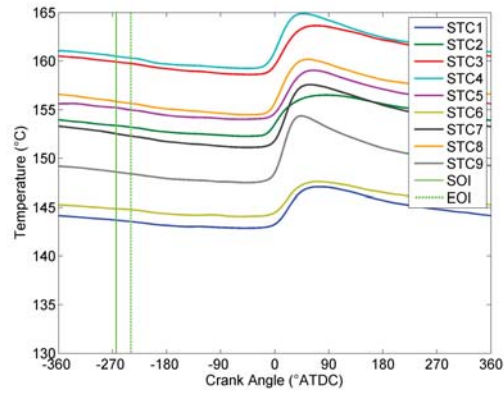
for reduction in heat transfer for dilute combustion; however, the data showed a larger surface temperature decrease for lean operation. Since the exhaust gas temperatures were decreased nearly the same amount, it is believed that this difference was due to variations in engine oil and coolant temperatures. If these temperatures increased, the backside of the head and underside of the piston would have been at higher temperatures and thus for the same heat flux, the surface temperature would have been higher. The coolant temperature set point was 82°C, but it varied by $\pm 2^\circ\text{C}$. The oil temperature was not controlled, but at a given speed and load point, it varied by less than $\pm 2^\circ\text{C}$.

5.6 Fuel Impingement Identification

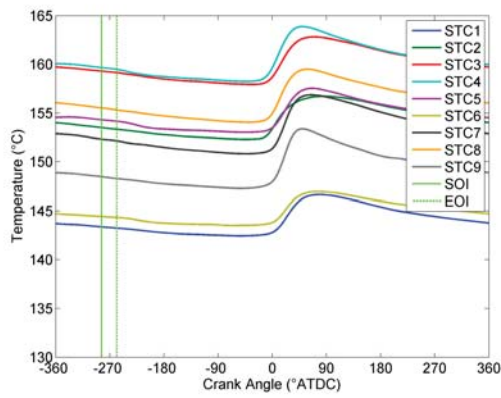
With fast response surface thermocouples installed in a variety of locations around the piston bowl, it was believed that it would be possible to identify fuel spray impingement on the piston. A series of SOI sweeps, with frequent piston cleanings to minimize carbon deposits, was conducted and the results were analyzed from both a surface temperature and heat flux perspective. The goal of the analysis was to find an impingement signature that would identify the injection timings and piston locations where impingement occurred.

The first step in finding an impingement identification signature was looking at the surface temperature profiles. Five SOI timings were tested at several different speed/load points. The results for 1500 RPM and 5 bar BMEP are shown in Fig. 5.15.

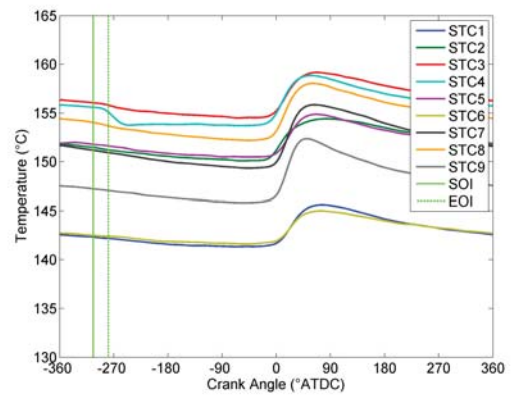
From the large dips in temperature just after the start of injection, it was clear that multiple



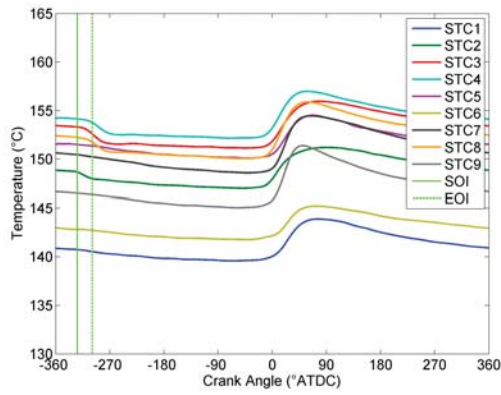
(a) -260° ATDC



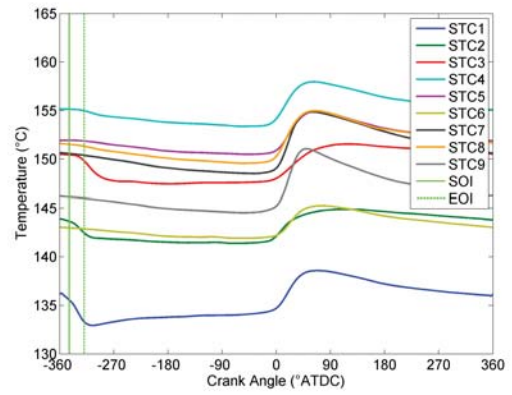
(b) -280° ATDC



(c) -300° ATDC



(d) -320° ATDC



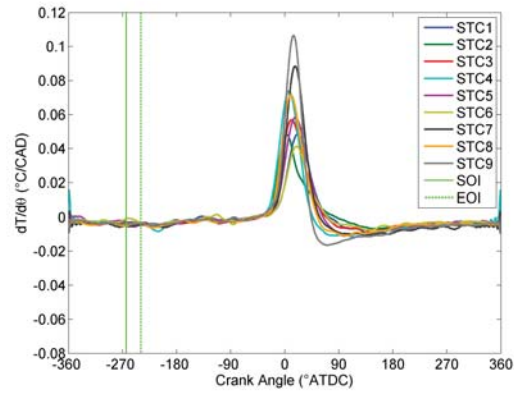
(e) -340° ATDC

Figure 5.15: SOI Sweep STC Results at 1500 RPM and 5 bar BMEP

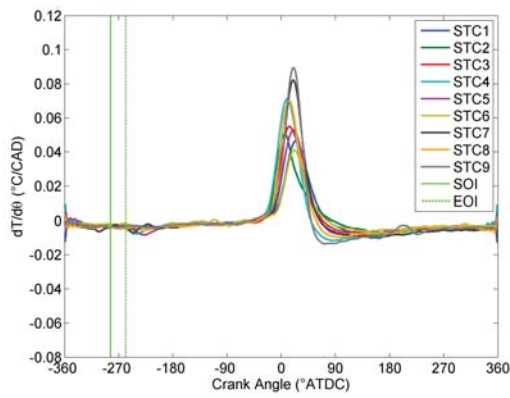
locations were experiencing impingement and that it would be possible to identify the phenomenon from the temperature profile. While it was relatively easy to visually identify the impingement signature, it was desired to find a robust quantitative value that could be used for impingement identification. It was known that the dip in temperature would result in a negative spike in the derivative of temperature with respect to crank angle, $dT/d\theta$. Taking the derivative would also serve to normalize the data and remove the effect of differences in average temperature. The forward difference derivative was computed and the results for the 1500 RPM 5 bar BMEP case are shown in Fig. 5.16.

It was much easier to visually identify an impingement signature using $dT/d\theta$ compared to the surface temperature profile. It was also then possible to quantitatively identify impingement as a local minimum with a value less than some threshold. Determining this threshold was difficult; however, since the minimum value was both a function of the amount of impingement, as well as the response time of the thermocouple. The thicker the deposit layer on the thermocouple the longer the response time and the smaller the spike.

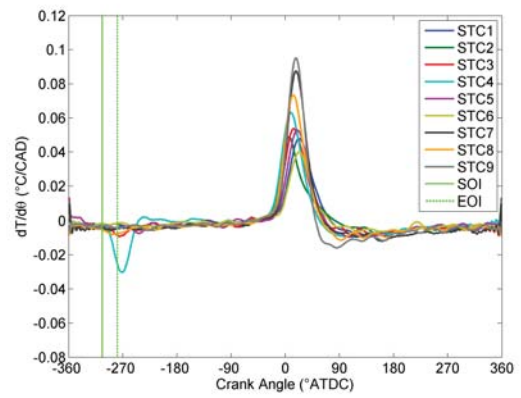
Since it was possible to compute the transient surface heat flux for all the piston surface thermocouples, that parameter was analyzed for an identifiable impingement signature as well. The results of that analysis are shown in Fig. 5.17. The heat flux seemed to provide a slightly smoother and better normalized parameter for impingement identification. In order to mitigate the differences in the minimum value caused by the deposit layer, an attempt was made to normalize the heat flux data for each channel by dividing the profile by the maximum heat flux value from combustion. The maximum value provided an approximation of the response time of each sensor. The results of this normalization are shown in Fig. 5.18. An impingement ID threshold was visually identified and plotted as well. This method proved effective at most of the 1500 RPM SOI sweeps; however, using $dT/d\theta$ proved to be a more robust method for the 3000 RPM SOI sweeps. All of the surface temperature, $dT/d\theta$, and normalized heat flux plots for the various SOI sweeps are shown in Appendix D. The main problem with the normalized heat flux was that the normalization was only effective when the differences in response/deposits were small. For large differences in deposits, the normalization over-amplified the effects for the "dirtier" locations. The difference between the two methods is shown in Fig. 5.19. The impingement event was still clearly visible using the $dt/d\theta$ technique but not for the normalized heat flux technique at 3000 RPM and 5 bar BMEP. Thermocouples 4 and 5 had a large amount of deposits and thus a very damped response and a low peak heat flux, which caused the



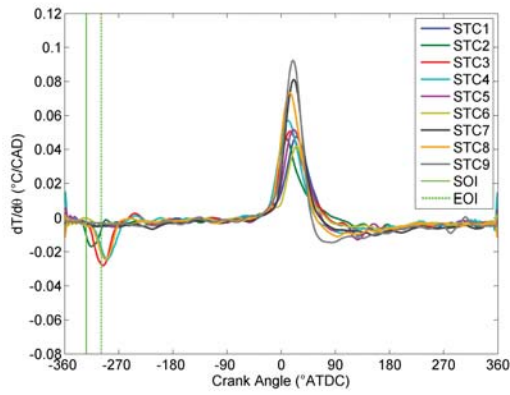
(a) -260° ATDC



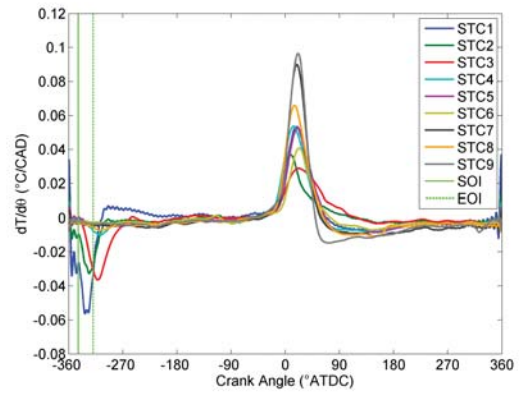
(b) -280° ATDC



(c) -300° ATDC

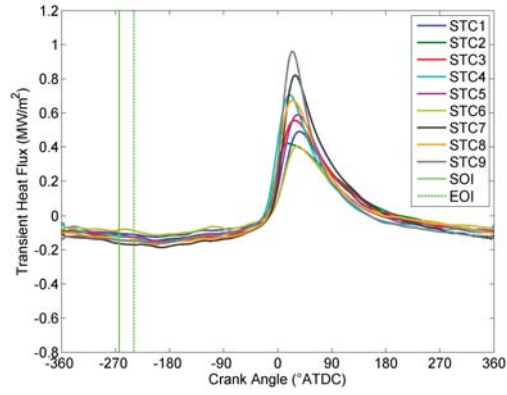


(d) -320° ATDC

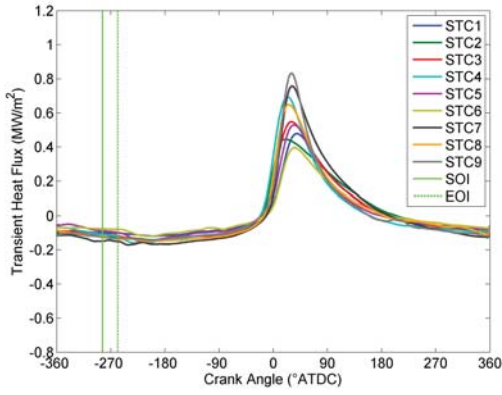


(e) -340° ATDC

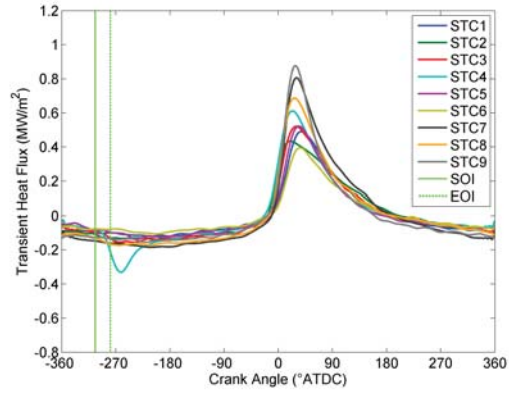
Figure 5.16: SOI Sweep $dT/d\theta$ Results at 1500 RPM and 5 bar BMEP



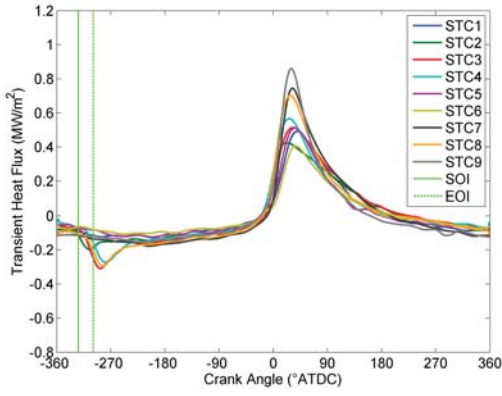
(a) -260° ATDC



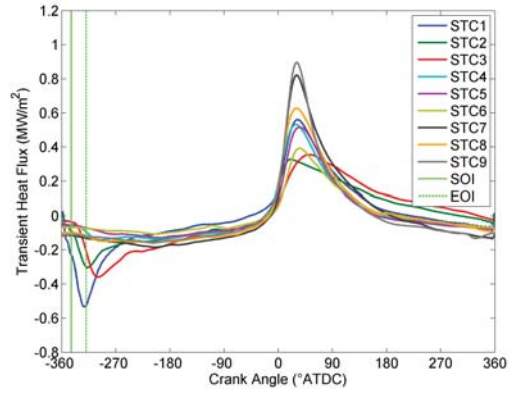
(b) -280° ATDC



(c) -300° ATDC

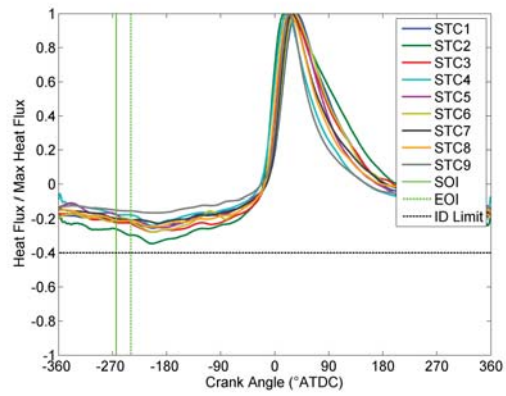


(d) -320° ATDC

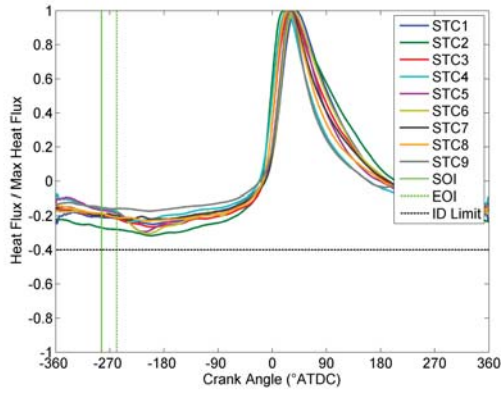


(e) -340° ATDC

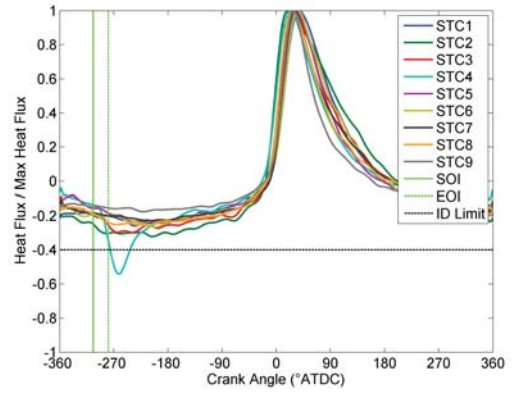
Figure 5.17: SOI Sweep Heat Flux Results at 1500 RPM and 5 bar BMEP



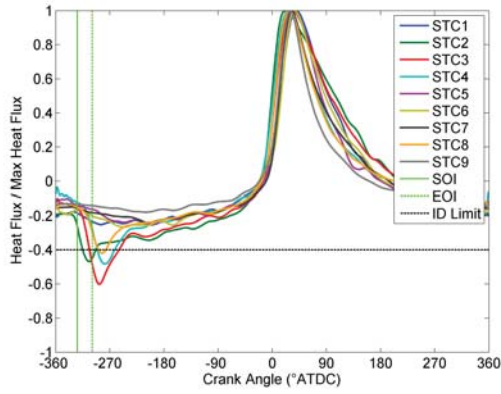
(a) -260° ATDC



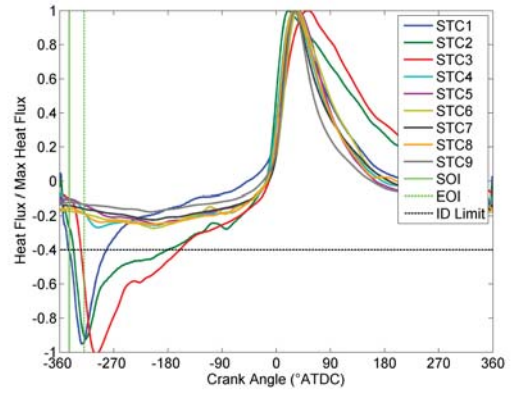
(b) -280° ATDC



(c) -300° ATDC



(d) -320° ATDC

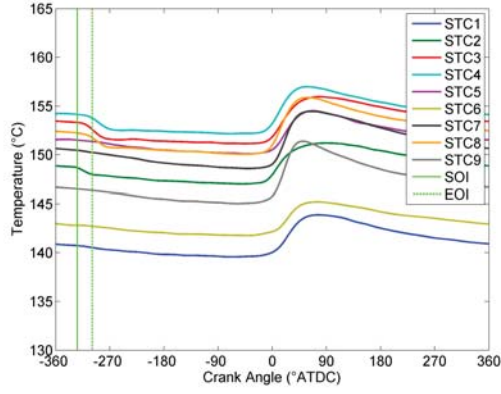


(e) -340° ATDC

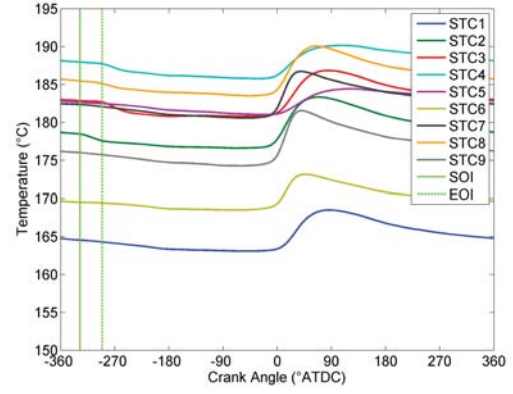
Figure 5.18: SOI Sweep Normalized Heat Flux Results at 1500 RPM and 5 bar BMEP

normalization technique to over-amplify the heat flux for those locations.

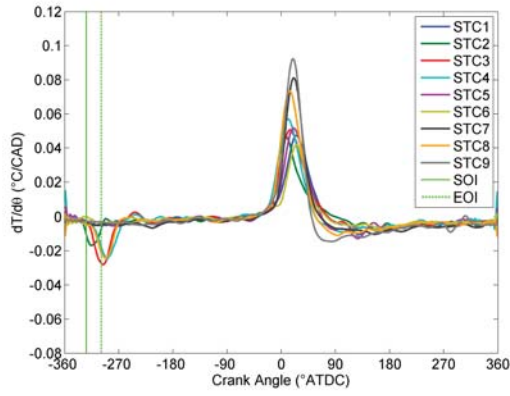
In summary, it was possible to identify impingement using data from fast response surface thermocouples; however, carbon deposits made it difficult to find a standardized algorithm and threshold level. The best method for identifying impingement in the data collected in this research was using $dT/d\theta$, although, for some cases the normalized surface heat flux was also effective. A local minimum in $dT/d\theta$ within 60° of SOI was shown to be indicative of fuel spray impingement. A fixed threshold for the local minimum value was not practical, instead it required analysis on a case by case basis. As expected, the locations that were most susceptible to impingement were those in and around the piston bowl and bowl lip (STCs 1-4 and 8).



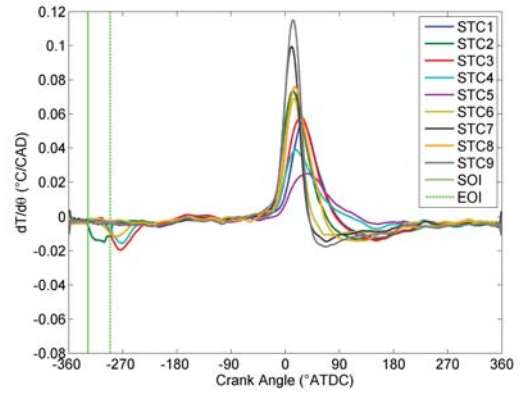
(a) Temperature for 1500/5



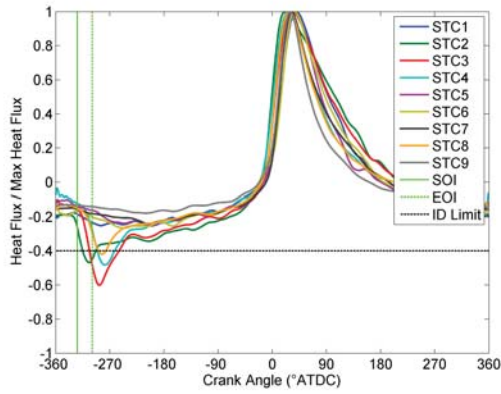
(b) Temperature for 3000/5



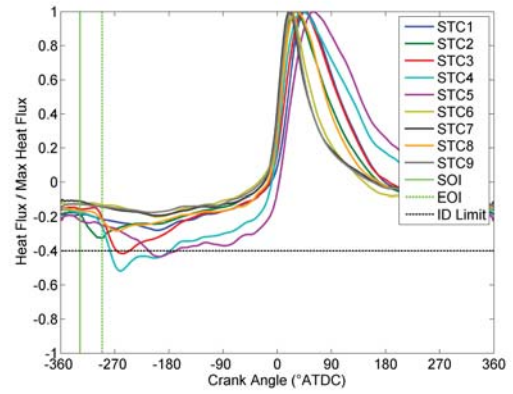
(c) $dt/d\theta$ for 1500/5



(d) $dt/d\theta$ for 3000/5



(e) Normalized Heat Flux for 1500/5



(f) Normalized Heat Flux for 3000/5

Figure 5.19: Comparison of Impingement ID Techniques at an SOI Timing of -320°ATDC

Chapter 6

Conclusions and Recommendations¹

6.1 Conclusions

1. The engine load was confirmed to be the dominant factor in determining the distribution of energy/exergy between brake work, coolant heat transfer, and the exhaust stream. At higher loads, a larger percentage of the energy/exergy went to brake work and the exhaust, while a smaller fraction went to the coolant.
2. While there was a large amount of energy in the coolant, especially under low loads and low speeds, its low temperature resulted in a Carnot efficiency of only 16% and thus the waste heat recovery potential was only 3-6% of the input fuel energy.
3. The high exhaust gas temperatures of SI engines as well as the high exhaust enthalpies make it a good candidate for waste heat recovery systems. Its Carnot efficiencies ranged from 55-75% and thus it would be possible to recover an additional 15-30% of the input fuel energy. However, there is a trade-off between lower temperatures and higher flow rates for lean and dilute combustion that affected the amount of energy/exergy in the exhaust. This trade-off is dependent on operating conditions as well as the location in the exhaust system. Under the conditions studied in this work, this trade-off resulted in an energy increase in 100% of the cases for CV 1 and 85% of the cases for CV 2, but the exergy only increased for 87% of the cases for CV 1 and 43% of the cases for CV 2.

¹The material contained in this chapter is planned for submission as part of a journal article and/or conference paper in the future.

4. Downsizing and downspeeding have the potential to improve fuel economy by shifting the engine to a more efficient operating point. Utilizing lean combustion and adding exhaust waste heat recovery could improve the thermal efficiency of the engine to over 55%.
5. An empirical model was developed that calculates the energy distribution of the engine as well as the exhaust gas temperature at the manifold. This model further proved that engine load was the dominant factor controlling the engine energy distribution.
6. A dilution ratio was defined that enabled comparisons between the normalized effects of lean operation and EGR. Utilizing this parameter, it was shown that dilution from lean operation resulted in a similar in-cylinder (0.3°C per 1% dilution) and exhaust gas (3.3°C per 1% dilution) temperature reduction, but an 85% larger brake efficiency increase compared to the same amount of dilution from EGR. The difference in efficiency improvement was the result of longer burn durations and smaller increases in gamma for EGR compared to lean operation.
7. Two methods for identifying fuel spray impingement on the piston were found and proven effective. However, there was not a single method and threshold value that worked for all operating conditions. If the surface thermocouples were all clean and had similar response characteristics, either method would have been effective and it is likely a single threshold value could have been found.

6.2 Recommendations for Future Work

- The instrumentation was not in place during this research to complete a thorough study of the turbocharger as waste heat recovery mechanism. It would be beneficial to understand the amount of work that was recovered by the turbocharger and how efficient it was under lean and dilute conditions. This would require additional temperature and pressure measurements to be added to the exhaust and intake system.
- The effects of dilute combustion via lean operation and EGR could be integrated into the simple empirical model. This could potentially be done with a multiplication factor that would be applied to the base model results. The base model could also

be greatly improved by collecting data at lower engine speeds as well as for no load conditions at the engine speeds already tested.

- With the SOI timings that resulted in fuel spray impingement known, it would be possible to explore the engine performance implications of impingement. Taking emissions measurements or analyzing the existing fuel flow and brake efficiency data would lead to an understanding of whether or not all the fuel was able to be evaporated at late injection timings.
- Since the carbon deposits on the piston caused problems with some of the data analysis, it would be advisable to perform a study to better understand the growth of the deposit layer, how it affects the thermocouple, and what the best method for cleaning would be. This could be performed on thermocouples installed in an Aluminum block with a soot generation mechanism.

References

- [1] Stokes, J., Lake, T. H., and Osborne, R. J., 2000. “A Gasoline Engine Concept for Improved Fuel Economy - The Lean Boost System”. *SAE Technical Paper*, 2000-01-2902.
- [2] Duchaussoy, Y., Lefebvre, A., and Bonetto, R., 2003. “Dilution Interest on Turbocharged SI Engine Combustion”. *SAE Technical Paper*, 2003-01-0629.
- [3] Wirth, M., Mayerhofer, U., Piock, W. F., and Fraidl, G. K., 2000. “Turbocharging the DI Gasoline Engine”. *SAE Technical Paper*, 2000-01-0251.
- [4] Suzuki, M., Ueda, S., and Watanabe, T., 2006. “Real-time Piston Temperature Measurement using Induction Telemetry System”. *SAE Technical Paper*, 2006-01-1248.
- [5] Lee, H., Oh, C., Kauh, S., and Ha, K., 2006. “Development of a Multipiston Temperature Telemetry System Using Bluetooth Networks”. *Proc. IMechE Part D: Journal of Automobile Engineering*, **220**(2), pp. 127–138.
- [6] NHTSA, 2012. Corporate average fuel economy (cafe). Web, August.
- [7] Farrell, J. T., Stevens, J. G., and Weissman, W., 2006. “A Second Law Analysis of High Efficiency Low Emission Gasoline Engine Concepts”. *SAE Technical Paper*, 2006-01-0491.
- [8] Attard, W. P., and Blaxill, H., 2012. “A lean burn gasoline fueled pre-chamber jet ignition combustion system achieving high efficiency and low nox at part load”. *SAE Technical Paper*(2012-01-1146), 04.
- [9] Hsu, C.-T., Huang, G.-Y., Chu, H.-S., Yu, B., and Yao, D.-J., 2011. “Experiments and simulations on low-temperature waste heat harvesting system by thermoelectric power generators”. *Applied Energy*, **88**(4), pp. 1291 – 1297.
- [10] Wang, Y., Dai, C., and Wang, S., 2013. “Theoretical analysis of a thermoelectric generator using exhaust gas of vehicles as heat source”. *Applied Energy*(0).

- [11] Macián, V., Serrano, J., Dolz, V., and Sánchez, J., 2013. “Methodology to design a bottoming rankine cycle, as a waste energy recovering system in vehicles. study in a {HDD} engine”. *Applied Energy*, **104**(0), pp. 758 – 771.
- [12] Horst, T. A., Rottengruber, H.-S., Seifert, M., and Ringler, J., 2013. “Dynamic heat exchanger model for performance prediction and control system design of automotive waste heat recovery systems”. *Applied Energy*, **105**(0), pp. 293 – 303.
- [13] Pandiyarajan, V., Pandian, M. C., Malan, E., Velraj, R., and Seeniraj, R., 2011. “Experimental investigation on heat recovery from diesel engine exhaust using finned shell and tube heat exchanger and thermal storage system”. *Applied Energy*, **88**(1), pp. 77 – 87.
- [14] Xie, H., and Yang, C., 2013. “Dynamic behavior of rankine cycle system for waste heat recovery of heavy duty diesel engines under driving cycle”. *Applied Energy*, **112**(0), pp. 130 – 141.
- [15] Zhang, H., Wang, E., and Fan, B., 2013. “A performance analysis of a novel system of a dual loop bottoming organic rankine cycle (orc) with a light-duty diesel engine”. *Applied Energy*, **102**(0), pp. 1504 – 1513.
- [16] Hughes, C., Mitts, C., Jacquelin, F., and Wiseman, M., 2001. “Heavy Duty Truck Cooling System Design Using Co-Simulation”. *SAE Technical Paper*, 2001-01-1707.
- [17] Luptowski, B. J., Arici, O., Johnson, J. H., and Parker, G. G., 2005. “Development of the Enhanced Vehicle and Engine Cooling System Simulation and Application to Active Cooling Control”. *SAE Technical Paper*, 2005-01-0697.
- [18] Boyce, B. P., Martin, J. K., Poehlman, A., and Shears, D., 1999. “Effects of Ignition Timing and Air-Fuel Ratio on In-Cylinder Heat Flux and Temperatures in a Four-Stroke, Air Cooled, Homogeneous Charge Engine”. *SAE Technical Paper*, 1999-01-0284.
- [19] Borman, G., and Nishiwaki, K., 1987. “Internal-Combustion Engine Heat Transfer”. *Progress in Energy and Combustion Science*, **13**(1), pp. 1 – 46.
- [20] Caton, J. A., 2000. “Operating Characteristics of a Spark-Ignition Engine Using the Second Law of Thermodynamics: Effects of Speed and Load”. *SAE Technical Paper*, 2000-01-0952.
- [21] Caton, J. A., 2006. “Utilizing a Cycle Simulation to Examine the Use of EGR for a Spark-Ignition Engine Including the Second Law of Thermodynamics”. *ASME Conference Proceedings*, **2006**(42606), pp. 31–46.
- [22] Ayala, F. A., Gerty, M. D., and Heywood, J. B., 2006. “Effects of Combustion Phasing, Relative Air-fuel Ratio, Compression Ratio, and Load on SI Engine Efficiency”. *SAE Technical Paper*, 2006-01-0229.

- [23] Güralp, O., Hoffman, M., Assanis, D., Filipi, Z., Kuo, T.-W., Najt, P., and Rask, R., 2009. “Thermal Characterization of Combustion Chamber Deposits on the HCCI Engine Piston and Cylinder Head Using Instantaneous Temperature Measurements”. *SAE Technical Paper*, 2009-01-0668.
- [24] Güralp, O., Najt, P., and Filipi, Z. S., 2012. “Method for Determining Instantaneous Temperature at the Surface of Combustion Chamber Deposits in an HCCI Engine”. *ASME Conference Proceedings*, **ICEF2012-92188**, 790825.
- [25] Hochgreb, S., 2001. “Liquid Fuel Impingement on the Piston Bowl of a Direct-Injection, Spark-Ignited (DISI) Engine under Stratified Operation”. *SAE Technical Paper*, 2001-01-3646.
- [26] Chang, J., Fillpi, Z., Assanis, D., Kuo, T.-W., Najt, P., and Rask, R., 2005. “Characterizing the Thermal Sensitivity of a Gasoline Homogeneous Charge Compression Ignition Engine with Measurements of Instantaneous Wall Temperature and Heat Flux”. *International Journal of Engine Research*, **6**(4), pp. 289 – 309.
- [27] Eichelberg, G., 1939. “Some New Investigations on Old Combustion Engine Problems”. *Engineering*, **148**, pp. 463–466, 547–550.
- [28] TESTING ENGINEER’S INC., 2004. *Templug User Information Guide*, rev. 3.0 ed.
- [29] Madison, D., Miers, S., Barna, G., and Richerson, J., 2012. “Comparison of Piston Temperature Measurement Methods: Templugs Versus Wireless Telemetry with Thermocouples”. *ASME Conference Proceedings*, **ICEF2012-92184**.
- [30] Hendricks, T., and Ghandhi, J., 2012. “Estimation of Surface Heat Flux in IC Engines Using Temperature Measurements: Processing Code Effects”. *SAE Int. J. Engines*, **5**(2012-01-1208), 04, pp. 1268–1285.
- [31] Bendersky, D., 1953. “A Special Thermocouple for Measuring Transient Temperatures”. *Mechanical Engineering*, **75**, pp. 117–121.
- [32] Medtherm Corporation, 2006. Coaxial Surface Thermocouple Probes. Tech. rep., Bulletin 500.
- [33] Moeller, C. E., 1962. “Thermocouples for the Measurement of Transient Surface Temperatures”. *TEMPERATURE, Its Measurement and Control in Science and Industry*, **3**(2), pp. 617–623.
- [34] Buttsworth, D. R., Stevens, R., and Stone, C. R., 2005. “Eroding Ribbon Thermocouples: Impulse Response and Transient Heat Flux Analysis”. *Measurement Science and Technology*, **16**(7), pp. 1487–1494.

- [35] Wilson, T. S., Bryanston-Cross, P. J., Chana, K. S., Dunkley, P., Jones, T. V., and Hannah, P., 2002. “High Bandwidth Heat Transfer and Optical Measurements in an Instrumented Spark Ignition Internal Combustion Engine”. *SAE Technical Paper*, 2002-01-0747.
- [36] Wimmer, A., Pivec, R., and Sams, T., 2000. “Heat Transfer to the Combustion Chamber and Port Walls of IC Engines - Measurement and Prediction”. *SAE Technical Paper*, 2000-01-0568.
- [37] Vatel Corporation, 2011. HFM (Heat Flux Microsensor). Web.
- [38] Syrimis, M., 1996. “Characterization of Knocking Combustion and Heat Transfer in a Spark Ignition Engine”. PhD thesis, University of Illinois at Urbana-Champaign.
- [39] Hendricks, T., 2011. “Instantaneous Surface Heat Flux Measurements in Internal Combustion Engines”. PhD thesis, University of Wisconsin-Madison.
- [40] Kato, N., Moritsugu, M., Shimura, T., and Matsui, J., 2001. “Piston Temperature Measuring Technology Using Electromagnetic Induction”. *SAE Technical Paper*, 2001-01-2027.
- [41] Miers, S. A., Barna, G. L., Anderson, C. L., Blough, J. R., Inal, M. K., and Ciatti, S. A., 2008. “A Wireless Microwave Telemetry Data Transfer Technique for Reciprocating and Rotating Components”. *Journal of Engineering for Gas Turbines and Power*, **130**(2), pp. 1–9.
- [42] Miers, S. A., Anderson, C. L., Blough, J. R., and Inal, M. K., 2005. “Impingement Identification in a High Speed Diesel Engine Using Piston Surface Temperature Measurements”. *SAE Technical Paper*, 2005-01-1909.
- [43] Hohenberg, G., 1979. “Advanced Approaches for Heat Transfer Calculations”. *SAE Technical Paper*, 790825.
- [44] Annand, W. J. D., 1963. “Heat Transfer in the Cylinders of Reciprocating Internal Combustion Engines”. *Proc. IMechE*, **177**(36), pp. 973–990.
- [45] Woschni, G., 1967. “Universally Applicable Equation for the Instantaneous Heat Transfer Coefficient in the Internal Combustion Engine”. *SAE Technical Paper*, 670931.
- [46] LeFeuvre, T., Myers, P. S., and Uyehara, O. A., 1969. “Experimental Instantaneous Heat Fluxes in a Diesel Engine and Their Correlation”. *SAE Technical Paper*, 690464.
- [47] Alkidas, A. C., 1980. “Heat Transfer Characteristics of a Spark-Ignition Engine”. *ASME Journal of Heat Transfer*, **102**, pp. 189–193.

- [48] Nusselt, W., 1923. “Die Wärmeübergang in den Verbrennungs-kraftmaschinen”. *Z. Ver. Dtsch. Ing.*, **67**, pp. 692–708.
- [49] Hayes, T. K., White, R., and Peters, J. E., 1993. “Combustion Chamber Temperature and Instantaneous Local Heat Flux Measurements in a Spark Ignition Engine”. *SAE Technical Paper*, 930217.
- [50] Enomoto, Y., Nagano, H., and Koyama, T., 1995. “Measurement of Wall Surface Temperature in a Combustion Chamber in Automobile 4-Stroke Engines”. *Proceedings of the Institution of Mechanical Engineers*, **C496/012**, pp. 575–585.
- [51] Miers, S. A., 2004. “Identification and Characterization of Impingement Signatures in a High Speed Diesel Engine using Piston Surface Temperature Measurements”. PhD thesis, Michigan Technological University.
- [52] Chammas, R. E., and Clodic, D., 2005. “Combined Cycle for Hybrid Vehicles”. *SAE Technical Paper*, 2005-01-1171.
- [53] Caton, J. A., 2000. “A Review of Investigations Using the Second Law of Thermodynamics to Study Internal-Combustion Engines”. *SAE Technical Paper*, 2000-01-1081.
- [54] Caton, J. A., 2006. “First and Second Law Analyses of a Spark-Ignition Engine Using Either Isooctane or Hydrogen: An Initial Assessment”. *ASME Conference Proceedings*, **2006**(42606), pp. 47–66.
- [55] Caton, J. A., 2010. “An Assessment of the Thermodynamics Associated With High-Efficiency Engines”. *ASME Conference Proceedings*, **2010**(49446), pp. 301–317.
- [56] Caton, J. A., 2013. “A Comparison of Lean Operation and Exhaust Gas Recirculation: Thermodynamic Reasons for the Increases of Efficiency”. *SAE Technical Paper*, 2013-01-0266.
- [57] Xin, Q. H., and Zheng, J., 2009. “Theoretical Analysis of Internal Combustion Engine Miscellaneous Heat Losses”. *SAE Technical Paper*, 2009-01-2881.
- [58] Smith, L. A., Preston, W. H., Dowd, G., Taylor, O., and Wilkinson, K. M., 2009. “Application of a First Law Heat Balance Method to a Turbocharged Automotive Diesel Engine”. *SAE Technical Paper*, 2009-01-2744.
- [59] Fu, J., Liu, J., Feng, R., Yang, Y., Wang, L., and Wang, Y., 2013. “Energy and exergy analysis on gasoline engine based on mapping characteristics experiment”. *Applied Energy*, **102**(0), pp. 622 – 630.
- [60] ECTRON CORPORATION, 2010. *Instruction Manual for Model 563H Transducer Conditioner-Amplifier*.

- [61] Barna, G., 2012. Personal Communiatiion. IR Telemetrics.
- [62] Kirwan, J. E., Shost, M., Roth, G., and Zizelman, J., 2010. “3-Cylinder Turbocharged Gasoline Direct Injection: A High Value Solution for Low CO₂ and NO_x Emissions”. *SAE Int. J. Engines*, **3**, 04, pp. 355–371.
- [63] Mathworks, 2013. Local Regression Smoothing. Web, November.
- [64] Heywood, J., 1988. *Internal Combustion Engine Fundamentals*. McGraw-Hill series in mechanical engineering. McGraw-Hill.
- [65] Assanis, D. N., and Badillo, E., 1989. “Evaluation of Alternative Thermocouple Designs for Transient Heat Transfer Measurements in Metal and Ceramic Engines”. *SAE Technical Paper*, 890571.
- [66] Özcan, H., and Söylemez, M., 2006. “Thermal balance of a {LPG} fuelled, four stroke {SI} engine with water addition”. *Energy Conversion and Management*, **47**(5), pp. 570 – 581.
- [67] Gharehghani, A., M.Koochak, Mirsalim, M., and Yusaf, T., 2013. “Experimental investigation of thermal balance of a turbocharged {SI} engine operating on natural gas”. *Applied Thermal Engineering*(0).
- [68] Lavoie, G., Ortiz-Soto, E., Babajimopoulos, A., Martz, J. B., and Assanis, D. N., 2012. “Thermodynamic sweet spot for high-efficiency, dilute, boosted gasoline engines”. *International Journal of Engine Research*.
- [69] Syed, I. Z., Yeliana, Y., Mukherjee, A., Naber, J. D., and Michalek, D., 2010. “Numerical Investigation of Laminar Flame Speed of Gasoline - Ethanol/Air Mixtures with Varying Pressure, Temperature and Dilution”. *SAE Int. J. Engines*, **3**, 04, pp. 517–528.

Appendix A

Additional Energy and Exergy Balance Analysis Plots¹

A.1 Interaction Plots for CV 2

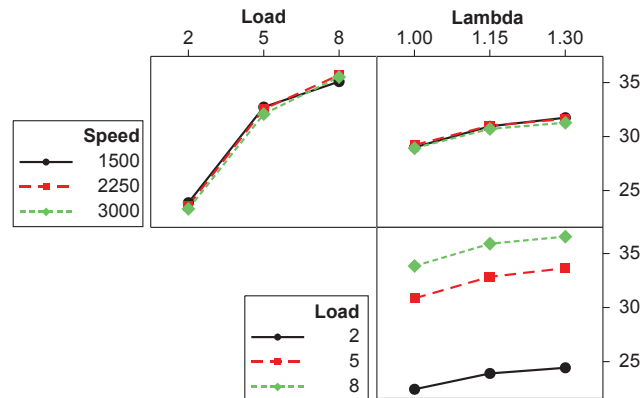


Figure A.1: Interaction Plot for Brake Efficiency Under Lean Conditions

¹The material contained in this chapter is planned for submission as part of a journal article and/or conference paper in the future.

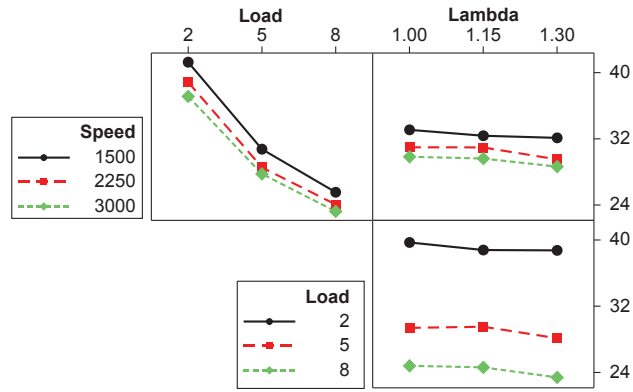


Figure A.2: Interaction Plot for Coolant Heat Energy Under Lean Conditions

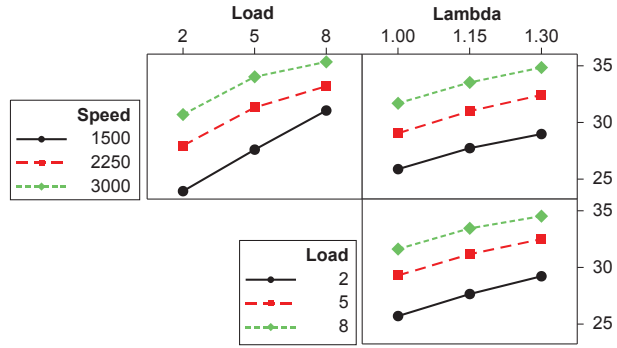


Figure A.3: Interaction Plot for Exhaust Heat Energy Under Lean Conditions

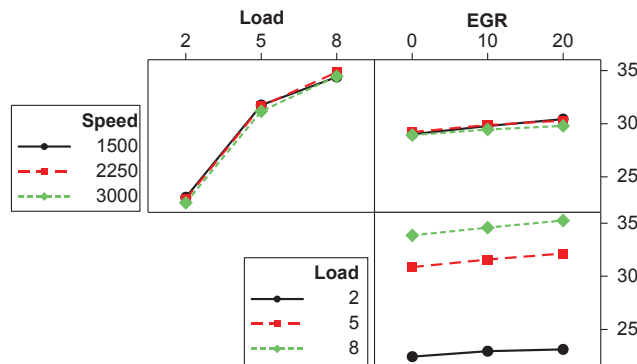


Figure A.4: Interaction Plot for Brake Efficiency with EGR

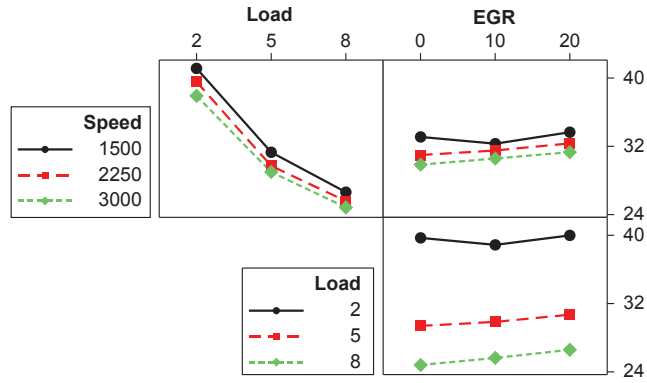


Figure A.5: Interaction Plot for Coolant Heat Energy with EGR

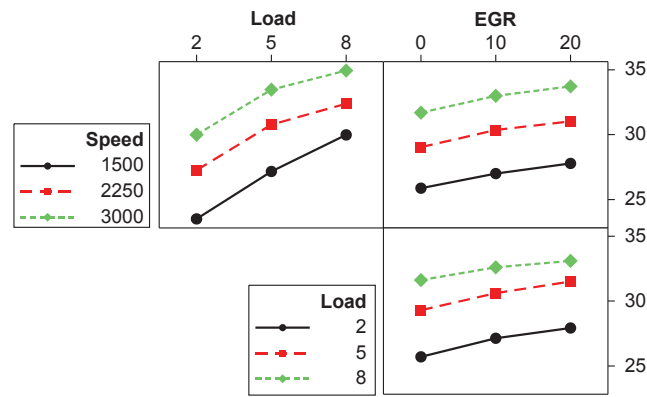
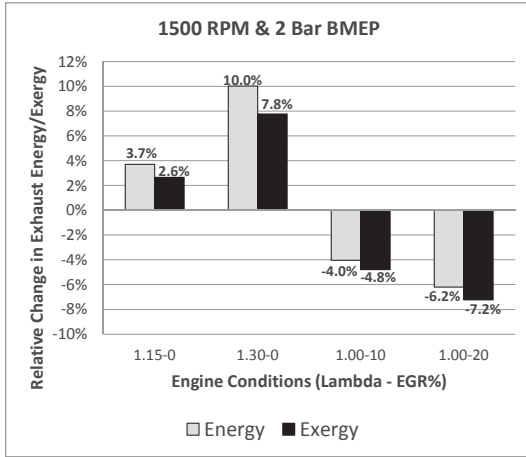
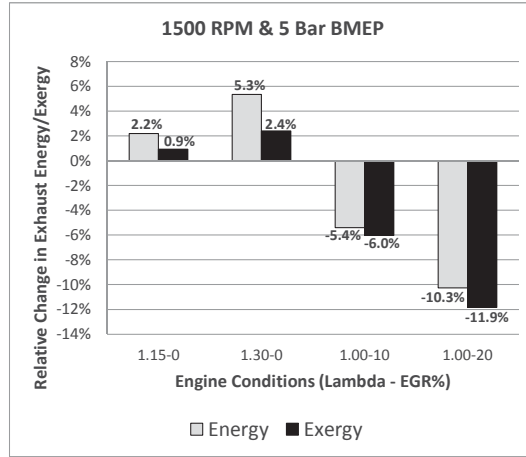


Figure A.6: Interaction Plot for Exhaust Heat Energy with EGR

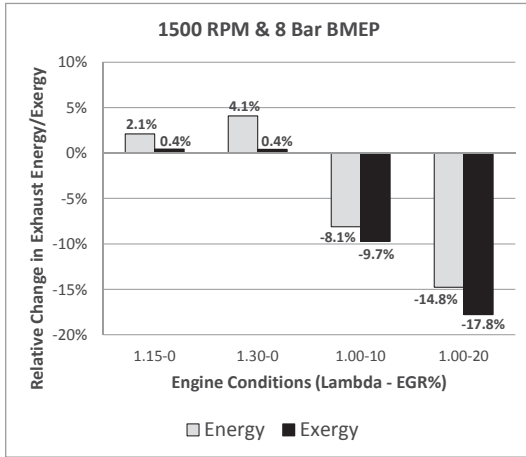
A.2 Exhaust Energy and Exergy Plots



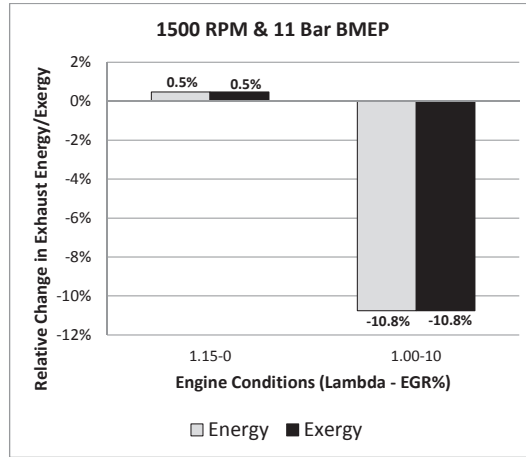
(a) 1500 RPM and 2 bar



(b) 1500 RPM and 5 bar

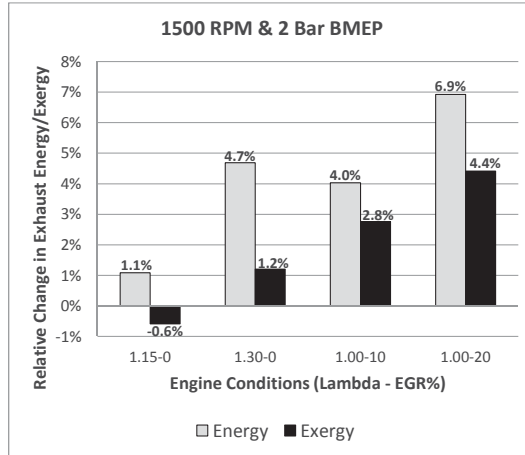


(c) 1500 RPM and 8 bar

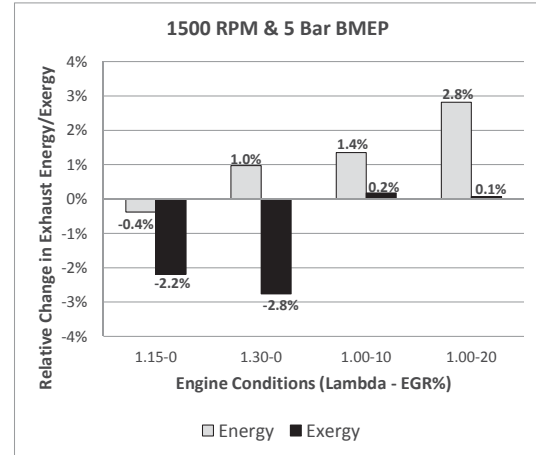


(d) 1500 RPM and 11 bar

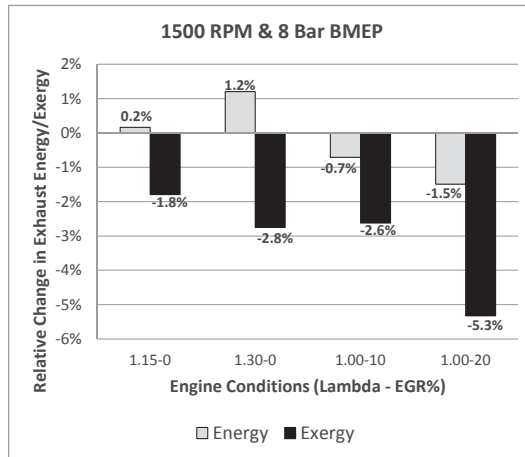
Figure A.7: Comparison of Exhaust Energy and Exergy for CV 1 at 1500 RPM



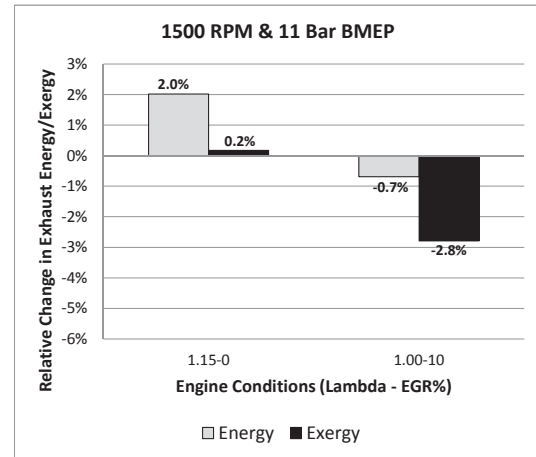
(a) 1500 RPM and 2 bar



(b) 1500 RPM and 5 bar

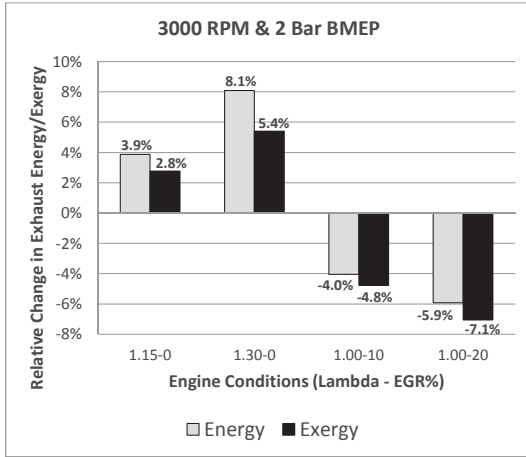


(c) 1500 RPM and 8 bar

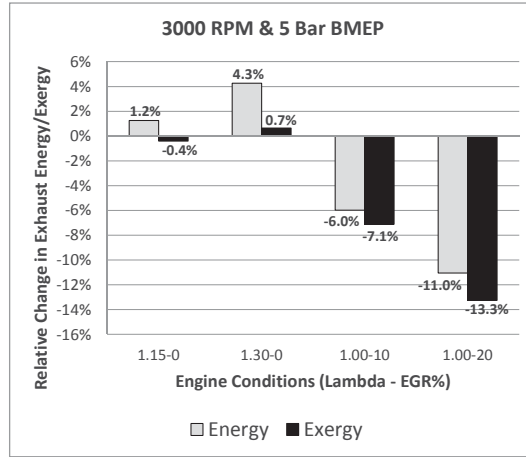


(d) 1500 RPM and 11 bar

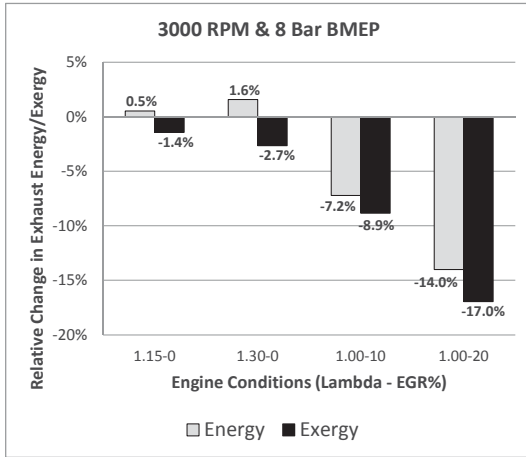
Figure A.8: Comparison of Exhaust Energy and Exergy for CV 2 at 1500 RPM



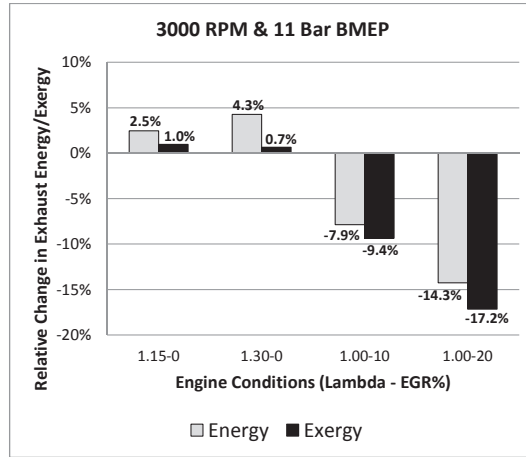
(a) 3000 RPM and 2 bar



(b) 3000 RPM and 5 bar

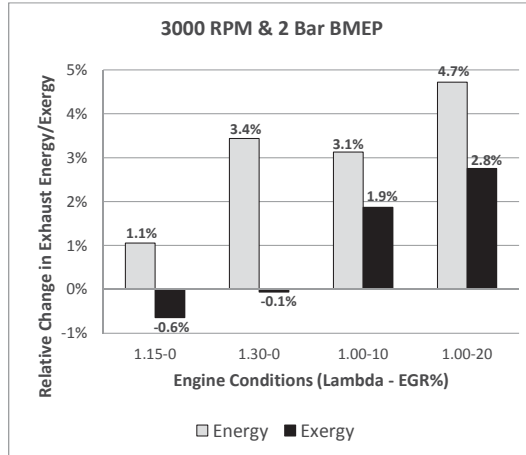


(c) 3000 RPM and 8 bar

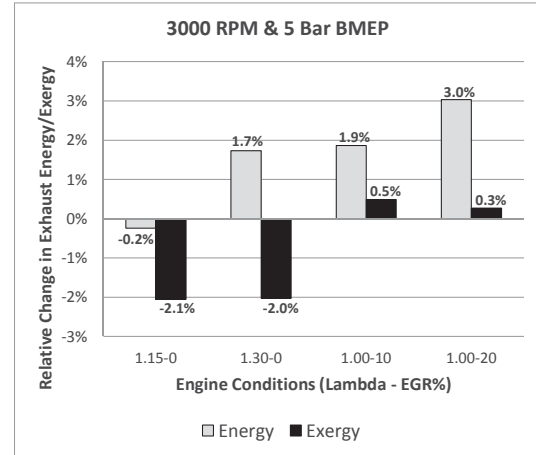


(d) 3000 RPM and 11 bar

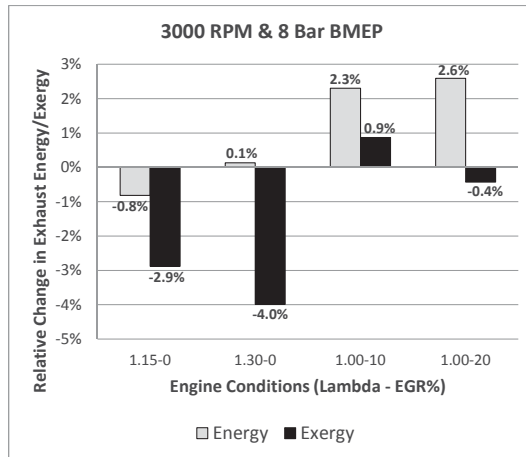
Figure A.9: Comparison of Exhaust Energy and Exergy for CV 1 at 3000 RPM



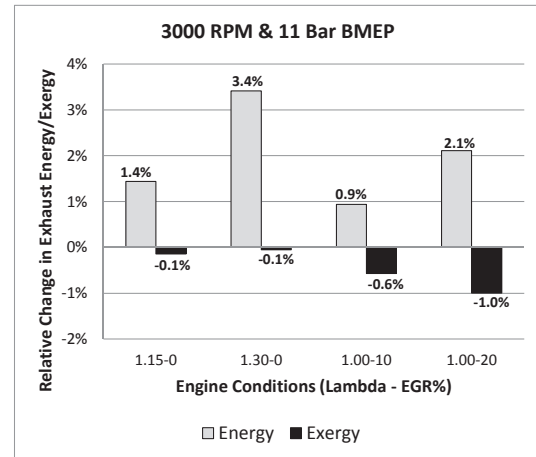
(a) 3000 RPM and 2 bar



(b) 3000 RPM and 5 bar



(c) 3000 RPM and 8 bar



(d) 3000 RPM and 11 bar

Figure A.10: Comparison of Exhaust Energy and Exergy for CV 2 at 3000 RPM

Appendix B

Control Point Repeatability¹

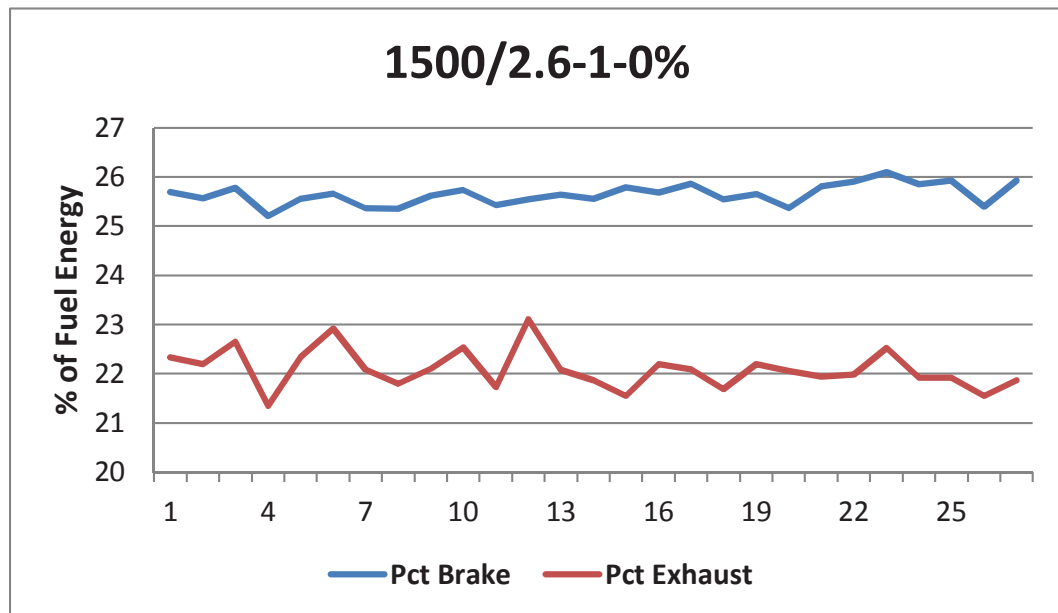


Figure B.1: Repeatability of the Brake Efficiency and Exhaust Energy Percentage for the 1500/2.6 Control Point

¹The material contained in this chapter is planned for submission as part of a journal article and/or conference paper in the future.

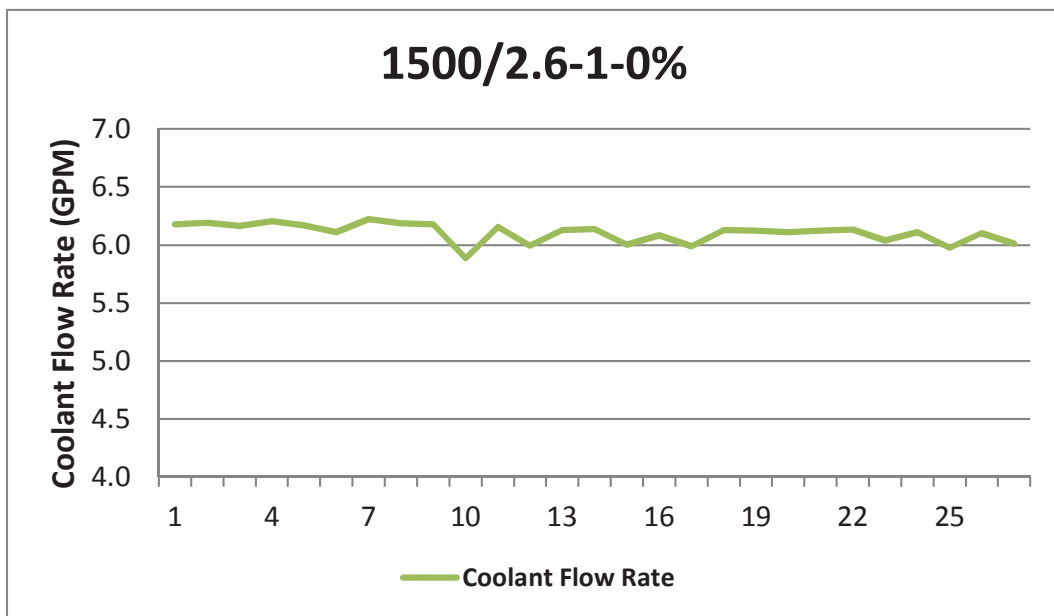
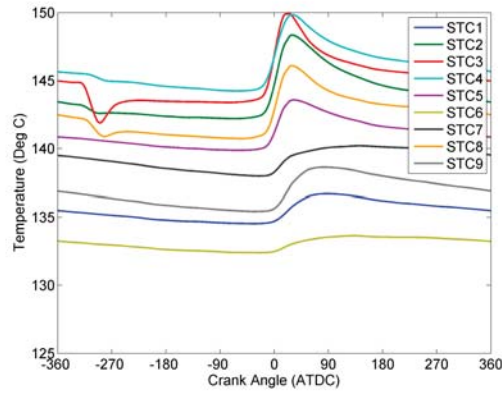


Figure B.2: Repeatability of the Coolant Flow Rate for the 1500/2.6 Control Point

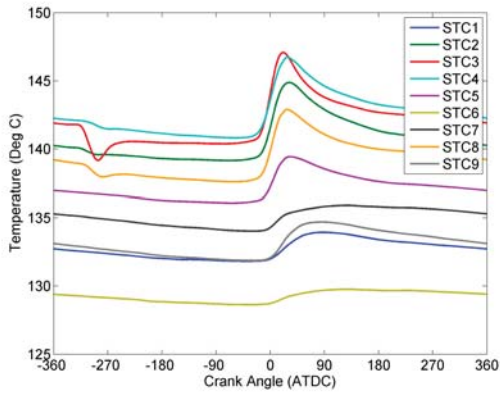
Appendix C

Additional Combustion Chamber Temperature and Heat Flux Plots¹

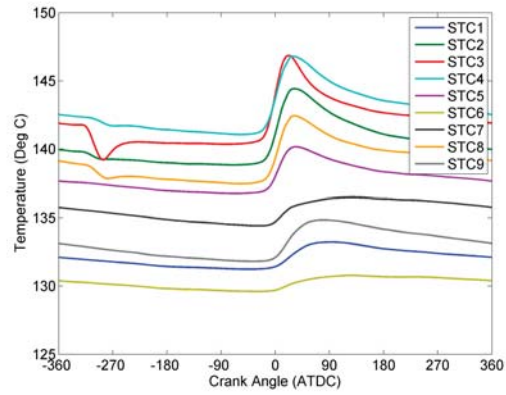
¹The material contained in this chapter is planned for submission as part of a journal article and/or conference paper in the future.



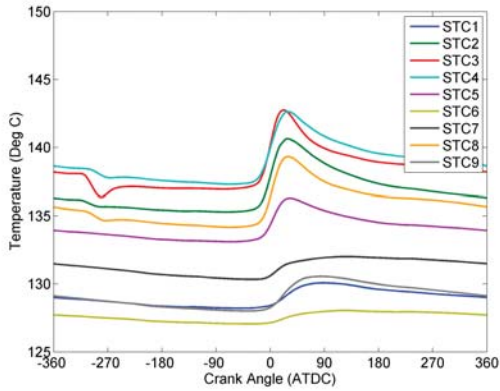
(a) $\lambda = 1.00$ and $EGR = 0\%$



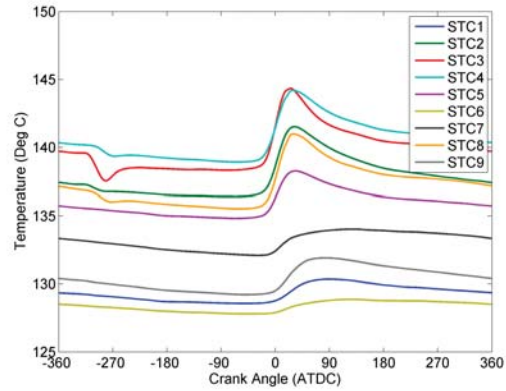
(b) $\lambda = 1.15$ and $EGR = 0\%$



(c) $\lambda = 1.00$ and $EGR = 10\%$

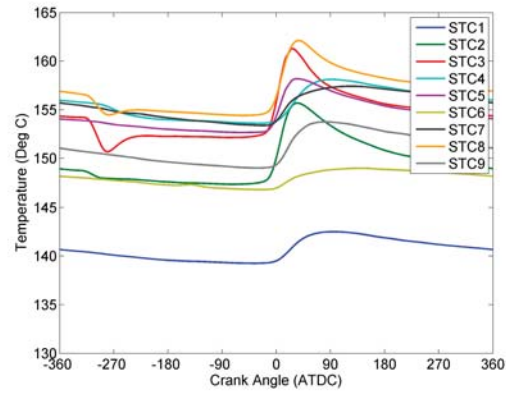


(d) $\lambda = 1.30$ and $EGR = 0\%$

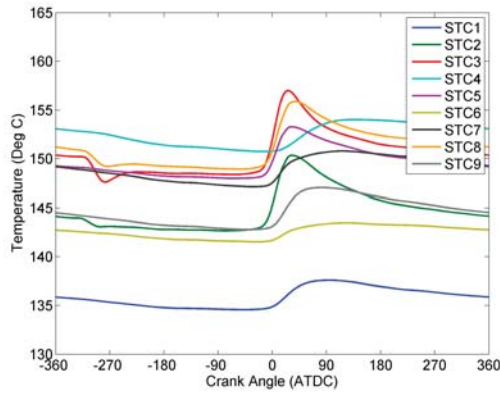


(e) $\lambda = 1.00$ and $EGR = 20\%$

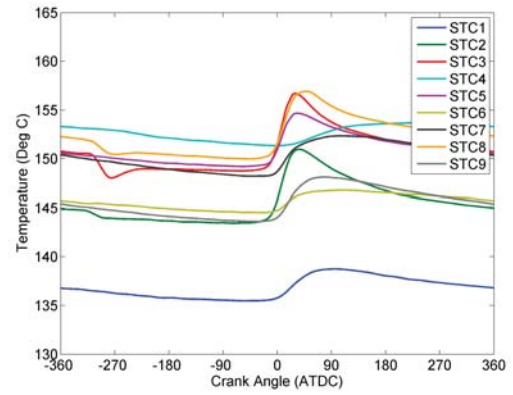
Figure C.1: Piston Temperature Plot for 1500 RPM and 2 bar BMEP



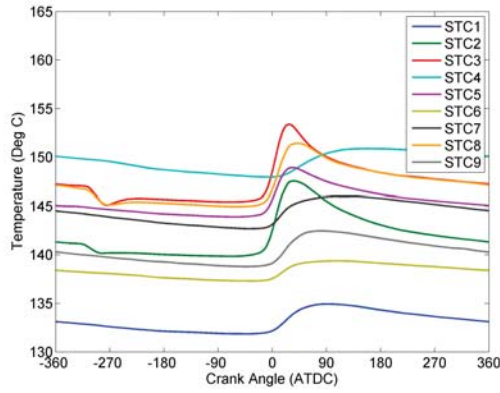
(a) $\lambda = 1.00$ and $EGR = 0\%$



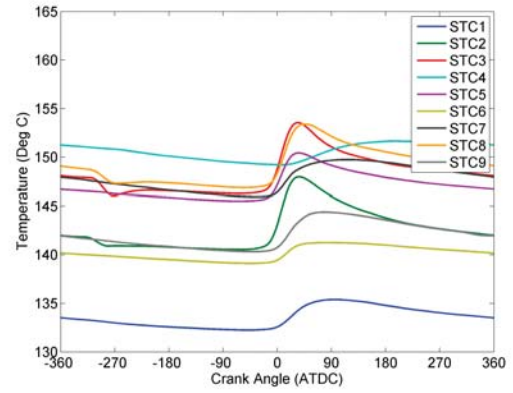
(b) $\lambda = 1.15$ and $EGR = 0\%$



(c) $\lambda = 1.00$ and $EGR = 10\%$

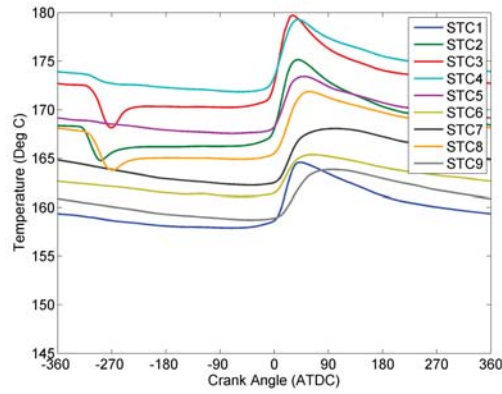


(d) $\lambda = 1.30$ and $EGR = 0\%$

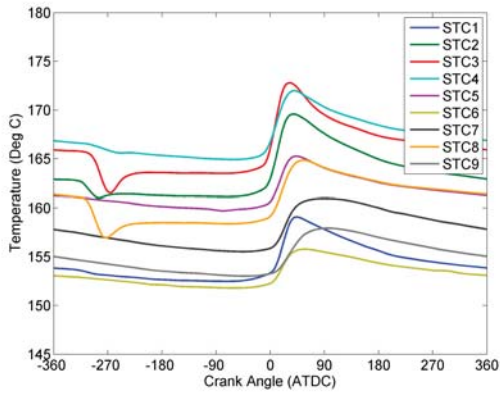


(e) $\lambda = 1.00$ and $EGR = 20\%$

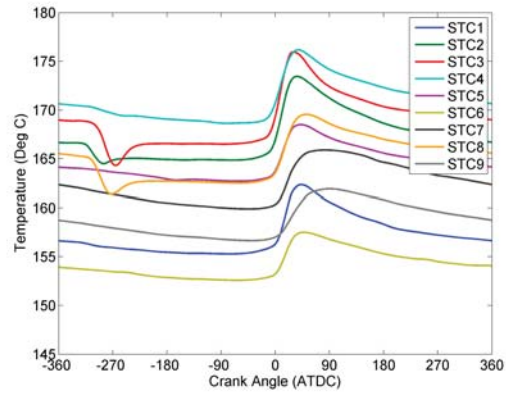
Figure C.2: Piston Temperature Plot for 1500 RPM and 5 bar BMEP



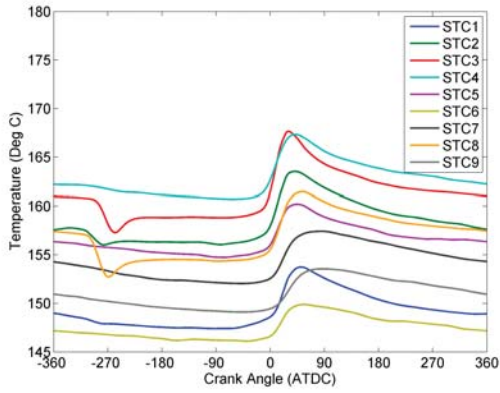
(a) $\lambda = 1.00$ and $EGR = 0\%$



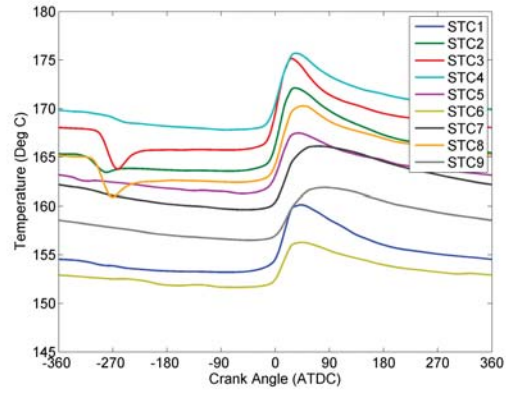
(b) $\lambda = 1.15$ and $EGR = 0\%$



(c) $\lambda = 1.00$ and $EGR = 10\%$

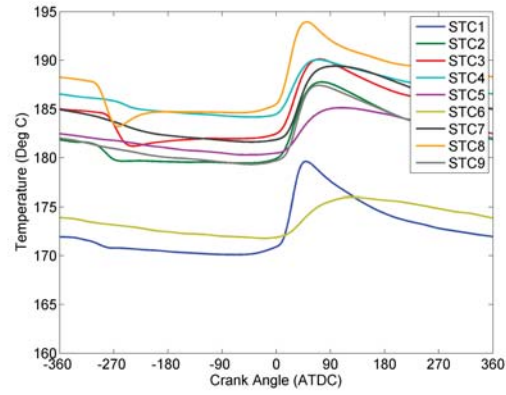


(d) $\lambda = 1.30$ and $EGR = 0\%$

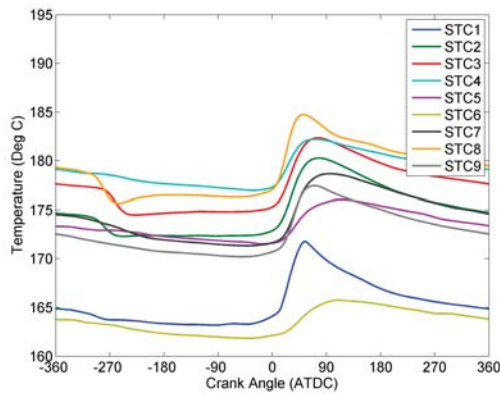


(e) $\lambda = 1.00$ and $EGR = 20\%$

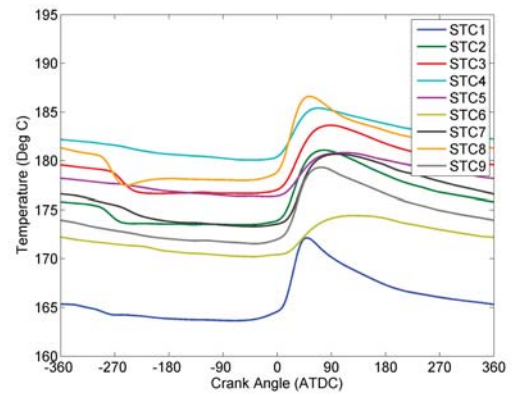
Figure C.3: Piston Temperature Plot for 1500 RPM and 8 bar BMEP



(a) $\lambda = 1.00$ and $EGR = 0\%$

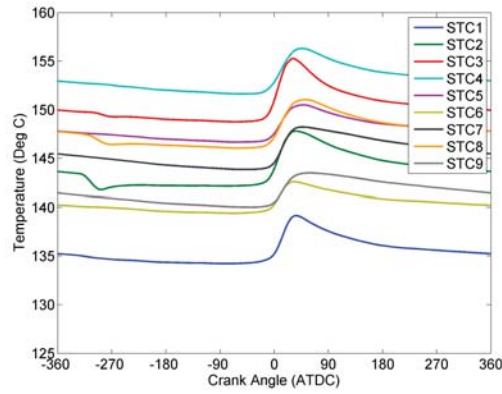


(b) $\lambda = 1.15$ and $EGR = 0\%$

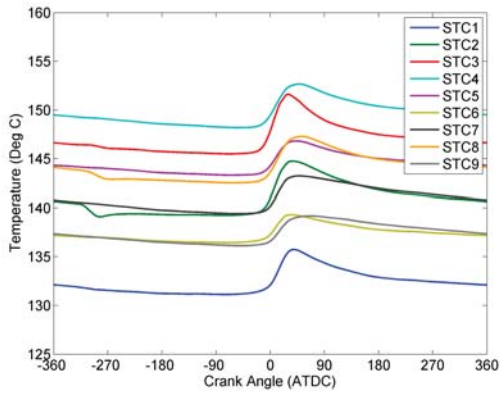


(c) $\lambda = 1.00$ and $EGR = 10\%$

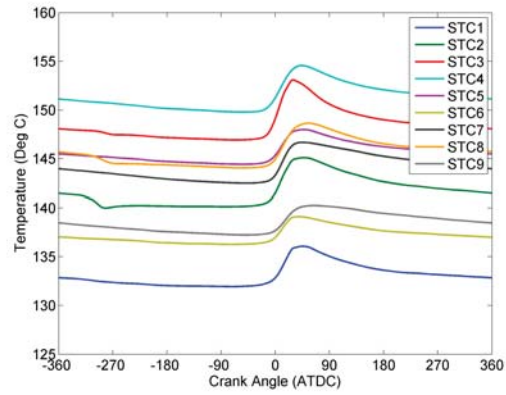
Figure C.4: Piston Temperature Plot for 1500 RPM and 11 bar BMEP



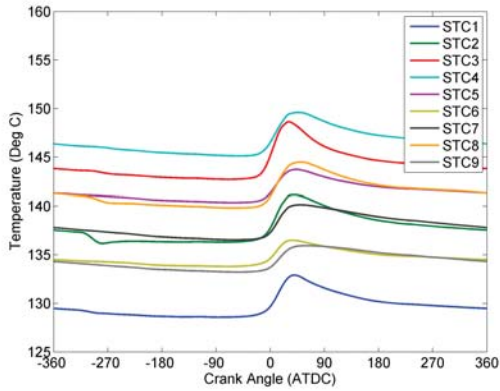
(a) $\lambda = 1.00$ and $EGR = 0\%$



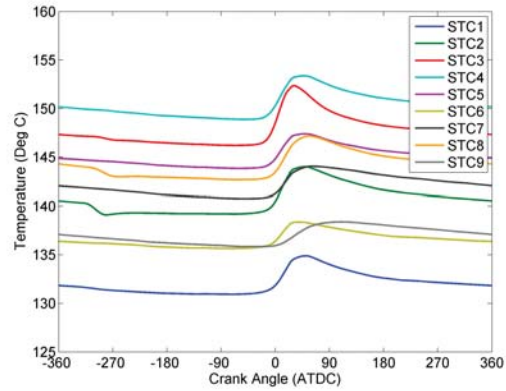
(b) $\lambda = 1.15$ and $EGR = 0\%$



(c) $\lambda = 1.00$ and $EGR = 10\%$

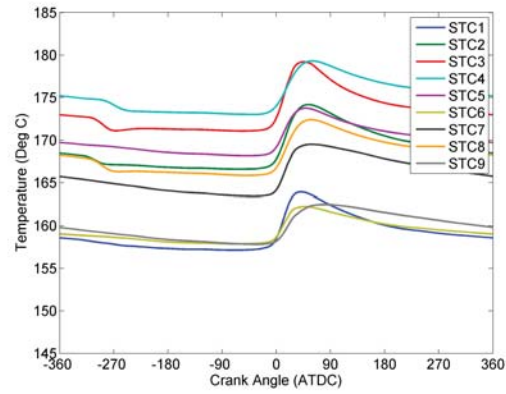


(d) $\lambda = 1.30$ and $EGR = 0\%$

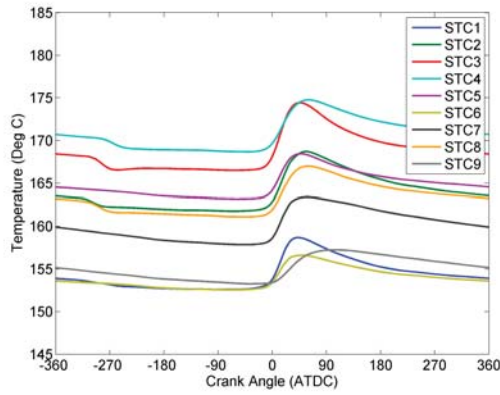


(e) $\lambda = 1.00$ and $EGR = 20\%$

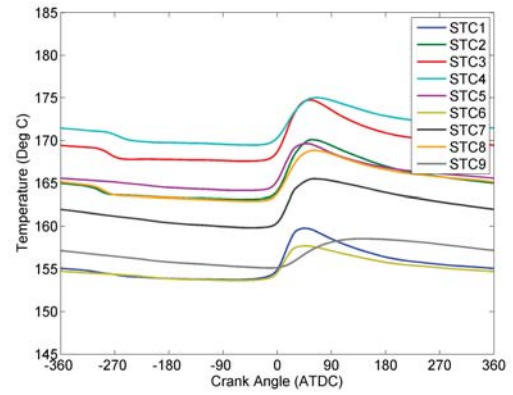
Figure C.5: Piston Temperature Plot for 2250 RPM and 2 bar BMEP



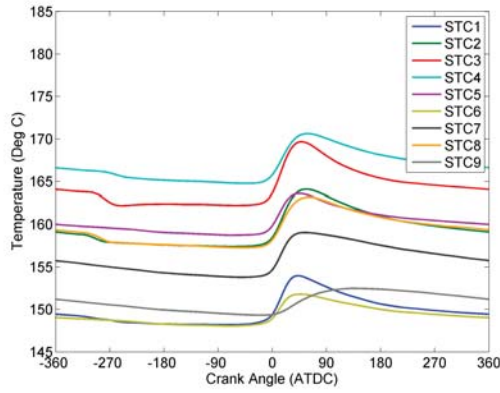
(a) $\lambda = 1.00$ and $EGR = 0\%$



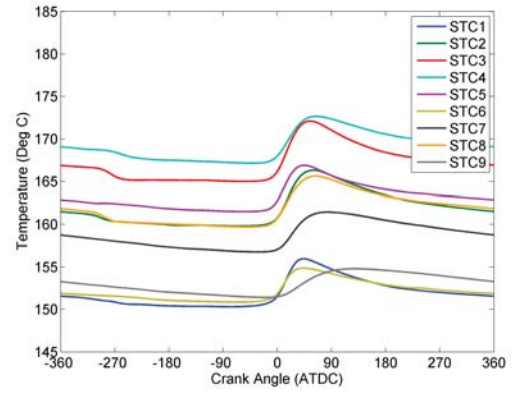
(b) $\lambda = 1.15$ and $EGR = 0\%$



(c) $\lambda = 1.00$ and $EGR = 10\%$

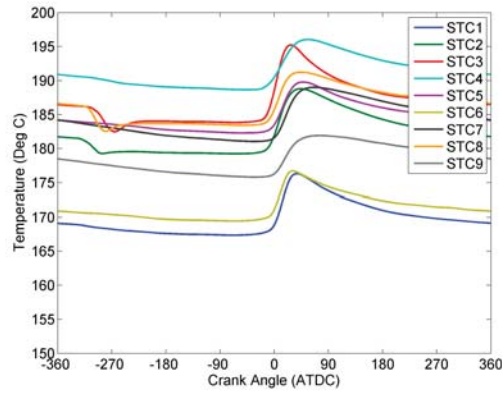


(d) $\lambda = 1.30$ and $EGR = 0\%$

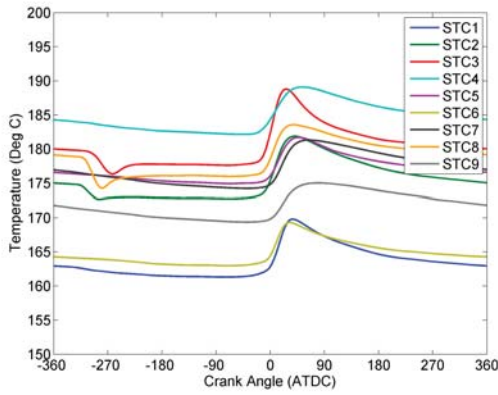


(e) $\lambda = 1.00$ and $EGR = 20\%$

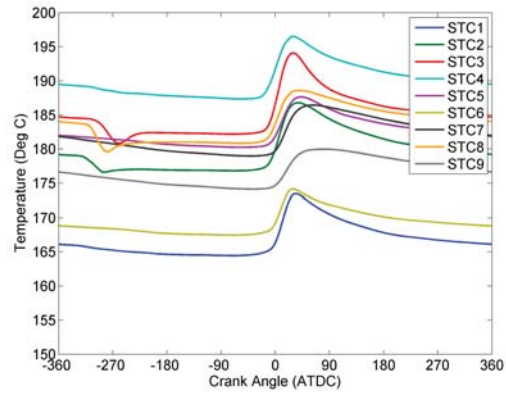
Figure C.6: Piston Temperature Plot for 2250 RPM and 5 bar BMEP



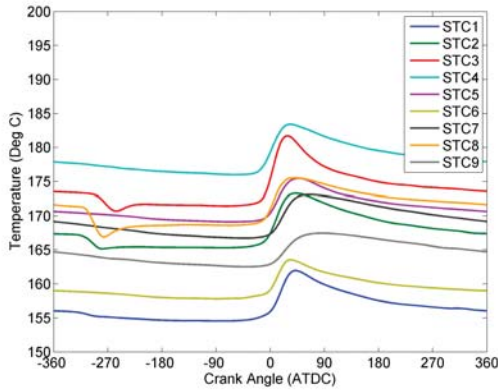
(a) $\lambda = 1.00$ and $EGR = 0\%$



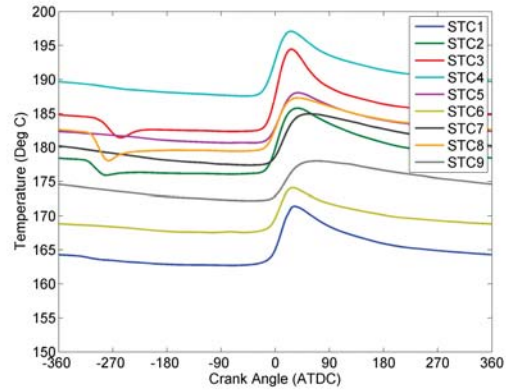
(b) $\lambda = 1.15$ and $EGR = 0\%$



(c) $\lambda = 1.00$ and $EGR = 10\%$

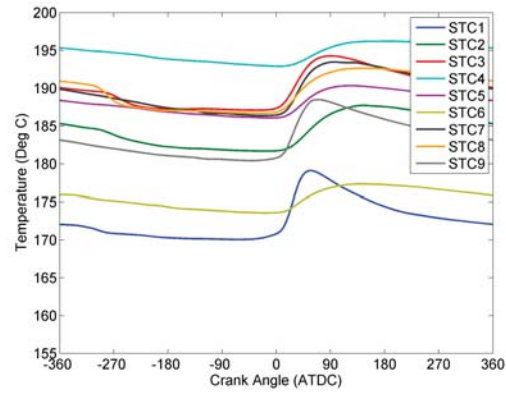


(d) $\lambda = 1.30$ and $EGR = 0\%$

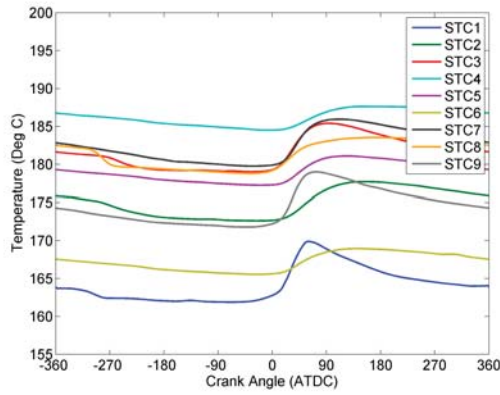


(e) $\lambda = 1.00$ and $EGR = 20\%$

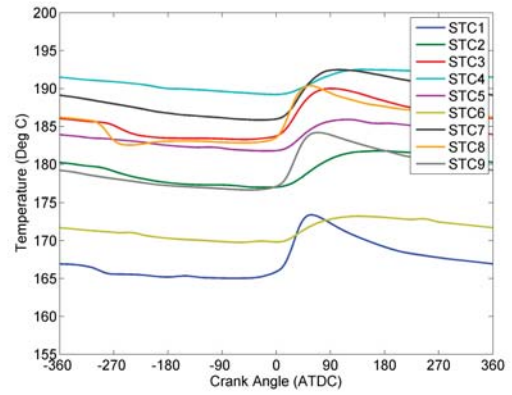
Figure C.7: Piston Temperature Plot for 2250 RPM and 8 bar BMEP



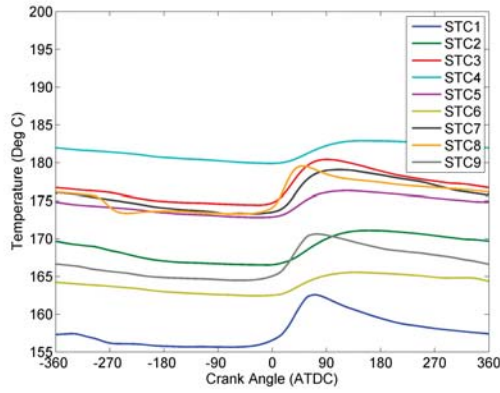
(a) $\lambda = 1.00$ and $EGR = 0\%$



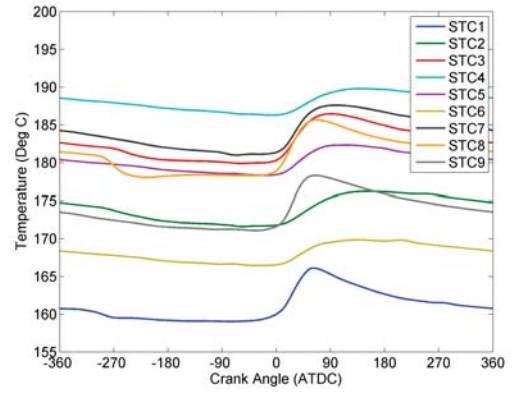
(b) $\lambda = 1.15$ and $EGR = 0\%$



(c) $\lambda = 1.00$ and $EGR = 10\%$

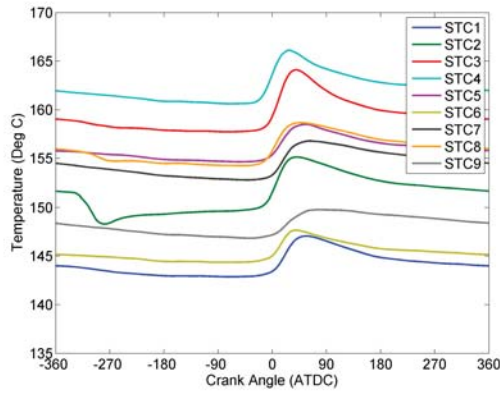


(d) $\lambda = 1.30$ and $EGR = 0\%$

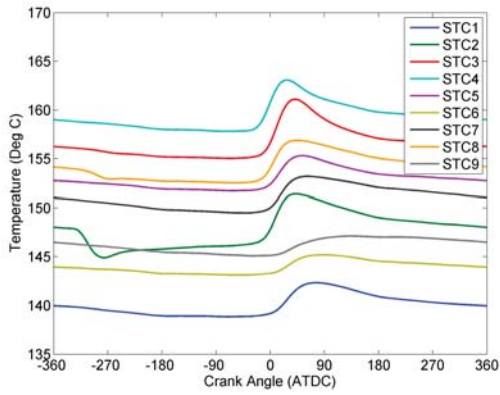


(e) $\lambda = 1.00$ and $EGR = 20\%$

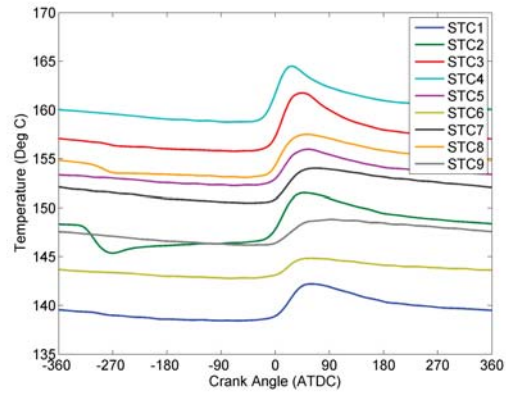
Figure C.8: Piston Temperature Plot for 2250 RPM and 11 bar BMEP



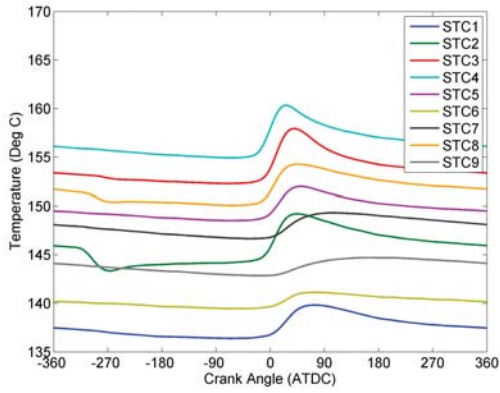
(a) $\lambda = 1.00$ and $EGR = 0\%$



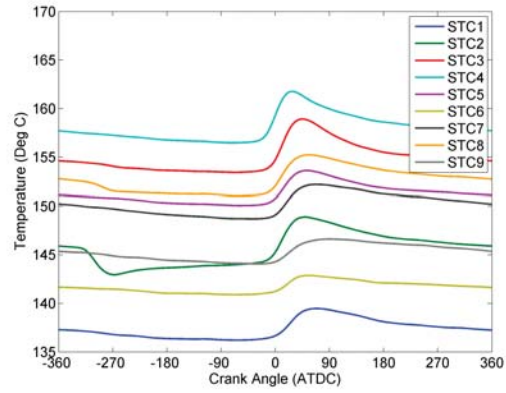
(b) $\lambda = 1.15$ and $EGR = 0\%$



(c) $\lambda = 1.00$ and $EGR = 10\%$

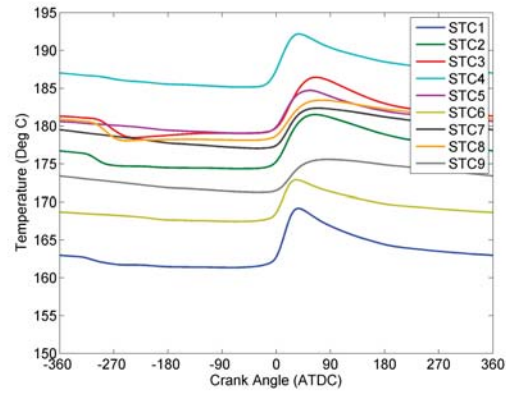


(d) $\lambda = 1.30$ and $EGR = 0\%$

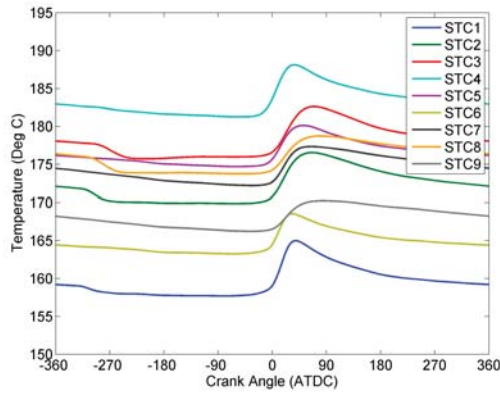


(e) $\lambda = 1.00$ and $EGR = 20\%$

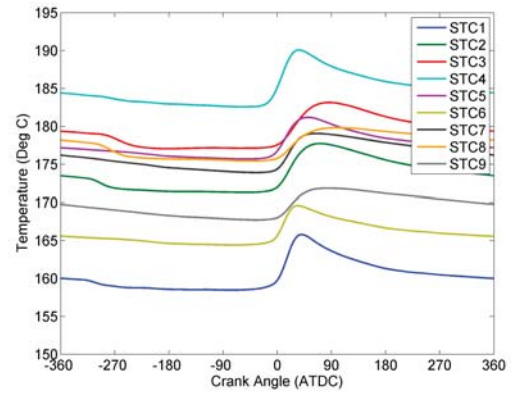
Figure C.9: Piston Temperature Plot for 3000 RPM and 2 bar BMEP



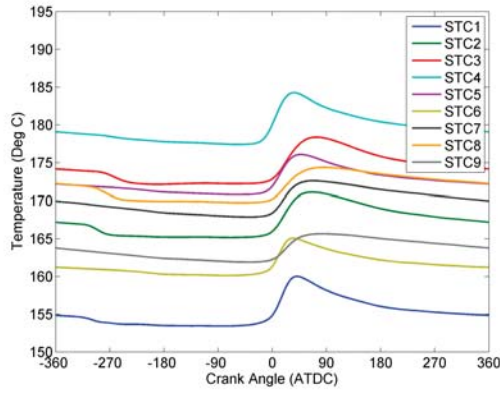
(a) $\lambda = 1.00$ and $EGR = 0\%$



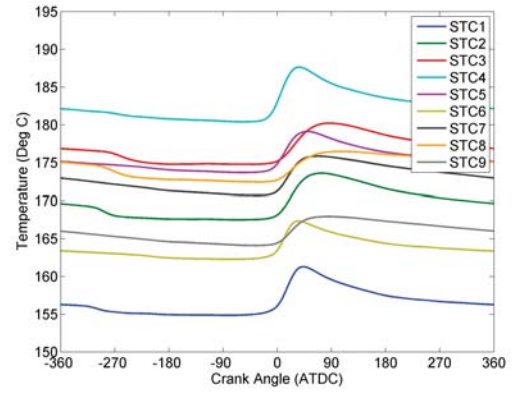
(b) $\lambda = 1.15$ and $EGR = 0\%$



(c) $\lambda = 1.00$ and $EGR = 10\%$

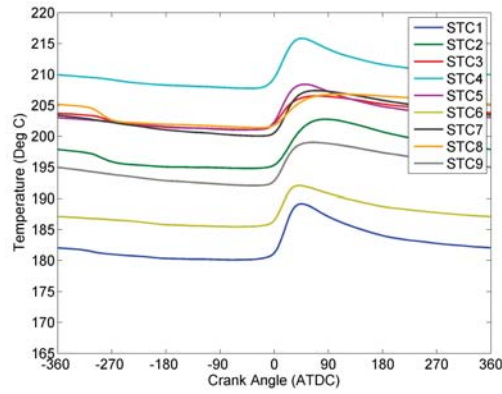


(d) $\lambda = 1.30$ and $EGR = 0\%$

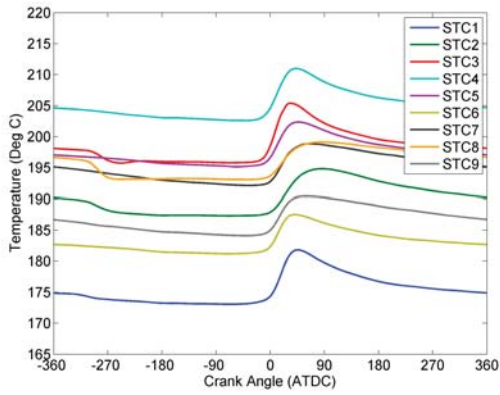


(e) $\lambda = 1.00$ and $EGR = 20\%$

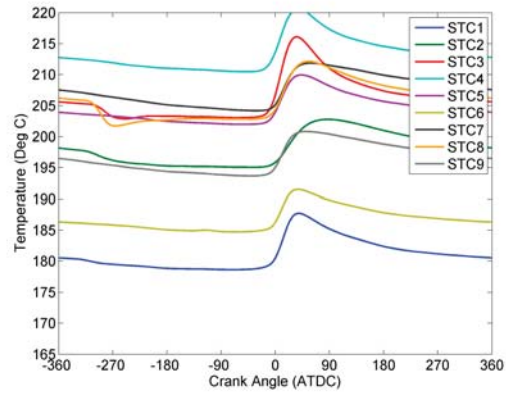
Figure C.10: Piston Temperature Plot for 3000 RPM and 5 bar BMEP



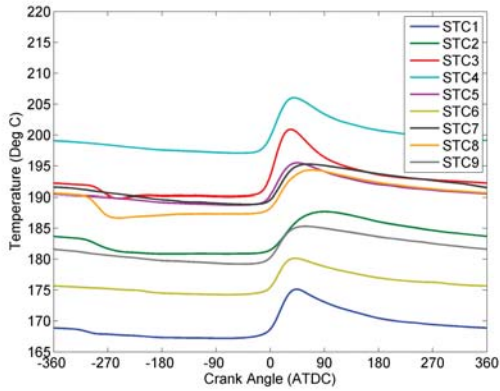
(a) $\lambda = 1.00$ and $EGR = 0\%$



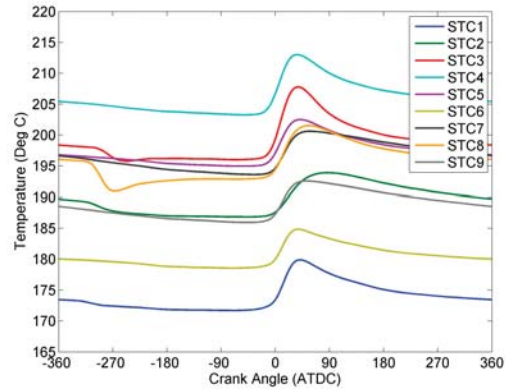
(b) $\lambda = 1.15$ and $EGR = 0\%$



(c) $\lambda = 1.00$ and $EGR = 10\%$

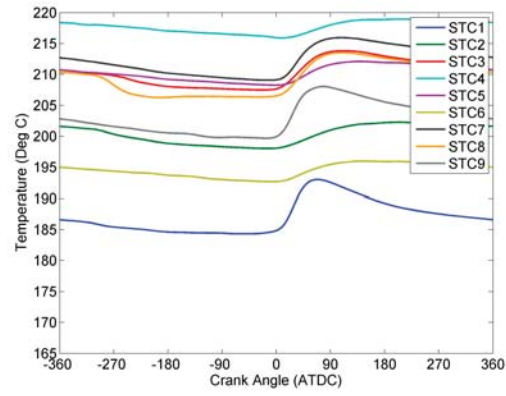


(d) $\lambda = 1.30$ and $EGR = 0\%$

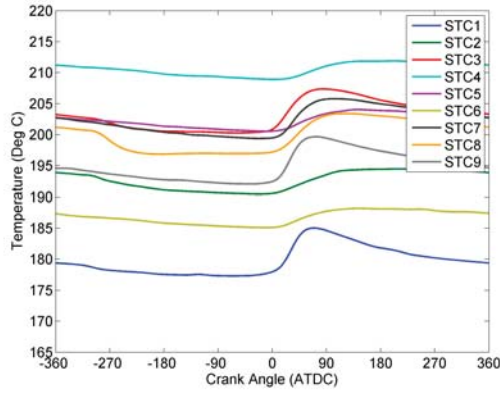


(e) $\lambda = 1.00$ and $EGR = 20\%$

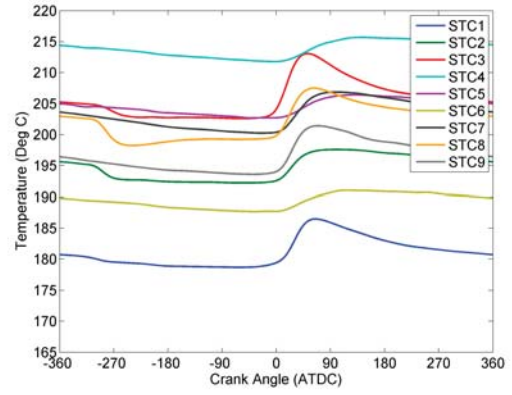
Figure C.11: Piston Temperature Plot for 3000 RPM and 8 bar BMEP



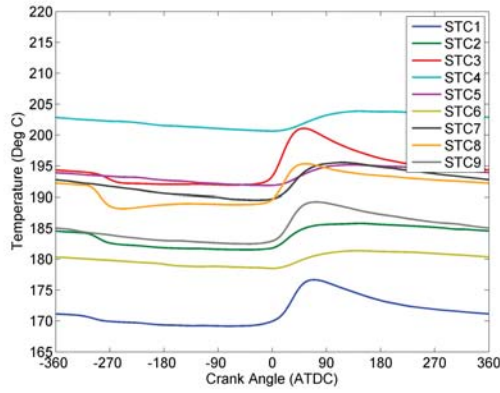
(a) $\lambda = 1.00$ and $EGR = 0\%$



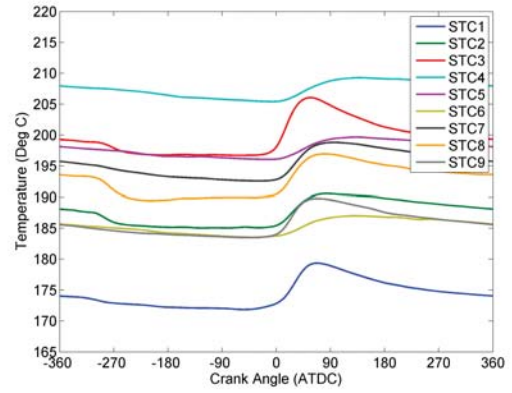
(b) $\lambda = 1.15$ and $EGR = 0\%$



(c) $\lambda = 1.00$ and $EGR = 10\%$



(d) $\lambda = 1.30$ and $EGR = 0\%$



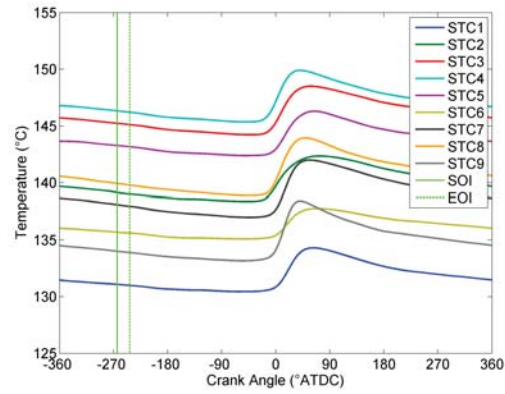
(e) $\lambda = 1.00$ and $EGR = 20\%$

Figure C.12: Piston Temperature Plot for 3000 RPM and 11 bar BMEP

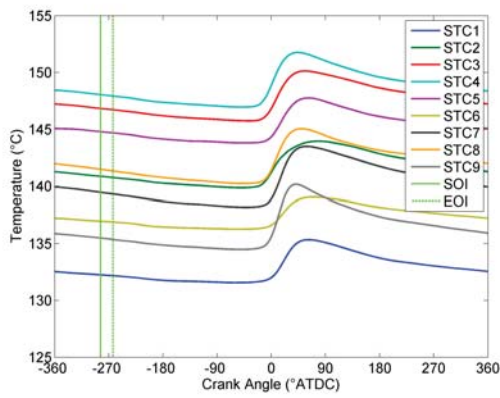
Appendix D

Additional Impingement Identification Plots¹

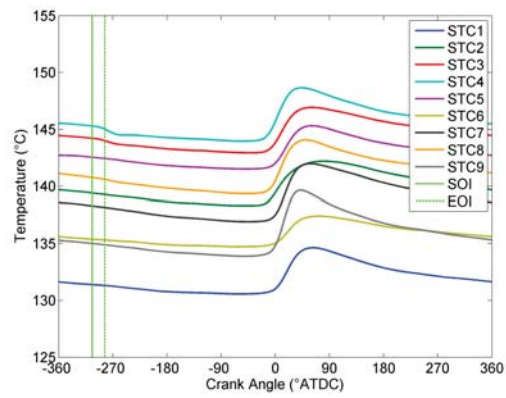
¹The material contained in this chapter is planned for submission as part of a journal article and/or conference paper in the future.



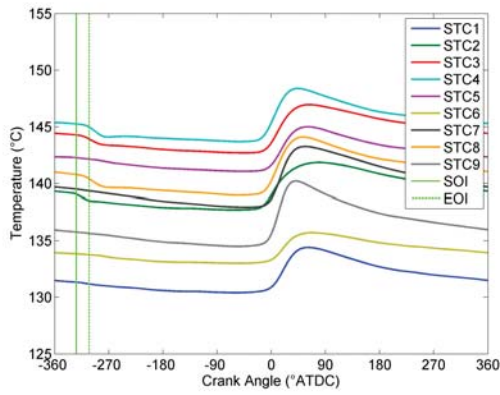
(a) -260° ATDC



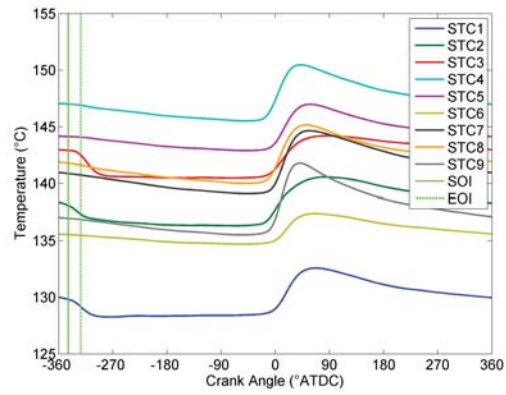
(b) -280° ATDC



(c) -300° ATDC

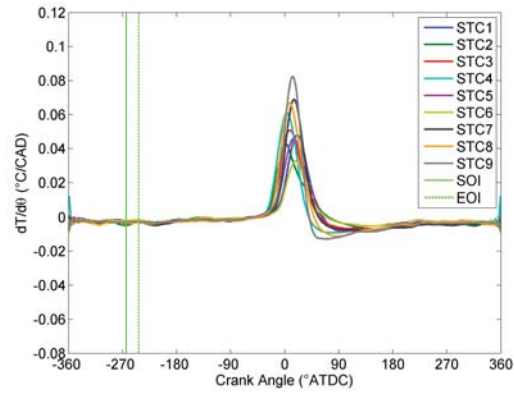


(d) -320° ATDC

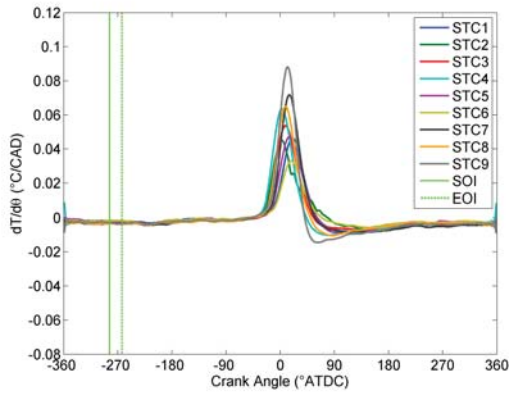


(e) -340° ATDC

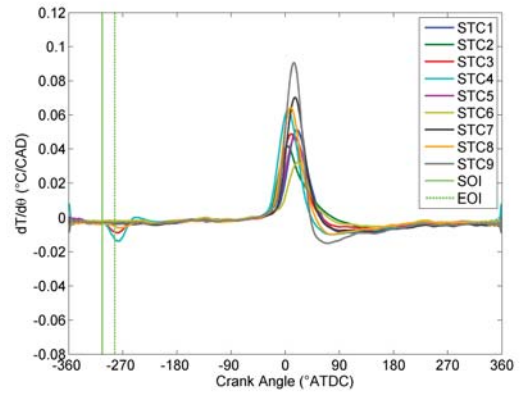
Figure D.1: SOI Sweep STC Results at 1500 RPM and 2.6 bar BMEP



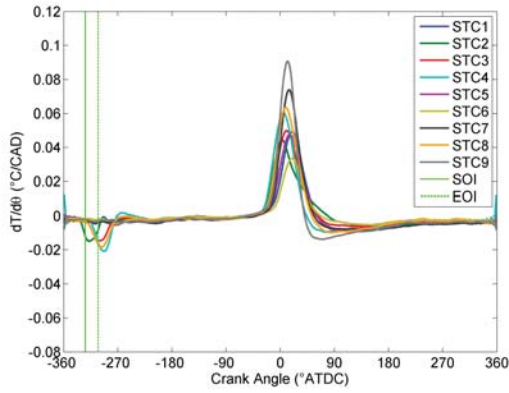
(a) -260° ATDC



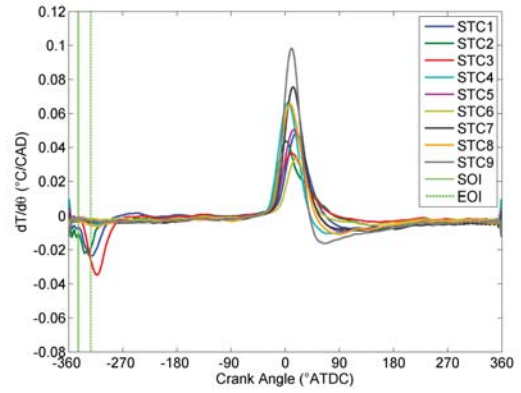
(b) -280° ATDC



(c) -300° ATDC

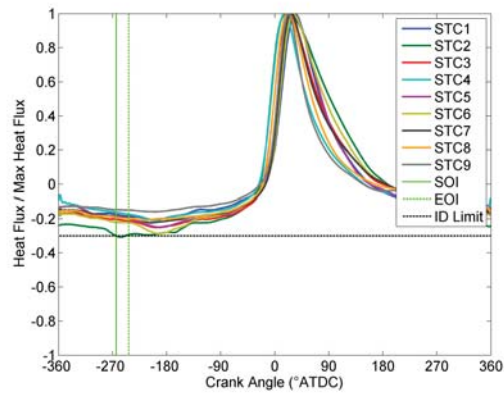


(d) -320° ATDC

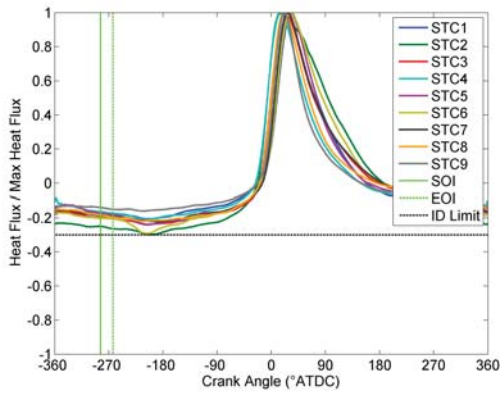


(e) -340° ATDC

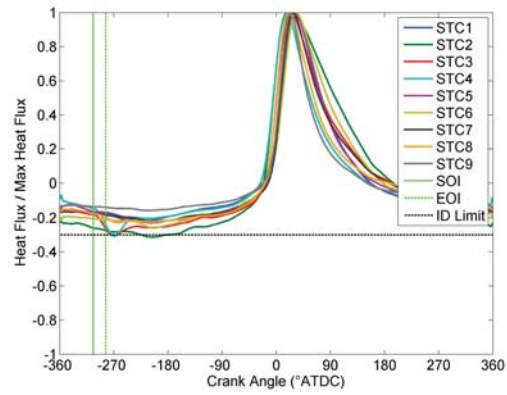
Figure D.2: SOI Sweep $dT/d\theta$ Results at 1500 RPM and 2.6 bar BMEP



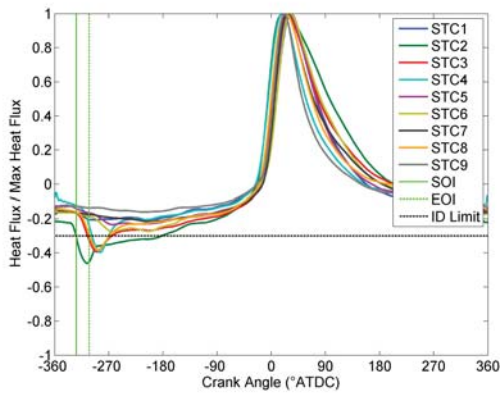
(a) -260° ATDC



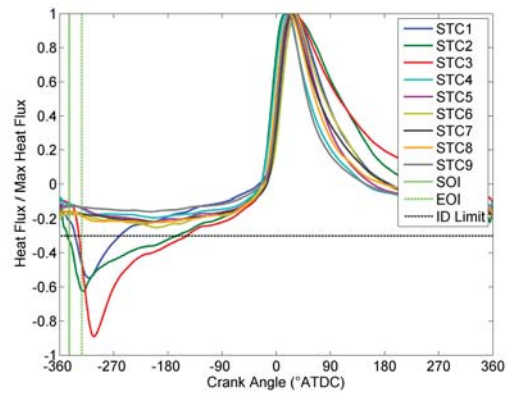
(b) -280° ATDC



(c) -300° ATDC

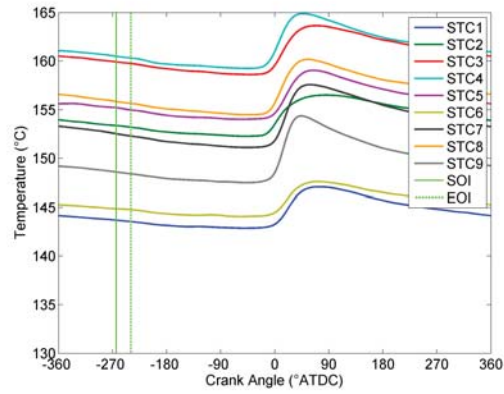


(d) -320° ATDC

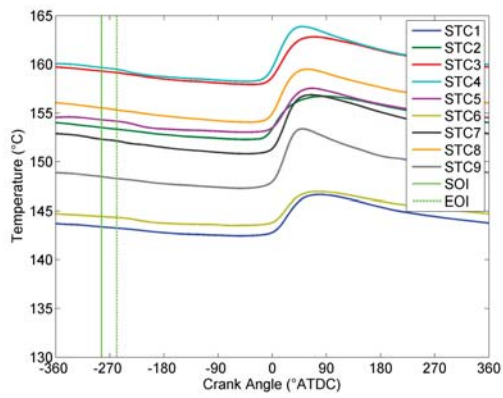


(e) -340° ATDC

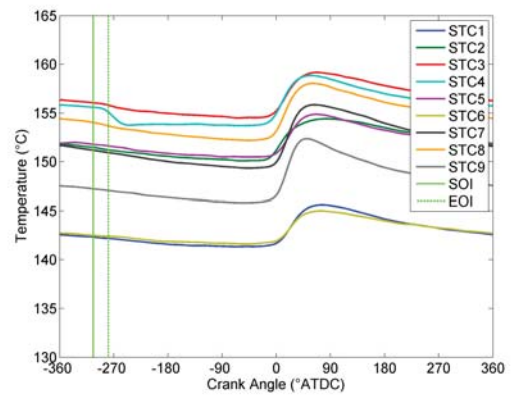
Figure D.3: SOI Sweep Normalized Heat Flux Results at 1500 RPM and 2.6 bar BMEP



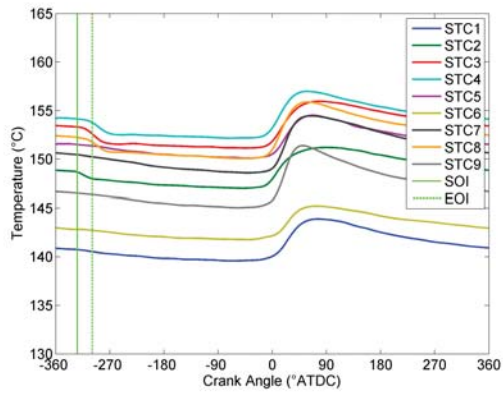
(a) -260° ATDC



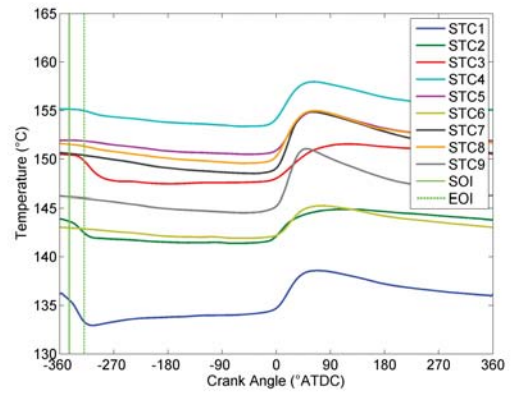
(b) -280° ATDC



(c) -300° ATDC

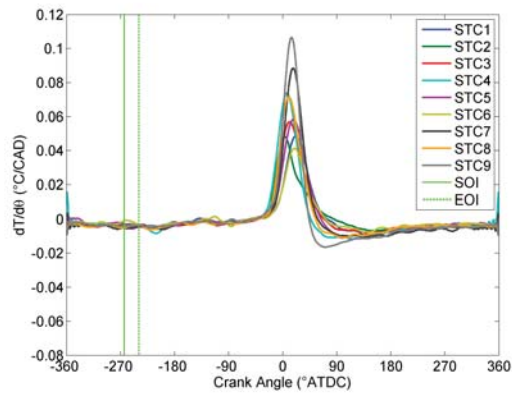


(d) -320° ATDC

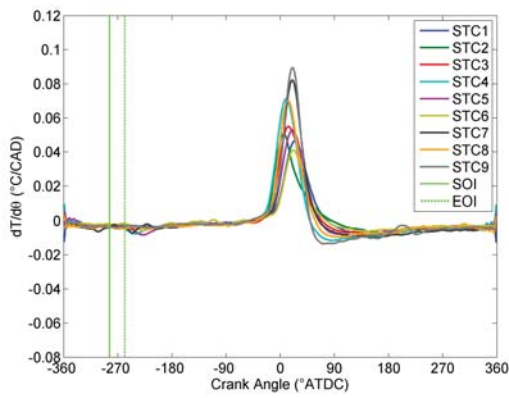


(e) -340° ATDC

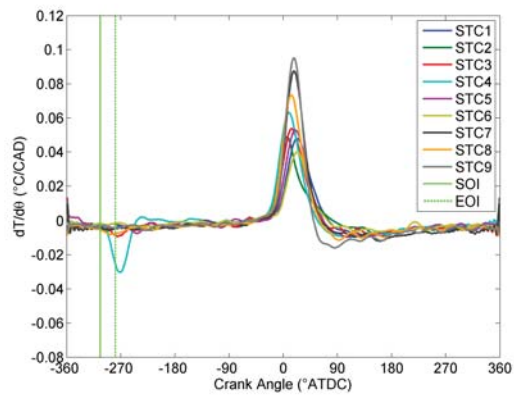
Figure D.4: SOI Sweep STC Results at 1500 RPM and 5 bar BMEP



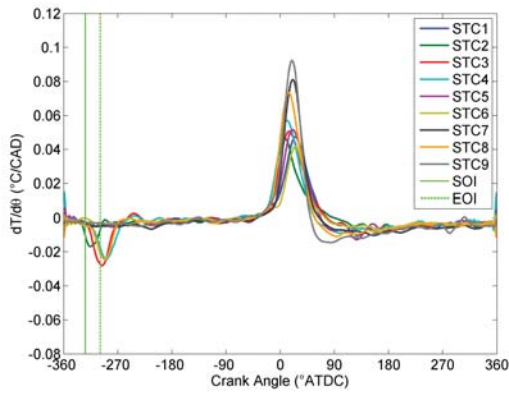
(a) -260° ATDC



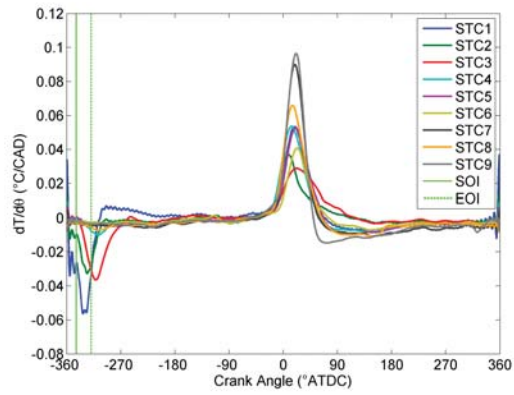
(b) -280° ATDC



(c) -300° ATDC

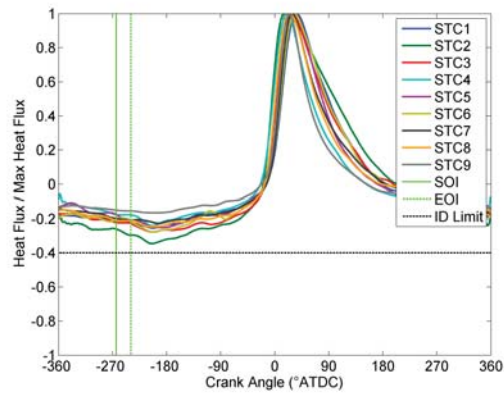


(d) -320° ATDC

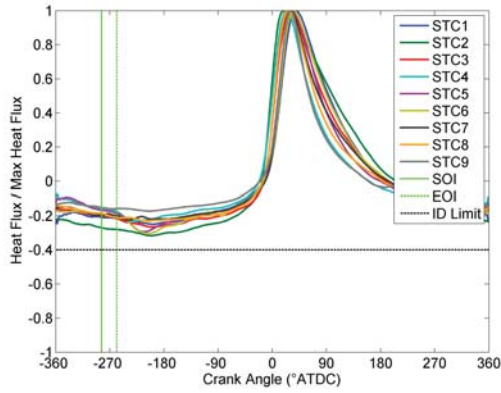


(e) -340° ATDC

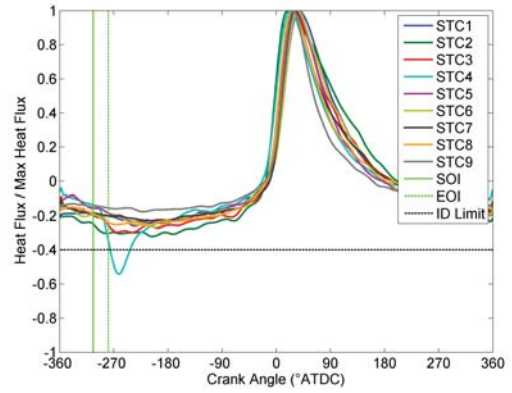
Figure D.5: SOI Sweep $dT/d\theta$ Results at 1500 RPM and 5 bar BMEP



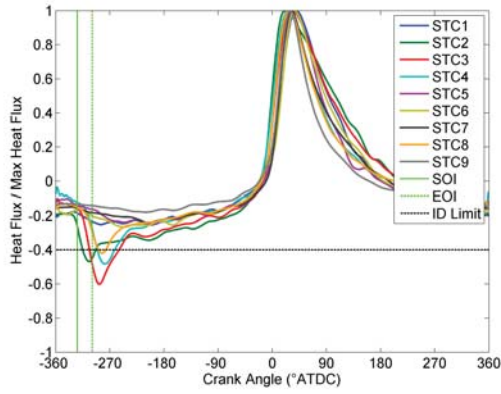
(a) -260° ATDC



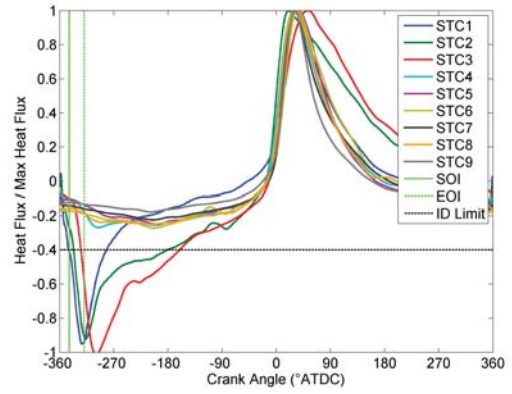
(b) -280° ATDC



(c) -300° ATDC

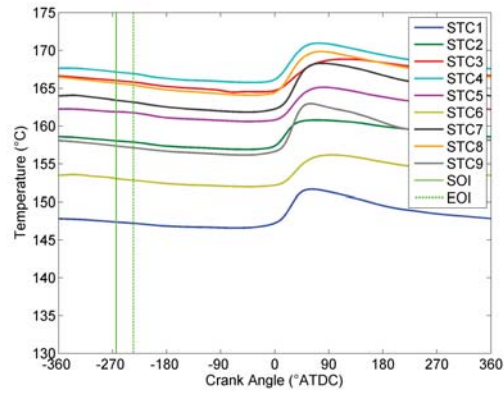


(d) -320° ATDC

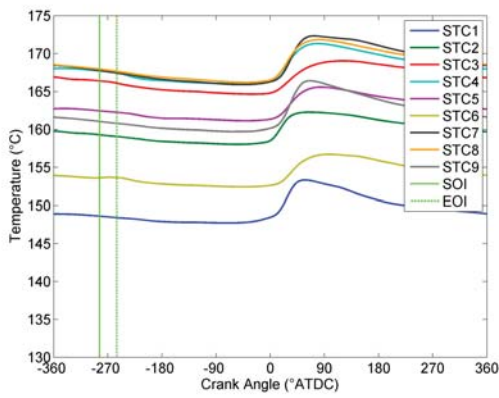


(e) -340° ATDC

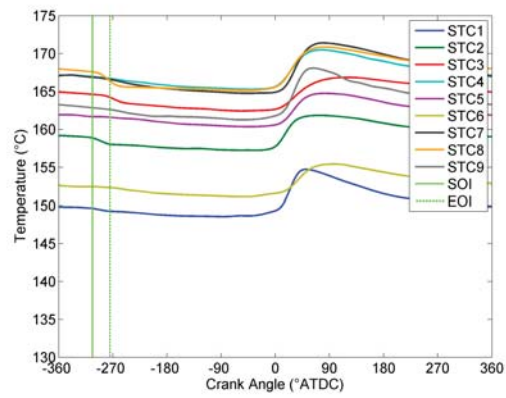
Figure D.6: SOI Sweep Normalized Heat Flux Results at 1500 RPM and 5 bar BMEP



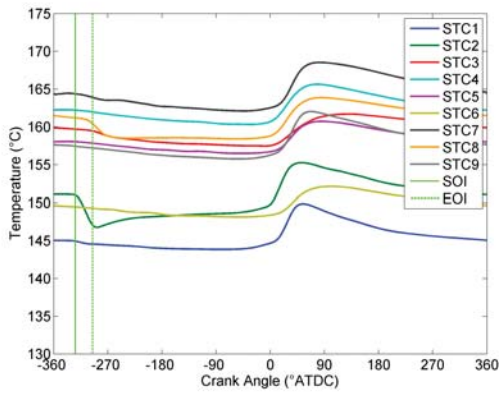
(a) -260° ATDC



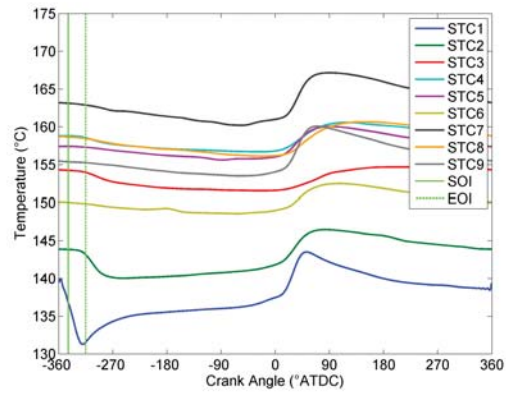
(b) -280° ATDC



(c) -300° ATDC

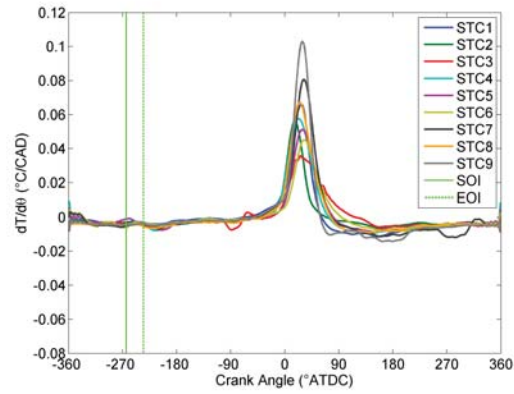


(d) -320° ATDC

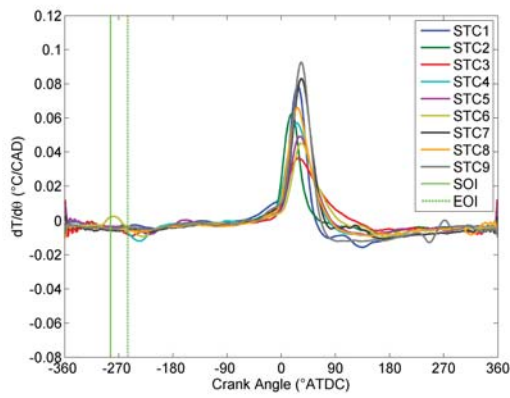


(e) -340° ATDC

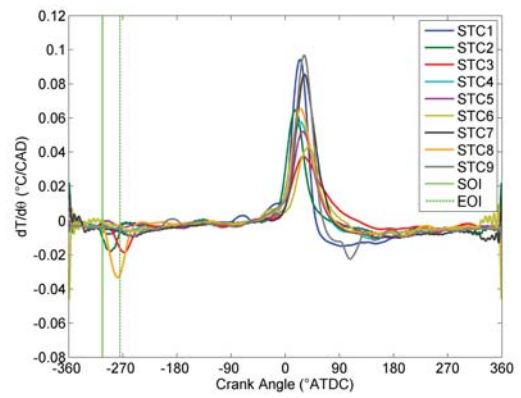
Figure D.7: SOI Sweep STC Results at 1500 RPM and 8 bar BMEP



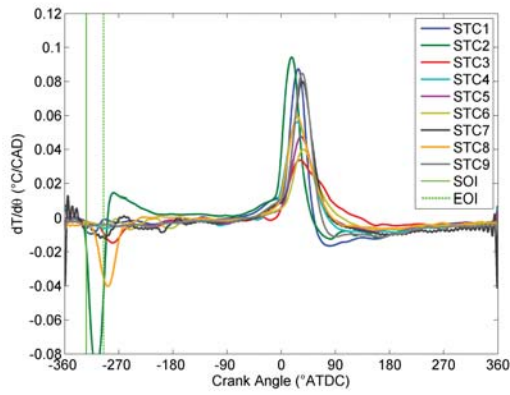
(a) -260° ATDC



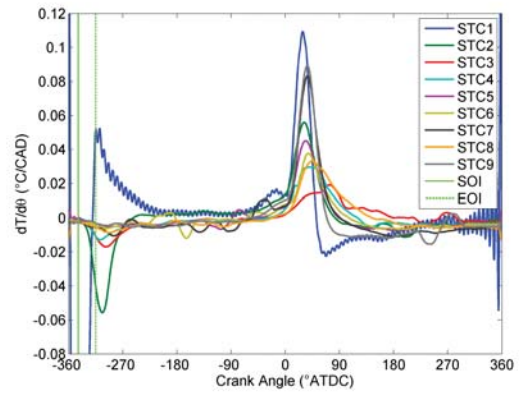
(b) -280° ATDC



(c) -300° ATDC

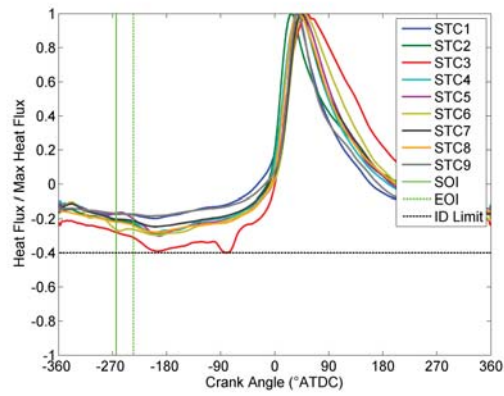


(d) -320° ATDC

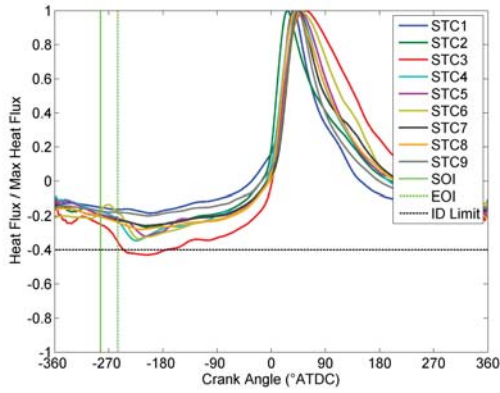


(e) -340° ATDC

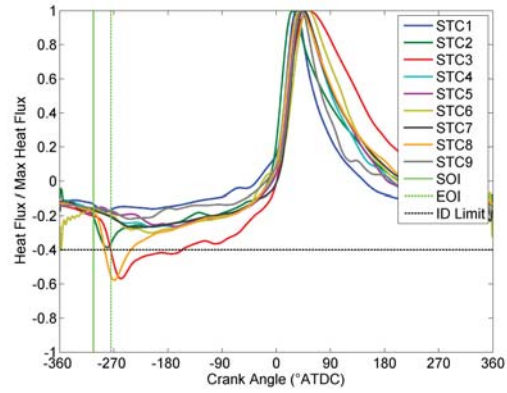
Figure D.8: SOI Sweep $dT/d\theta$ Results at 1500 RPM and 8 bar BMEP



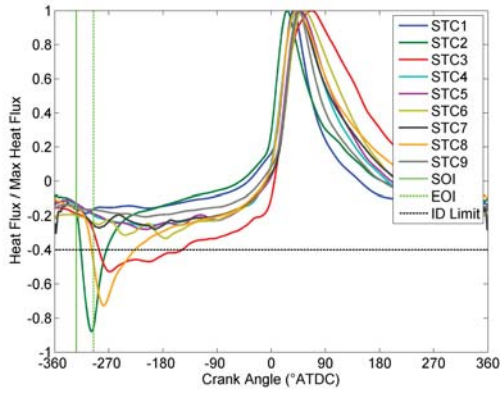
(a) -260° ATDC



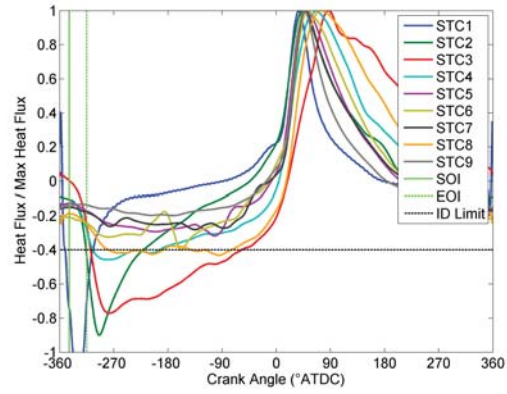
(b) -280° ATDC



(c) -300° ATDC

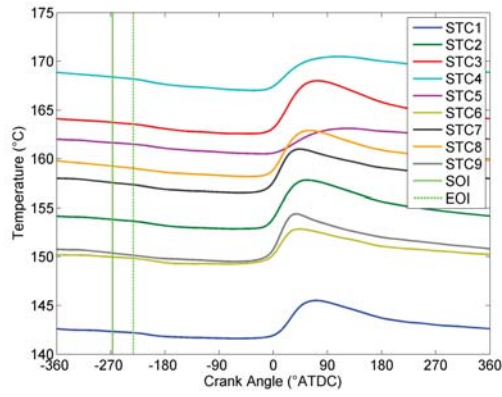


(d) -320° ATDC

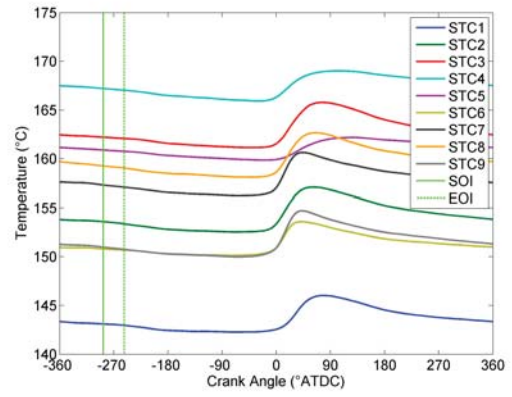


(e) -340° ATDC

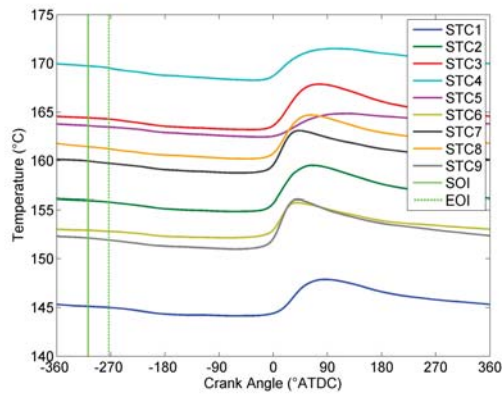
Figure D.9: SOI Sweep Normalized Heat Flux Results at 1500 RPM and 8 bar BMEP



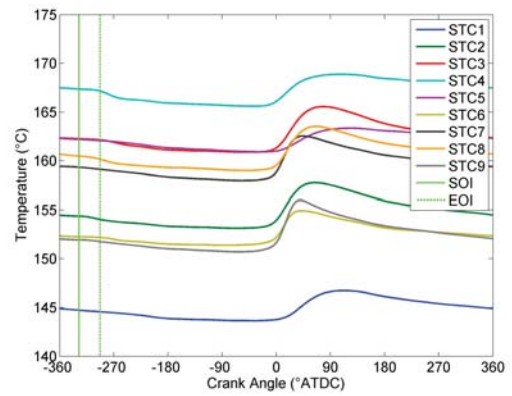
(a) -260° ATDC



(b) -280° ATDC

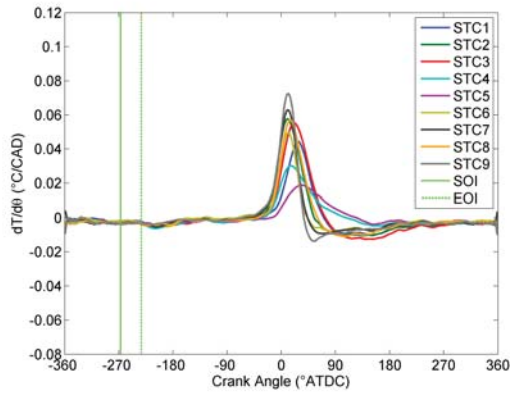


(c) -300° ATDC

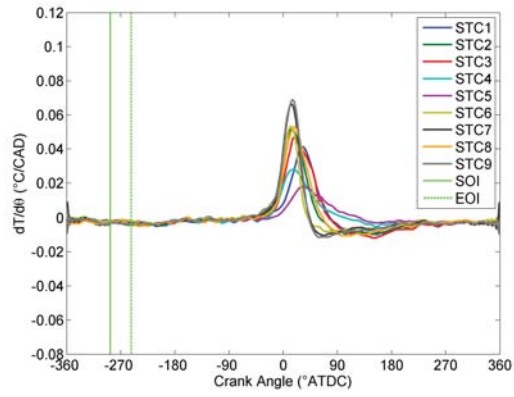


(d) -320° ATDC

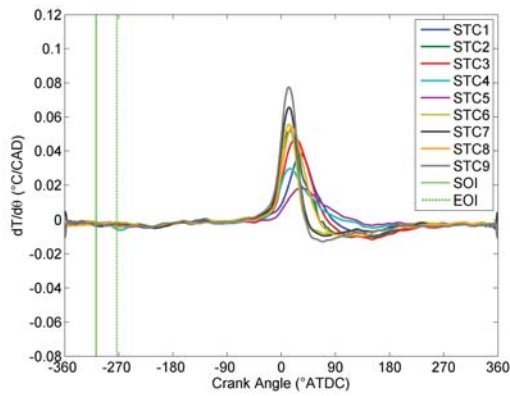
Figure D.10: SOI Sweep STC Results at 3000 RPM and 2.6 bar BMEP



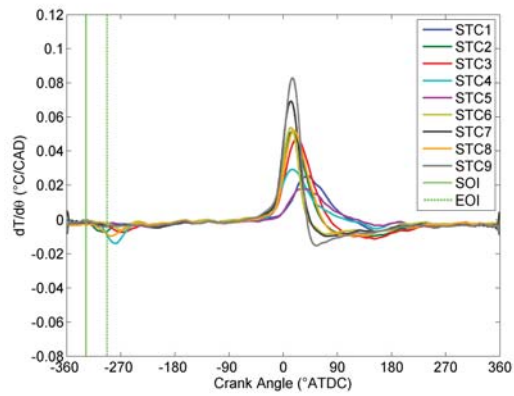
(a) -260° ATDC



(b) -280° ATDC

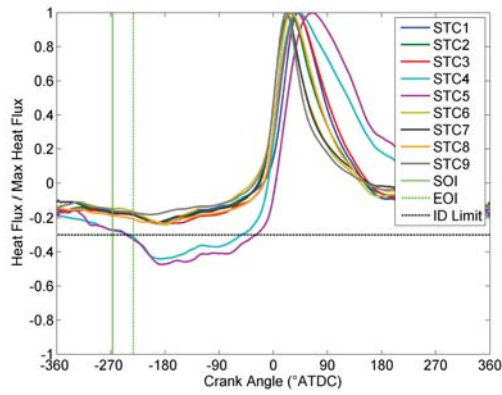


(c) -300° ATDC

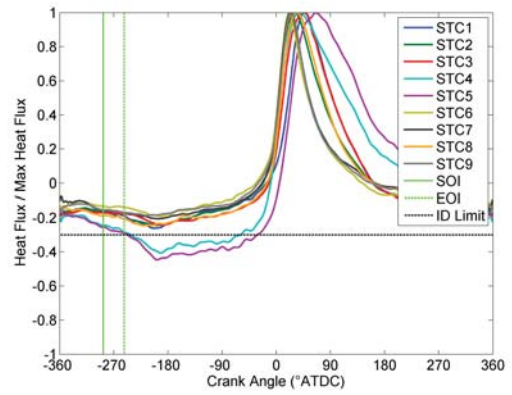


(d) -320° ATDC

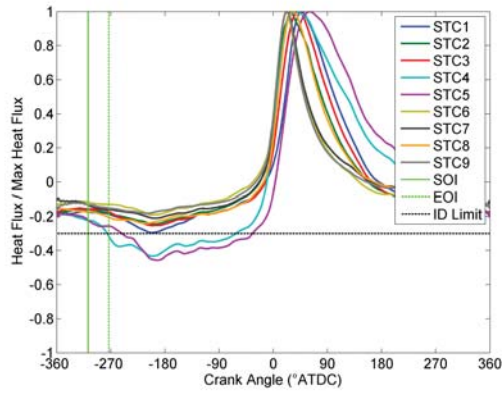
Figure D.11: SOI Sweep $dT/d\theta$ Results at 3000 RPM and 2.6 bar BMEP



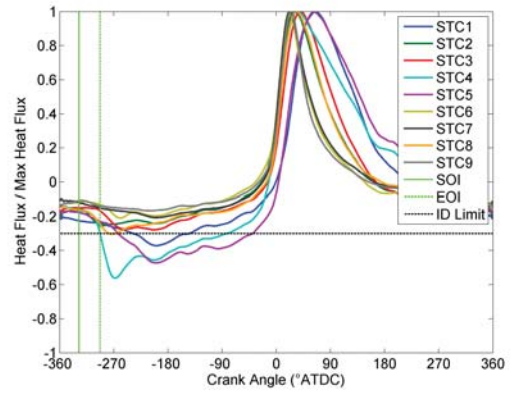
(a) -260° ATDC



(b) -280° ATDC

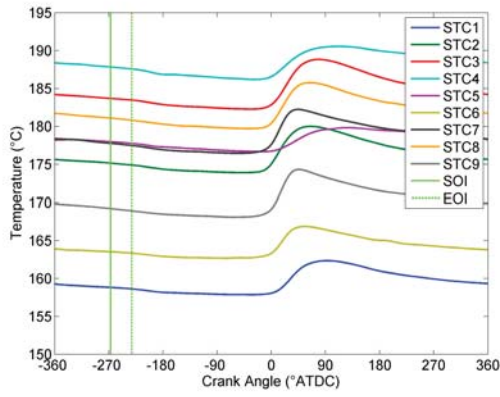


(c) -300° ATDC

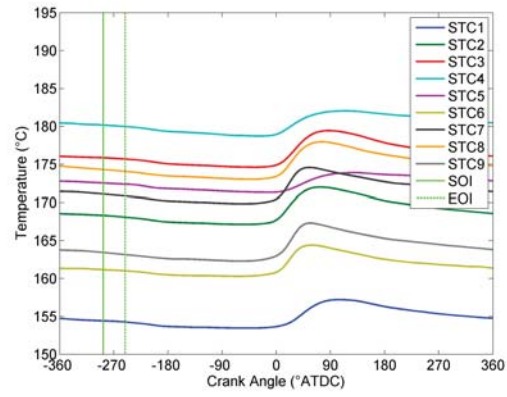


(d) -320° ATDC

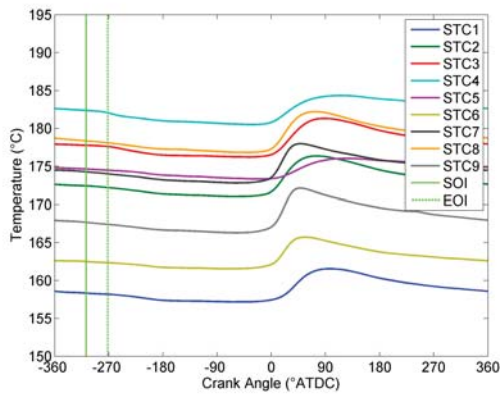
Figure D.12: SOI Sweep Normalized Heat Flux Results at 3000 RPM and 2.6 bar BMEP



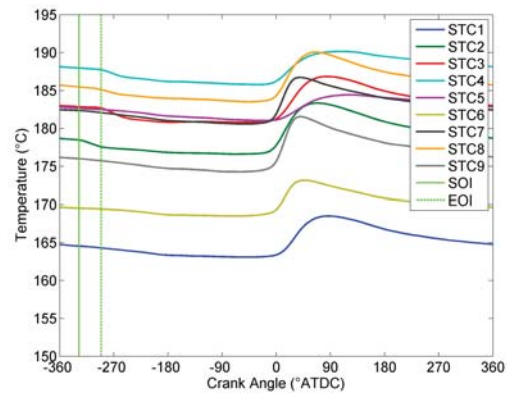
(a) -260° ATDC



(b) -280° ATDC

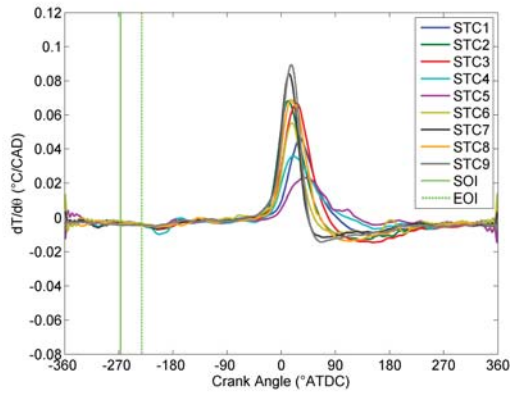


(c) -300° ATDC

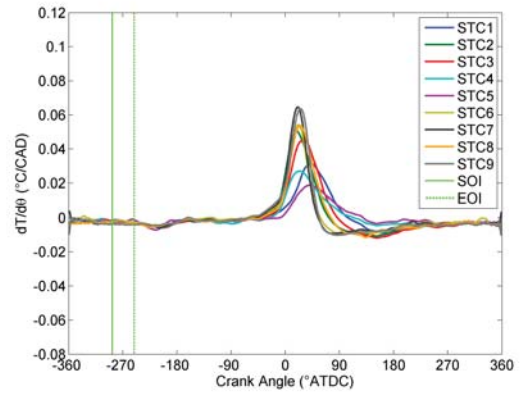


(d) -320° ATDC

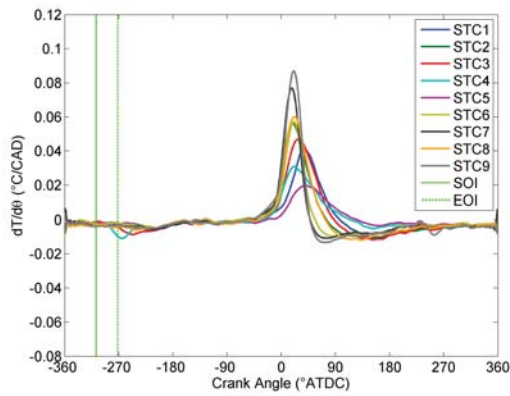
Figure D.13: SOI Sweep STC Results at 3000 RPM and 5 bar BMEP



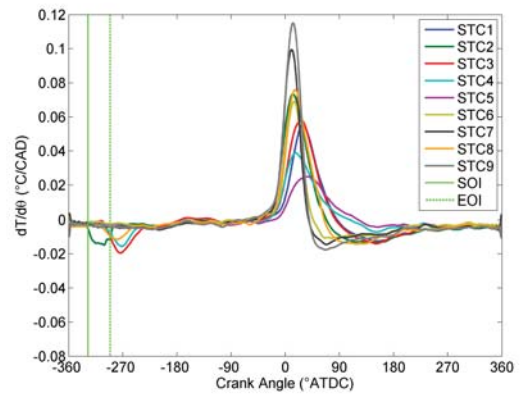
(a) -260° ATDC



(b) -280° ATDC

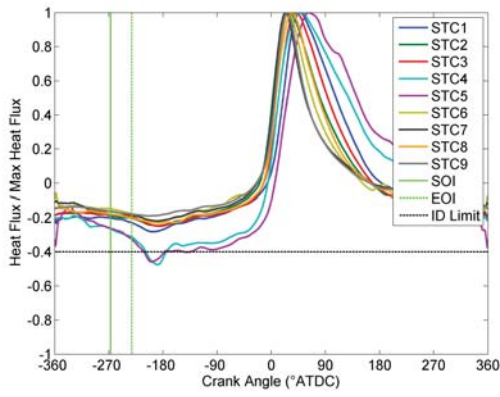


(c) -300° ATDC

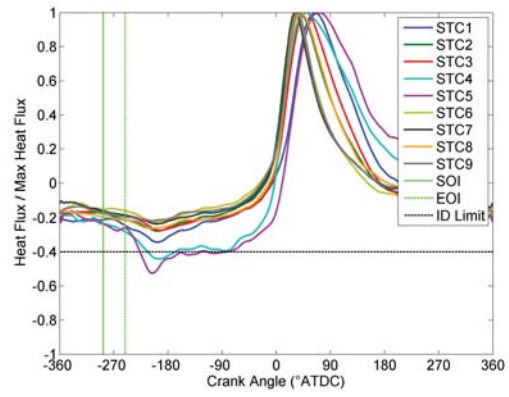


(d) -320° ATDC

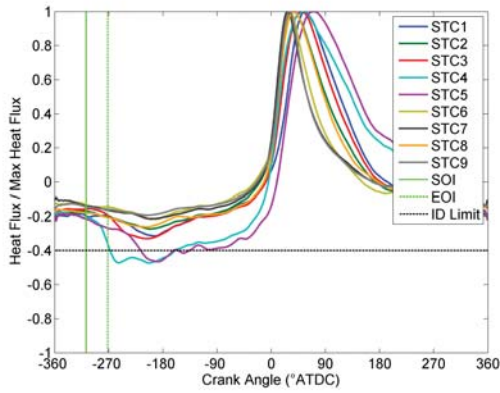
Figure D.14: SOI Sweep $dT/d\theta$ Results at 3000 RPM and 5 bar BMEP



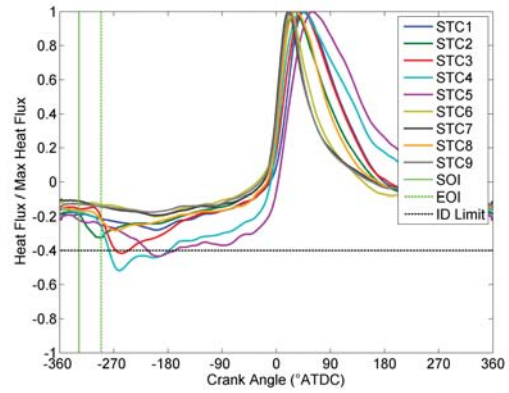
(a) -260° ATDC



(b) -280° ATDC

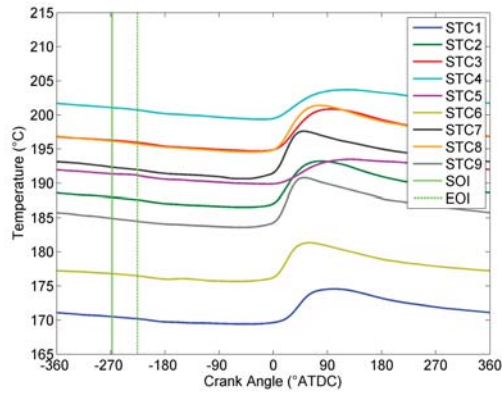


(c) -300° ATDC

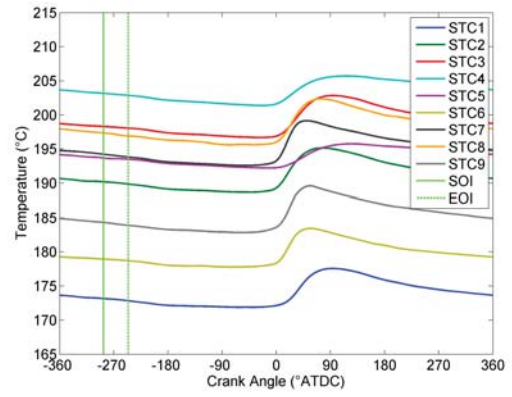


(d) -320° ATDC

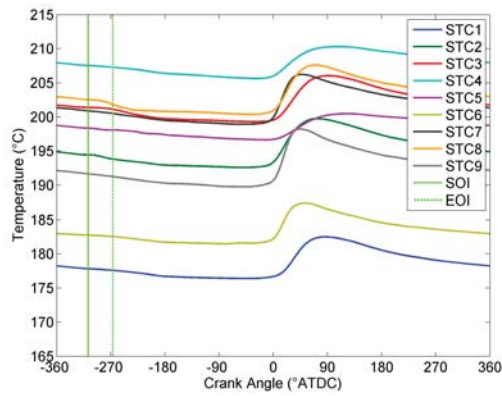
Figure D.15: SOI Sweep Normalized Heat Flux Results at 3000 RPM and 5 bar BMEP



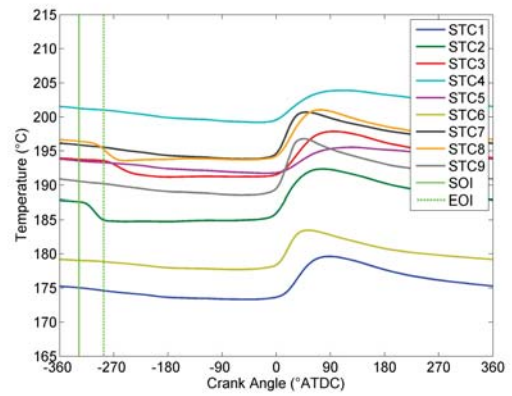
(a) -260° ATDC



(b) -280° ATDC

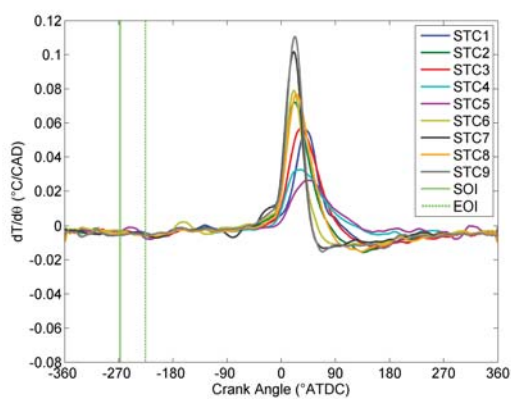


(c) -300° ATDC

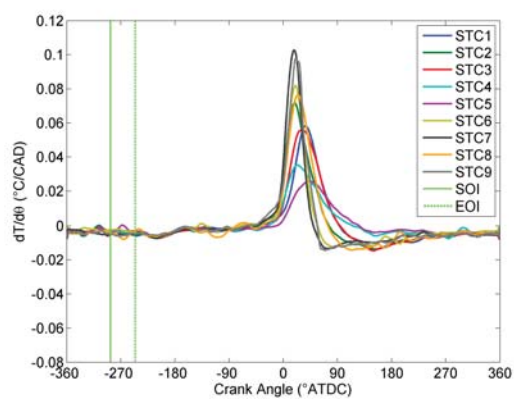


(d) -320° ATDC

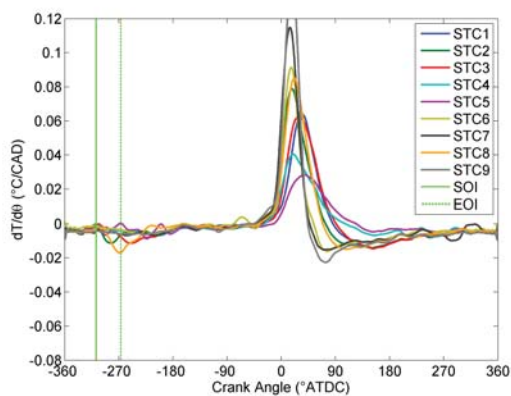
Figure D.16: SOI Sweep STC Results at 3000 RPM and 8 bar BMEP



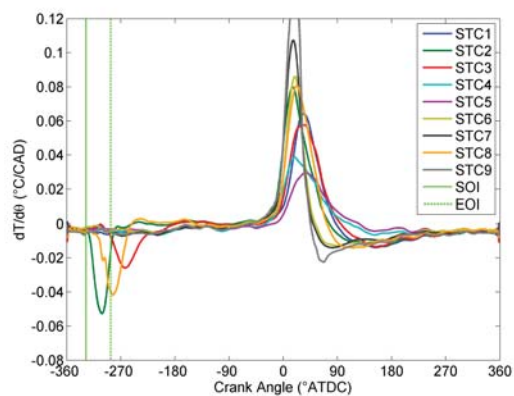
(a) -260° ATDC



(b) -280° ATDC

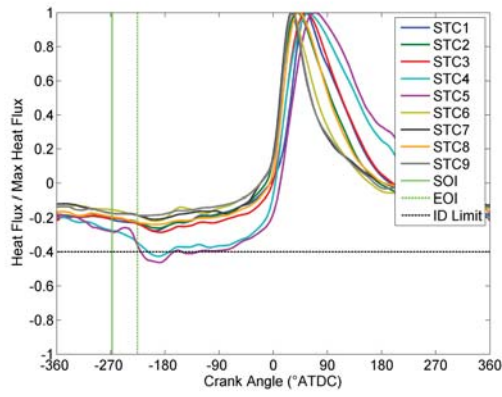


(c) -300° ATDC

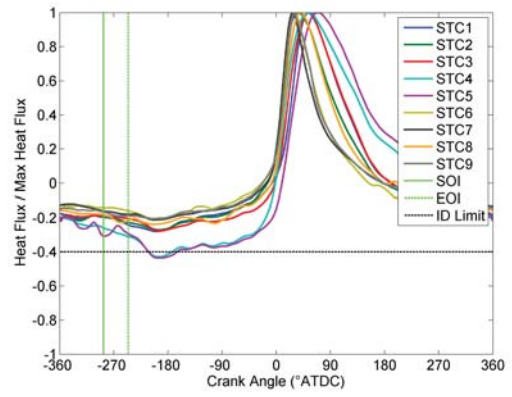


(d) -320° ATDC

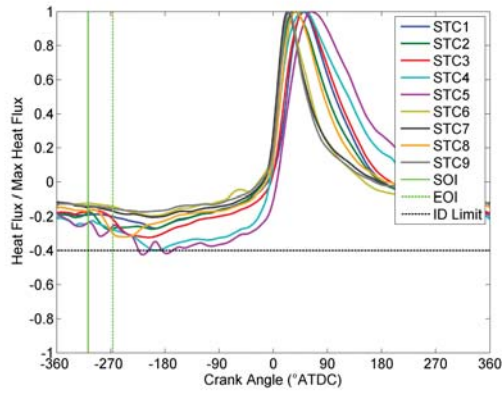
Figure D.17: SOI Sweep $dT/d\theta$ Results at 3000 RPM and 8 bar BMEP



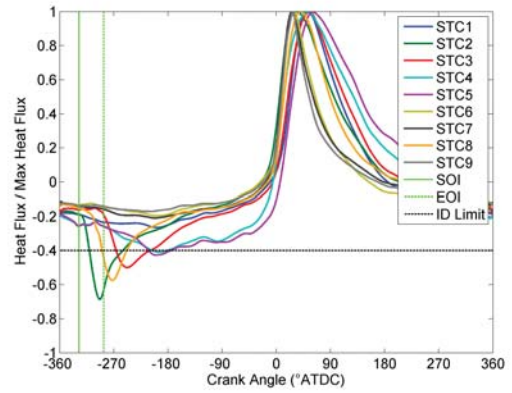
(a) -260° ATDC



(b) -280° ATDC



(c) -300° ATDC



(d) -320° ATDC

Figure D.18: SOI Sweep Normalized Heat Flux Results at 3000 RPM and 8 bar BMEP

Appendix E

Letters of Permission

Permission for Fig. 2.1



Daniel Madison <dpm5049@gmail.com>

to Maria ▾

Hello Maria,

I need to obtain your permission to use the Templug diagram that I used in my MS report in my PhD Dissertation.

Thanks,
Dan



Maria Romero <mariar@testing-engineers.com>

to me ▾

Yes feel free to use the diagram.

Maria Romero-Williams

[510-835-3142 ext. 177](tel:510-835-3142)

Testing Engineers, Inc.

Email: mariar@testing-engineers.com

Permission for Fig. 2.2

MEDTHERM Corporation

3:51 PM (22 minutes ago) ☆

to me

-
Dan

You have our permission to use the diagram of a coaxial thermocouple found in Medtherm Bulletin 500 in your MS report and PhD dissertation.

Best regards,
MEDTHERM Corporation
Larry Jones
President

MEDTHERM Corporation
Post Office Box 412
Huntsville, AL 35804
Telephone: [256-837-2000](tel:256-837-2000)
Fax: [256-837-2001](tel:256-837-2001)
email: medtherm@comcast.net

Street address: 2604 Newby Road
Huntsville, AL 35805

Permission for Fig. 2.5

Daniel Madison <dpmadiso@mtu.edu>

to Daniel

Nov 1

I need permission to use the same figure in my PhD Dissertation this time.

Title: THERMAL CHARACTERIZATION OF COMBUSTION CHAMBER COMPONENTS IN A GASOLINE TURBOCHARGED DIRECT INJECTION (GTDI) ENGINE

Name of School: Michigan Technological University

Number of Copies to be Distributed, and To Whom: It will be available in the MTU library as an electronic document (PDF) and only MTU students and local library patrons will have access to it. Additionally, 1 print copy will be in the library and my adviser and myself will also have print copies.

Format: Electronic and Print

Expected Publication Date: 12/21/2013

Figure 1 and Figure 2 from "Eroding Ribbon Thermocouples: Impulse Response and Transient Heat Flux Analysis" which is found in Volume 18, Number 7 in the journal of Measurement Science and Technology in 2005 on page 1488.

Thanks,
Daniel Madison

Daniel Madison

I need permission to use the same figures in my PhD Dissertation this time. I...

11:14 AM (22 hours ago)

Permissions via mtu.edu

3:37 AM (6 hours ago)

to Daniel

Dear Daniel Madison,

Thank you for your request to reproduce IOP Publishing material.

We are happy to grant permission for the use you request on the terms set out below.

If you have any questions, please feel free to contact our Permissions team at permissions@iop.org.

I should be grateful if you would acknowledge receipt of this email.

Kind regards,
Sarah Ryder

Publishing Administrator
Email: permissions@iop.org

Conditions

Non-exclusive, non-transferrable, revocable, worldwide, permission to use the material in print and electronic form will be granted **subject to the following conditions:**

- Permission will be cancelled without notice if you fail to fulfil any of the conditions of this letter.
- You will make reasonable efforts to contact the author(s) to seek consent for your intended use. Contacting one author acting expressly as authorised agent for their co-authors is acceptable.
- You will reproduce the following prominently alongside the material:
 - the source of the material, including author, article title, title of journal, volume number, issue number (if relevant), page range (or first page if this is the only information available) and date of first publication. This information can be contained in a footnote or reference note; or
 - a link back to the article (via DOI); and
 - if practical and IN ALL CASES for works published under any of the Creative Commons licences the words "© IOP Publishing. Reproduced by permission of IOP Publishing. All rights reserved"
- The material will not, without the express permission of the author(s), be used in any way which, in the opinion of IOP Publishing, could distort or alter the author(s)' original intention(s) and meaning, be prejudicial to the honour or reputation of the author(s) and/or imply endorsement by the author(s) and/or IOP Publishing.
- Payment of £0 is received in full by IOP Publishing prior to use.

Please note: IOP does not usually provide signed permission forms as a separate attachment. Please print this email and provide it to your publisher as proof of permission.

 **David Buttsworth** via mtu.edu
to Daniel 

Nov 1   

Daniel,

As far as I am concerned, you are most welcome to use them again.

Best wishes,

David

From: dpm5049@gmail.com [dpm5049@gmail.com] on behalf of Daniel Madison [dpmadiso@mtu.edu]
Sent: Saturday, 2 November 2013 12:55 AM
To: David Buttsworth
Subject: Re: Copyright Request

Hi David,

I need your permission again to use the figures, this time in my PhD Dissertation.

Title: THERMAL CHARACTERIZATION OF COMBUSTION CHAMBER COMPONENTS IN A GASOLINE TURBOCHARGED DIRECT INJECTION (GTDI) ENGINE

Name of School: Michigan Technological University

Number of Copies to be Distributed, and To Whom: It will be available in the MTU library as an electronic document (PDF) and only MTU students and local library patrons will have access to it. Additionally, 1 print copy will be in the library and my advisor and myself will also have print copies.




Format: Electronic and Print

Expected Publication Date: 12/21/2013

The details of the journal and figures requested are seen below:

Figure 1 and Figure 2 from "Eroding Ribbon Thermocouples: Impulse Response and Transient Heat Flux Analysis" which is found in Volume 16, Number 7 in the journal of Measurement Science and Technology in 2005 on page 1488.




Permission for Fig. 2.7

 **Daniel Madison** <dpm5049@gmail.com> 11:28 AM (1 hour ago) ☆  

to eng ▾

I need your permission again to use the diagram in my PhD dissertation this time.

Thanks,
Dan




 **eng** 12:11 PM (20 minutes ago) ☆  

to me ▾

Hi Dan,

Well congratulations on getting your Master's and good luck with the PhD. You are welcome to use the diagram again, please just give Vatel Corporation credit as the source. Best of luck.

Permission for Figures 2.8, 2.9, 2.11, 2.12, 4.5, and 4.6.

 **Terri Kelly** via mtu.edu Nov 4 ☆  

to Daniel ▾

Dear Daniel,

Thank you for contacting SAE for permission to reprint the figures noted below in your PhD dissertation titled THERMAL CHARACTERIZATION OF COMBUSTION CHAMBER COMPONENTS IN A GASOLINE TURBOCHARGED DIRECT INJECTION (GTDI) ENGINE for Michigan Technological University.

- Figure 6, Figure 7, Figure 8, and Figure 10 from SAE 2009-01-0668
- Figure 1 from SAE 2001-01-2027
- Figure 2 and Figure 3 from SAE 2006-01-0400

Permission is hereby granted, and we request the following copyright statement appear directly below the figures:

"Reprinted with permission Copyright (c) XXXX" SAE International" (*please insert the copyright year from the paper).

We also request that you cite the author(s) and paper number in the reference section of your dissertation.

Again, thank you for contacting SAE for this permission. Please let me know if you need further assistance.





Best regards,


Terri Kelly
Intellectual Property Rights Administrator

SAE INTERNATIONAL
400 Commonwealth Drive
Warrendale, PA 15096

o [+1.724.772.4095](tel:+17247724095)
f [+1.724-776-9765](tel:+17247769765)
e terri@sae.org
www.sae.org

Permission for Fig. 2.10

 **PermissionsUK** <Permissions@sagepub.co.uk>Nov 5   

to me 

Hi Daniel,
Thank you for your email.





Please consider this email as written permission to reuse Figure 1 in "Development of a multipiston temperature telemetry system using Bluetooth networks" from our publication *Part D: Journal of Automobile Engineering* in your PhD dissertation.





Please note:
This permission doesn't cover any 3rd party material found in the work.
The author needs to be informed of this reuse.
A full academic reference to the original material needs to be included.


Best Wishes,
Leah

Permissions Assistant
SAGE Publications Ltd
1 Oliver's Yard, 55 City Road
London, EC1Y 1SP
UK
Available: Tuesdays & Thursdays
Tel: 0207 336 1233
www.sagepub.co.uk
SAGE Publications Ltd, Registered in England No.1017514
Los Angeles | London | New Delhi
Singapore | Washington DC
Thank you for considering the environment before printing this email.

Permission for Fig. 3.7 and Fig. 3.8

Permission to Use IRT Figures in PhD Dissertation  Inbox x MTU/Copyright Permission x   





 **Daniel Madison** <dpm5049@gmail.com> Dec 6 (3 days ago)   


to Glen 

Hi Glen,

I need your permission to use the telemetry components diagram and the telemetry conversion process diagram in my PhD Dissertation. All I need for that is a simple response to this email. You had already done this for my Master's Report and PhD Proposal, but technically I am required to have it again for the Dissertation.

Thanks,
Dan Madison

 **Glen Barna** Dec 6 (3 days ago)   

to me 

Dan,

No problem. You have my permission.

Glen L. Barna

